



저작자표시-비영리-변경금지 2.0 대한민국

이용자는 아래의 조건을 따르는 경우에 한하여 자유롭게

- 이 저작물을 복제, 배포, 전송, 전시, 공연 및 방송할 수 있습니다.

다음과 같은 조건을 따라야 합니다:



저작자표시. 귀하는 원저작자를 표시하여야 합니다.



비영리. 귀하는 이 저작물을 영리 목적으로 이용할 수 없습니다.



변경금지. 귀하는 이 저작물을 개작, 변형 또는 가공할 수 없습니다.

- 귀하는, 이 저작물의 재이용이나 배포의 경우, 이 저작물에 적용된 이용허락조건을 명확하게 나타내어야 합니다.
- 저작권자로부터 별도의 허가를 받으면 이러한 조건들은 적용되지 않습니다.

저작권법에 따른 이용자의 권리는 위의 내용에 의하여 영향을 받지 않습니다.

이것은 [이용허락규약\(Legal Code\)](#)을 이해하기 쉽게 요약한 것입니다.

[Disclaimer](#)

February 2024

PhD Dissertation

Study on Tunable and Two-color Modulation  
Transfer Spectroscopy and Neighboring  
Effects on Electromagnetically Induced  
Absorption and Transparency Using D2  
Transition Line of Rb Atoms

Graduate School of Chosun University

Department of Photonic Engineering

Aisar ul Hassan

Study on Tunable and Two-color Modulation  
Transfer Spectroscopy and Neighboring  
Effects on Electromagnetically Induced  
Absorption and Transparency Using D2  
Transition Line of Rb Atoms

Rb 원자의 D2 전이선을 이용한 주사 가능한  
이색 변조전달분광학과 전자기유도 흡수 및  
투과도의 이웃 전이선 효과에 관한 연구

February 23, 2024

Graduate School of Chosun University

Department of Department of Photonic Engineering

Aisar ul Hassan

Study on Tunable and Two-color Modulation  
Transfer Spectroscopy and Neighboring  
Effects on Electromagnetically Induced  
Absorption and Transparency Using D2  
Transition Line of Rb Atoms

Advisor: Prof. Jin-Tae, Kim

A dissertation submitted in partial fulfillment of the requirements  
for the Degree of Doctor of Philosophy

October 2023



Graduate School of Chosun University



Department of Department of Photonic Engineering

Aisar ul Hassan

This is to certify that the PhD thesis of **Aisar ul Hassan**  
has successfully met the thesis requirements of Chosun  
University.

Chairman: Prof. Jong-Rak Park  

Member: Prof. Jin-Tae Kim  

Member: Prof. Hyun Su Kim  

Member: Prof. Tae-Jung Ahn  

Member: Prof. Heung-Ryoul Noh  

January, 2024

Graduate School of Chosun University

Department of Photonic Engineering

## Abstract

### Study on Tunable and Two-color Modulation Transfer Spectroscopy and Neighboring Effects on Electromagnetically Induced Absorption and Transparency Using D2 Transition Line of Rb Atoms

Aisar ul Hassan

Advisor: Prof. Jin-Tae, Kim

Department of Photonic Engineering

Graduate School of Chosun University

This thesis focuses on two different themes such as modulation transfer spectroscopy (MTS) and neighboring effects on electromagnetically induced absorption (EIA) and electromagnetically induced transparency (EIT). MTS generates a dispersive-like signal with zero background, which is good for laser frequency locking without direct modulation of the probe laser. Additionally, MTS produces strong signals for cycling transitions, which is useful in cycling cases where hyperfine spacing is small and saturation absorption signals are weak. The MTS signals are generated for the  $F_g = 3 \rightarrow F_e = 4$  transition of  $^{85}\text{Rb}$  and the  $F_g = 2 \rightarrow F_e = 3$  transition of  $^{87}\text{Rb}$  atoms for the robust frequency stabilization of the laser. To further demonstrate how this method can be used to generate a single, distinct line for laser frequency stabilization when multiple closely spaced hyperfine transitions are present, we also obtain the MTS signal for the  $F_g = 2 \rightarrow F_e = 1$  transition of  $^{85}\text{Rb}$ . The MTS signals obtained with one laser have been compared to those of two-color MTS (TCMTS).

Secondly, V-type TCMTS has been demonstrated experimentally and theoretically for the D2 line of Rb atoms, considering Zeeman sublevels to solve the optical Bloch equation. The probe beam is resonant on  $F_g = 3 \rightarrow F_e = 2, 3$ , and

4 transitions of  $^{85}\text{Rb}$  and  $F_g = 2 \rightarrow F_e = 1, 2,$  and  $3$  of  $^{87}\text{Rb}$  with scanning and modulating pump beam across  $F_g = 3 \rightarrow F_e = 4$  transition of  $^{85}\text{Rb}$  and  $F_g = 2 \rightarrow F_e = 3$  of  $^{87}\text{Rb}$ , respectively. This method has the advantage that various configurations of pump and probe beams, etc., can be prepared. The calculated results of TCMTS using optical Bloch equation match well with the experimentally obtained ones. Thus, we have spectroscopic tools to do MTS for high-lying excited states with various configurations of pump and probe beams.

Thirdly, the tunable characteristics of the MTS, which generate a dispersive-like tunable reference signal that does not compromise on amplitude and signal gradient, have also been investigated. The Tunable Modulation Transfer Spectroscopy (TMTS) generated for  $F_g = 3 \rightarrow F_e = 4$  and  $F_g = 2 \rightarrow F_e = 1$  transitions of  $^{85}\text{Rb}$  are used for Type I and Type II magneto-optical trapping (MOT) of atoms in the  $F_g = 3$  and  $F_g = 2$  energy levels of the  $5S_{1/2}$  ground state, respectively. For  $F_g = 2 \rightarrow F_e = 1$  cycling transition  $F_e < F_g$ , the ground and excited Zeeman sub-levels do not couple, which makes the excited hyperfine level the dark state and do not contribute to the trapping so that weak trapping force happens. Laser trapping for atoms in lower ground state hyperfine energy levels has been reported only using polarization spectroscopy.

Next, the influence of neighboring transitions on electromagnetically induced absorption (EIA) and electromagnetically induced transparency (EIT) with respect to the angle between the polarization axes of the coupling and probe beams has been investigated for the D2 transition line of Rb. The angle between the polarization axes of the coupling and probe beams plays a major role in switching from EIA to EIT or vice versa along with the influence of neighboring hyperfine energy levels. The critical angles for coherent control of EIA and EIT are obtained from the experiment and theory using optical Bloch equations. The theoretical critical angles match well with experimental ones.

Lastly, effects of neighboring transitions through Doppler broadening on EIA and EIT of the degenerate two-level system at the  $F_g = 2 \rightarrow F_e = 1, 2,$  and  $3$  transitions of  $^{87}\text{Rb}$  D2 line have been investigated. Two different polarization configurations such as linear parallel and linear perpendicular polarization of coupling

and probe lasers, have been studied. We study the significant variation of EIT and EIA due to the effect of the neighboring transitions via artificial variation of the hyperfine spacings of the  $5P_{3/2}$  state. The dependence of spectral features on the hyperfine spacing for circular parallel and circular orthogonal polarizations of coupling and probe is also calculated by artificially varying the hyperfine spacing of  $^{85}\text{Rb}$  atoms. Result calculated from a specific hyperfine separation can be used to predict the transitions between EIA and EIT.

**Index Terms:** MTS, TMTS, TCMTS, MOT, EIA, EIT, DTLS, rubidium atoms, Doppler broadening, coupling-probe spectroscopy, laser cooling



## 초록

### Rb 원자의 D2 전이선을 이용한 주사 가능한 이색 변조전달분광학과 전자기유도 흡수 및 투과의 이웃 전이선 효과에 관한 연구

아이사르 울 하산

지도교수: 김진태 교수

광기술공학과

조선대학교 대학원

본 학위 논문은 변조전달분광학과 EIA와 EIT의 이웃 전이선 효과와 같은 두 개의 다른 주제에 초점을 둔다. MTS는 프로브 레이저 빔의 직접적인 변조없이 레이저 주파수 고정에 좋은 배경신호가 없는 미분 신호를 생성한다. 부가적으로 초미세 구조 간격이 작고 포화 흡수 분광학 신호가 약한 경우의 사이클링 전이선에 강한 MTS 신호를 생성한다. 본 연구에서 레이저의 강력한 주파수 안정화를 위해  $^{85}\text{Rb}$  원자의  $F_g = 3 \rightarrow F_e = 4$  전이선과  $^{87}\text{Rb}$  원자의  $F_g = 2 \rightarrow F_e = 3$  전이선에 대한 MTS 신호를 얻었다. 또한, 다중의 근접한 초미세 구조가 존재할 때 하나의 분명한 단일 주파수 미분 신호를 얻는 데 사용할 수 있는지에 대한 예시를 보이기 위하여  $^{85}\text{Rb}$  원자의  $F_g = 2 \rightarrow F_e = 1$  전이선에 대한 MTS 신호를 얻었다. 이러한 단일 레이저에 의한 MTS 신호는 이색 MTS 신호와 비교하였다.

두 번째로 V-타입 이색 MTS가 Rb 원자의 D2 전이선에 대해 실험적으로 구현되었으며 이론적으로는 제만 부준위를 고려한 광-블로흐 방정식을 고려하여 이론적으로 얻은 결과와 비교하였다. 프로브 빔은  $^{85}\text{Rb}$  원자의  $F_e = 3 \rightarrow F_g = 2, 3, 4$  전이선과  $^{87}\text{Rb}$  원자의  $F_e = 2 \rightarrow F_g = 1, 2, 3$  전이선에 주파수가 고정되고, 변조된 펄스 레이저 빔은 각각  $F_g = 3 \rightarrow F_e = 4, F_g = 2 \rightarrow F_e = 3$  전이선을 스캔하였다. 이러한 이색 MTS 방법은 펄스와 프로브 빔의 여러 구도로 준비될 수 있는 장점을 가지고 있다. 이색 MTS 신호를 광블로흐 방정식을

이용하여 계산된 MTS 신호는 실험적으로 얻은 결과와 잘 일치하는 것을 알 수 있었다. 그래서 펌프빔과 프로브 빔의 여러구도로 고에너지 상태에 대한 MTS 를 구현할 수 있는 MTS 분광 기술을 가지게 되었다.

세 번째로 진폭과 신호 그레디언트에 절충하지 않는 미분 형태의 스캔 가능한 참조 신호를 생성하는 MTS의 스캔 특성들이 연구되었다. 또한, 스캔 가능한 MTS 신호를 이용하여  $^{85}\text{Rb}$ 의  $F_g = 2 \rightarrow F_e = 1$ ,  $F_g = 3 \rightarrow F_e = 4$ 의 전이선들에 주파수 안정화된 레이저 빔을 이용하여  $5S_{1/2}$ 기저상태의  $F_g = 3$ 과  $F_g = 2$ 의 에너지 준위에 있는 원자들에 대한 Type I, II Magneto-Optical Trapping (MOT)을 구현하였다.  $F_e < F_g$ 인 Type II 전이선인  $F_g = 2 \rightarrow F_e = 1$ 의 사이클링 전이선은 기저준위와 여기준위의 제만분준위간에 결합되지 않는 여기 상태의 암흑 전자 상태를 만들어 더 이상 레이저 포획에 기여 못해 약한 포획 결과를 가져온다. 기저상태의 낮은 초미세 구조에 있는 원자들에 대한 포획은 단지 편광분광학을 통해서 구현된 바 있다.

다음으로 커플링 빔과 프로브 빔의 편광축들간의 사잇각에 따른 전자기 유도 흡수와 전자기 유도 투과가 이웃전이선들의 영향이 어떻게 되는지를 연구 하였다. 편광축들간의 사잇각은 EIA에서 이웃 전이선들의 영향을 받는 EIT로 혹은 EIT에서 EIA로 스위칭되는 것에 중요한 역할을 함을 알았다. EIA와 EIT의 결맞은 제어를 위한 임계각이 실험과 광-블로흐 방정식을 사용하는 이론으로부터 얻어 졌으며 이론치와 실험치가 잘 맞는 것을 확인하였다.

마지막으로  $^{87}\text{Rb}$  D2 전이선인  $F_e = 2 \rightarrow F_g = 1, 2, 3$ 에서 측정된 이준위계의 EIA와 EIT에 도플러 확장을 통한 이웃 전이선 효과가 연구되었다. 커플링 빔과 프로브 빔의 선형적으로 평행한 경우와 수직 구도의 두 개의 다른 편광 구도들이 연구되었다. 여기서  $5P_{3/2}$  상태의 초미세 구조 간격에의 인위적인 변위에 따른 이웃 전이선의 영향에 기인한 EIT와 EIA의 변화를 연구하였다. 커플링 및 프로브 빔의 평행한 원형 편광과 수직인 원형 구도에서  $^{85}\text{Rb}$  원자의 인위적으로 초미세구조 간격을 변화시켜 가면서 초미세구조 간격에 따른 스펙트라의 종속 변환이 계산되어 졌다. 특정 초미세 간격에서 계산된 결과는 EIA 및 EIT 스위칭을 예측할 수 있었다.

**Index Terms:** MTS, TMTS, TCMTS, MOT, EIA, EIT, DTLS, rubidium atoms,

Doppler broadening, coupling-probe spectroscopy, laser cooling

## Acronyms

AOM	Acousto-Optic Modulator
BS	Beam Splitter
DLC	Diode Laser Controller
DTLS	Degenerate Two-Level System
DMLS	Degenerate Multi-Level System
EOM	Electro-Optic Modulator
FWM	Four-wave Mixing
ECDL	External Cavity Diode Laser
EIA	Electromagnetically Induced Absorption
EIT	Electromagnetically Induced Transparency
HWP	Half-Wave Plate
MHz	Mega Hertz
MOT	Magneto-optical Trap
MTS	Modulation Transfer Spectroscopy
NDF	Neutral Density Filter
OBE	Optical Bloch Equations
OI	Optical Isolator
PBS	Polarizing Beam Splitter
PD	Photo Diode
QWP	Quater-Wave Plate
Rb	Rubidium
SAS	Saturation Absorption Spectroscopy
TA	Tapered Amplifier
TCMTS	Two-color Modulation Transfer Spectroscopy
TMTS	Tunable Modulation Transfer Spectroscopy
W	Window

# Contents

<b>Abstract [English]</b>	<b>i</b>
<b>Abstract [Korean]</b>	<b>iv</b>
<b>Acronyms</b>	<b>vii</b>
<b>List of Figures</b>	<b>xi</b>
<b>1 Introduction</b>	<b>1</b>
1.1 Laser Spectroscopy . . . . .	1
1.1.1 Atomic Structure . . . . .	3
1.1.2 Saturation Absorption Spectroscopy . . . . .	5
1.2 Magneto-Optical Trapping (MOT) . . . . .	9
1.3 Electromagnetically Induced Absorption (EIA) and Electromag- netically Induced Transparency (EIT) . . . . .	13
1.4 Organization of Dissertation . . . . .	16
<b>2 Two-color Modulation Transfer Spectroscopy</b>	<b>17</b>
2.1 Overview . . . . .	17
2.2 Modulation Transfer Spectroscopy . . . . .	18
2.2.1 Experimental Setup . . . . .	19
2.2.2 Results and Discussion . . . . .	20
2.3 Two-color Modulation Transfer Spectroscopy . . . . .	22
2.3.1 Experimental Setup . . . . .	23
2.3.2 Results and Discussion . . . . .	25
2.4 Summary . . . . .	29
<b>3 Magneto-optical Trapping</b>	<b>31</b>
3.1 Overview . . . . .	31

3.2	Tunable Modulation Transfer Spectroscopy . . . . .	31
3.2.1	Experimental Setup . . . . .	33
3.2.2	Results and Discussion . . . . .	36
3.3	Magneto-Optical Trap . . . . .	38
3.3.1	Experimental Setup . . . . .	40
3.3.2	Results and Discussion . . . . .	42
3.4	Summary . . . . .	44
<b>4</b>	<b>EIA and EIT with Varying Linear Polarization</b>	<b>46</b>
4.1	Overview . . . . .	46
4.2	Theoretical Background . . . . .	48
4.3	Experimental Setup . . . . .	50
4.4	Results and Discussion . . . . .	52
4.4.1	$F_g = 2 \rightarrow F_e = 1, 2, \text{ and } 3$ transitions of $^{85}\text{Rb}$ . . . . .	53
4.4.2	$F_g = 3 \rightarrow F_e = 2, 3, \text{ and } 4$ transitions of $^{85}\text{Rb}$ . . . . .	56
4.4.3	$F_g = 1 \rightarrow F_e = 0, 1, \text{ and } 2$ transitions of $^{87}\text{Rb}$ . . . . .	60
4.4.4	$F_g = 2 \rightarrow F_e = 1, 2, \text{ and } 3$ transitions of $^{87}\text{Rb}$ . . . . .	64
4.5	Summary . . . . .	68
<b>5</b>	<b>Coherent Control of EIA and EIT</b>	<b>69</b>
5.1	Overview . . . . .	69
5.2	Artificial Variation in Hyperfine Splitting of $^{87}\text{Rb}$ . . . . .	69
5.2.1	Methods . . . . .	70
5.2.2	Results and Discussion . . . . .	72
5.3	Artificial Variation in Hyperfine Splitting of $^{85}\text{Rb}$ . . . . .	77
5.3.1	Experimental Setup . . . . .	77
5.3.2	Results and Discussion . . . . .	79
5.4	Summary . . . . .	84
<b>6</b>	<b>Conclusion</b>	<b>85</b>
	<b>List of Publications</b>	<b>89</b>



## Bibliography

# List of Figures

1.1	Energy level (not to scale) diagram of $^{85}\text{Rb}$ atoms . . . . .	2
1.2	Energy level (not to scale) diagram of $^{87}\text{Rb}$ atoms . . . . .	4
1.3	Basic experimental arrangement for Saturation Absorption Spectroscopy . . . . .	5
1.4	(a) Simple two level energy level diagram (b) Transmission spectra of the probe beam; the blue dotted line is in the presence of a pump beam, whereas the red line is only a probe beam. . . . .	6
1.5	Schematic diagram of experimental setup. Component symbols: W: window; HWP: half-wave plate; QWP: quarter-wave plate; PBS: polarizing beam splitter; M: mirror; NDF: neutral density filter PD: photo-detector. . . . .	7
1.6	SAS spectral profile of D2 transition line of Rb atoms . . . . .	8
1.7	MOT configuration with three pairs of laser beams and a pair of anti-Helmholtz coils. . . . .	9
1.8	Energy level diagram of atom under the influence of magnetic field in 1D MOT . . . . .	12
1.9	Basic experimental arrangement for Electromagnetically Induced Absorption and Transparency . . . . .	14
2.1	Schematic diagram of basic MTS setup. . . . .	17
2.2	Energy level diagram of MTS. The pump beam is modulated by EOM. . . . .	18
2.3	Schematic diagram of experimental setup. Component symbols: SAS: saturation absorption spectroscopy; W: window; HWP: half-wave plate; PBS: polarizing beam splitter; EOM: electro-optic modulator; M: mirror; PD: photo-detector. . . . .	20
2.4	Comparison between SAS and MTS signals for the $^{85}\text{Rb } F_g = 3 \rightarrow F_e = 4$ and $^{87}\text{Rb } F_g = 2 \rightarrow F_e = 3$ transitions . . . . .	21



2.5	Comparison between SAS and MTS signals for $^{85}\text{Rb } F_g = 2 \rightarrow F_e = 1$ transition. . . . .	22
2.6	Energy Level diagram of TCMTS. The modulated pump beam is scanning across transitions from $F_g = 3$ ( $F_g = 2$ ) of $^{85}\text{Rb}$ ( $^{87}\text{Rb}$ ) atoms whereas, the probe beam is fixed at (a) $F_g = 3 \rightarrow F_e = 2$ ( $F_g = 2 \rightarrow F_e = 1$ ) (b) $F_g = 3 \rightarrow F_e = 3$ ( $F_g = 2 \rightarrow F_e = 2$ ), and (c) $F_g = 3 \rightarrow F_e = 4$ ( $F_g = 2 \rightarrow F_e = 3$ ) resonance lines of $^{85}\text{Rb}$ ( $^{87}\text{Rb}$ ) atoms. . . . .	23
2.7	Schematic diagram of experimental setup. Component symbols: SAS: saturation absorption spectroscopy; W: window; HWP: half-wave plate; PBS: polarizing beam splitter; EOM: electro-optic modulator; M: mirror; PD: photo-detector. . . . .	24
2.8	Comparison of SAS, MTS, and TCMTS signals . . . . .	25
2.9	TCMTS signals with phase $\phi = 0$ to 180 of (a) probe beam is fixed at $^{85}\text{Rb } F_g = 3 \rightarrow F_e = 2$ transition while pump beam is scanning across the transitions from $^{85}\text{Rb } F_g = 3$ , (b) probe beam is fixed at $^{85}\text{Rb } F_g = 3 \rightarrow F_e = 3$ transition while pump beam is scanning across the transitions from $^{85}\text{Rb } F_g = 3$ , and (c) probe beam is fixed at $^{85}\text{Rb } F_g = 3 \rightarrow F_e = 4$ transition while pump beam is scanning across the transitions from $^{85}\text{Rb } F_g = 3$ . . . . .	26
2.10	TCMTS signals with phase $\phi = 0$ to 180 of (a) probe beam is fixed at $^{87}\text{Rb } F_g = 2 \rightarrow F_e = 1$ transition while pump beam is scanning across the transitions from $^{87}\text{Rb } F_g = 2$ (plots are 25 times the original signal), (b) probe beam is fixed at $^{87}\text{Rb } F_g = 2 \rightarrow F_e = 2$ transition while pump beam is scanning across the transitions from $^{87}\text{Rb } F_g = 2$ (plots are 6 times the original signal), and (c) probe beam is fixed at $^{87}\text{Rb } F_g = 2 \rightarrow F_e = 3$ transition while pump beam is scanning across the transitions from $^{87}\text{Rb } F_g = 2$ . . . . .	27

2.11	Comparison of TCMTS signals with probe beam fixed at $^{87}\text{Rb } F_g = 2 \rightarrow F_e = 1, 2,$ and 3 resonance lines with pump beam scanning across transitions from $F_g = 2,$ and $^{85}\text{Rb } F_g = 3 \rightarrow F_e = 2, 3,$ and 4 resonance lines with pump beam scanning across transitions from $F_g = 3.$ . . . . .	29
3.1	Energy Level diagram of TMTS. The color of the line indicates whether the laser beam is detuned to the red or blue side of the resonance line in two different experimental setups. . . . .	32
3.2	Schematic diagram of experimental setup. Component symbols: SAS: saturation absorption spectroscopy; NDF: neutral density filter; W: window; HWP: half-wave plate; QWP: Quarter-wave plate; PBS: polarizing beam splitter; AOM: acousto-optic modulator; EOM: electro-optic modulator; M: mirror; BD: beam dump; PD: photo-detector. . . . .	34
3.3	Comparison of SAS and red detuned SAS and TMTS by 200 MHz. The blue line is SAS signal, red line is detuned SAS signal, and green line is TMTS signal. . . . .	35
3.4	Comparison of SAS and blue detuned SAS and TMTS by 200 MHz . . . . .	36
3.5	Comparison between red and blue detuned TMTS signals. . . . .	37
3.6	GUI for MOT using LabVIEW . . . . .	38
3.7	Energy level diagram of Type-I and Type-II MOT. . . . .	39
3.8	Schematic diagram of experimental setup. Component symbols: SAS: saturation absorption spectroscopy; TMTS: tunable modulation transfer spectroscopy; W: window; HWP: half-wave plate; QWP: Quarter-wave plate; PBS: polarizing beam splitter; BE: beam expander; M: mirror; OI: optical isolator; BD: beam dump; UHVC: ultra-high vacuum chamber. . . . .	41
3.9	Image of MOT for atoms in $^{85}\text{Rb } F_g = 3$ hyperfine ground state. . . . .	42
3.10	Image of MOT for atoms in $^{85}\text{Rb } F_g = 2$ hyperfine ground state. . . . .	43

4.1 Energy level diagram for the  $F_g = 3 \rightarrow F_e = 4$  transitions of  $^{85}\text{Rb}$  D2 line. The blue and red lines imply the transitions excited by coupling and probe beams, respectively. . . . . 47

4.2 Schematic diagram of experimental setup. Component symbols: SAS: saturation absorption spectroscopy; W: window; HWP: halfwave plate; PBS: polarizing beam splitter; BE: beam expander; A: aperture; AOM: acousto-optic modulator; M: mirror; BS: beam splitter; Bd: beam dump; PD: photodetector. . . . . 51

4.3 Comparison of calculated and measured spectra for  $F_g = 2 \rightarrow F_e = 1$  transition considering (a) pure two-level resonant transition (b) a transition resonant at  $F_g = 2 \rightarrow F_e = 1$  with neighboring hyperfine transitions  $F_g = 2 \rightarrow F_e = 2$  and  $F_g = 2 \rightarrow F_e = 3$  (c) experimentally measured spectra for resonant transition  $F_g = 2 \rightarrow F_e = 1$ . . . . . 53

4.4 Comparison of calculated and measured spectra for  $F_g = 2 \rightarrow F_e = 2$  transition considering (a) pure two-level resonant transition (b) a transition resonant at  $F_g = 2 \rightarrow F_e = 2$  with neighboring hyperfine transitions  $F_g = 2 \rightarrow F_e = 3$  and  $F_g = 2 \rightarrow F_e = 1$  (c) experimentally measured spectra for resonant transition  $F_g = 2 \rightarrow F_e = 2$ . . . . . 54

4.5 Comparison of calculated and measured spectra for  $F_g = 2 \rightarrow F_e = 3$  transition considering (a) pure two-level resonant transition (b) a transition resonant at  $F_g = 2 \rightarrow F_e = 3$  with neighboring hyperfine transitions  $F_g = 2 \rightarrow F_e = 1$  and  $F_g = 2 \rightarrow F_e = 2$  (c) experimentally measured spectra for resonant transition  $F_g = 2 \rightarrow F_e = 3$ . . . . . 55

4.6 Comparison of calculated and measured spectra for  $F_g = 3 \rightarrow F_e = 4$  transition considering (a) pure two-level resonant transition (b) a transition resonant at  $F_g = 3 \rightarrow F_e = 4$  with neighboring hyperfine transitions  $F_g = 3 \rightarrow F_e = 3$  and  $F_g = 3 \rightarrow F_e = 2$  (c) experimentally measured spectra for resonant transition  $F_g = 3 \rightarrow F_e = 4$ . . . . . 57

4.7 Comparison of calculated and measured spectra for  $F_g = 3 \rightarrow F_e = 3$  transition considering (a) pure two-level resonant transition (b) a transition resonant at  $F_g = 3 \rightarrow F_e = 3$  with neighboring hyperfine transitions  $F_g = 3 \rightarrow F_e = 2$  and  $F_g = 3 \rightarrow F_e = 4$  (c) experimentally measured spectra for resonant transition  $F_g = 3 \rightarrow F_e = 3$ . . . . . 58

4.8 Comparison of calculated and measured spectra for  $F_g = 3 \rightarrow F_e = 2$  transition considering (a) pure two-level resonant transition (b) a transition resonant at  $F_g = 3 \rightarrow F_e = 2$  with neighboring hyperfine transitions  $F_g = 3 \rightarrow F_e = 3$  and  $F_g = 3 \rightarrow F_e = 4$  (c) experimentally measured spectra for resonant transition  $F_g = 3 \rightarrow F_e = 2$ . . . . . 59

4.9 Comparison of calculated and measured spectra for  $F_g = 1 \rightarrow F_e = 0$  transition considering (a) pure two-level resonant transition (b) a transition resonant at  $F_g = 1 \rightarrow F_e = 0$  with neighboring hyperfine transitions  $F_g = 1 \rightarrow F_e = 1$  and  $F_g = 1 \rightarrow F_e = 2$  (c) experimentally measured spectra for resonant transition  $F_g = 1 \rightarrow F_e = 0$ . . . . . 61

4.10 Comparison of calculated and measured spectra for  $F_g = 1 \rightarrow F_e = 1$  transition considering (a) pure two-level resonant transition (b) a transition resonant at  $F_g = 1 \rightarrow F_e = 1$  with neighboring hyperfine transitions  $F_g = 1 \rightarrow F_e = 0$  and  $F_g = 1 \rightarrow F_e = 2$  (c) experimentally measured spectra for resonant transition  $F_g = 1 \rightarrow F_e = 1$ . . . . . 62

4.11	Comparison of calculated and measured spectra for $F_g = 1 \rightarrow F_e = 2$ transition considering (a) pure two-level resonant transition (b) a transition resonant at $F_g = 1 \rightarrow F_e = 2$ with neighboring hyperfine transitions $F_g = 1 \rightarrow F_e = 0$ and $F_g = 1 \rightarrow F_e = 1$ (c) experimentally measured spectra for resonant transition $F_g = 1 \rightarrow F_e = 2$ . . . . .	63
4.12	Comparison of calculated and measured spectra for $F_g = 2 \rightarrow F_e = 3$ transition considering (a) pure two-level resonant transition (b) a transition resonant at $F_g = 2 \rightarrow F_e = 3$ with neighboring hyperfine transitions $F_g = 2 \rightarrow F_e = 1$ and $F_g = 2 \rightarrow F_e = 2$ (c) experimentally measured spectra for resonant transition $F_g = 2 \rightarrow F_e = 3$ . . . . .	64
4.13	Comparison of calculated and measured spectra for $F_g = 2 \rightarrow F_e = 2$ transition considering (a) pure two-level resonant transition (b) a transition resonant at $F_g = 2 \rightarrow F_e = 2$ with neighboring hyperfine transitions $F_g = 2 \rightarrow F_e = 3$ and $F_g = 2 \rightarrow F_e = 1$ (c) experimentally measured spectra for resonant transition $F_g = 2 \rightarrow F_e = 2$ . . . . .	66
4.14	Comparison of calculated and measured spectra for $F_g = 2 \rightarrow F_e = 1$ transition considering (a) pure two-level resonant transition (b) a transition resonant at $F_g = 2 \rightarrow F_e = 1$ with neighboring hyperfine transitions $F_g = 2 \rightarrow F_e = 3$ and $F_g = 2 \rightarrow F_e = 2$ (c) experimentally measured spectra for resonant transition $F_g = 2 \rightarrow F_e = 1$ . . . . .	67
5.1	(a) Energy level diagram of $^{87}\text{Rb}$ D2 transition line, wherein the red and blue lines indicate transitions by the probe and coupling beams, respectively. (b) Level schemes considered in the case of the $F_g = 2 \rightarrow F_e = 3$ transition with two coupling and probe beams in (i) $\pi \perp \pi$ and, (ii) $\pi \parallel \pi$ configurations. . . . .	71

5.2 The spectral characteristics of the  $\pi \perp \pi$  configuration with artificial variation in the hyperfine splittings of  $^{87}\text{Rb}$  for the (a)  $F_g = 2 \rightarrow F_e = 3$ , (b)  $F_g = 2 \rightarrow F_e = 2$ , and (c)  $F_g = 2 \rightarrow F_e = 1$  transitions. 75

5.3 The spectral characteristics of the  $\pi \parallel \pi$  configuration with artificial variation in the hyperfine splittings of  $^{87}\text{Rb}$  for the (a)  $F_g = 2 \rightarrow F_e = 3$ , (b)  $F_g = 2 \rightarrow F_e = 2$ , and (c)  $F_g = 2 \rightarrow F_e = 1$  transitions. 76

5.4 Schematic diagram of experimental setup. Component symbols: SAS: saturation absorption spectroscopy; W: window; HWP: halfwave plate; QWP: quarter-wave plate; PBS: polarizing beam splitter; BE: beam expander; A: aperture; AOM: acousto-optic modulator; M: mirror; BS: beam splitter; Bd: beam dump; PD: photodetector. 78

5.5 Spectral profiles with  $\sigma \parallel \sigma$  configuration of coupling and probe beams at  $F_g = 3 \rightarrow F_e = 2, 3$ , and 4 of  $^{85}\text{Rb}$  D2 line considering (a) DTLS calculations without neighboring effects of  $F_g = 3 \rightarrow F_e = 2, F_g = 3 \rightarrow F_e = 3$ , and  $F_g = 3 \rightarrow F_e = 4$  transitions; (b) DMLS calculations (with neighboring effects) of  $F_g = 3 \rightarrow F_e = 2$  (3 and 4),  $F_g = 3 \rightarrow F_e = 3$  (2 and 4), and  $F_g = 3 \rightarrow F_e = 4$  (2 and 3); and (c) experimentally measured spectra for  $F_g = 3 \rightarrow F_e = 2, F_g = 3 \rightarrow F_e = 3$ , and  $F_g = 3 \rightarrow F_e = 4$  transitions. . . . . 79

5.6 Spectral profile with artificial variation in hyperfine splitting of  $F_g = 3 \rightarrow F_e = 2$  transition of  $^{85}\text{Rb}$  with respect to circular parallel ( $\sigma \parallel \sigma$ ) configuration of coupling and probe beams. . . . . 81

5.7 Spectral profiles with  $\sigma \perp \sigma$  configuration of coupling and probe beams at  $F_g = 3 \rightarrow F_e = 2, 3$ , and 4 of  $^{85}\text{Rb}$  D2 line considering (a) DTLS calculations without neighboring effects of  $F_g = 3 \rightarrow F_e = 2, F_g = 3 \rightarrow F_e = 3$ , and  $F_g = 3 \rightarrow F_e = 4$  transitions; (b) DMLS calculations (with neighboring effects) of  $F_g = 3 \rightarrow F_e = 2$  (3 and 4),  $F_g = 3 \rightarrow F_e = 3$  (2 and 4), and  $F_g = 3 \rightarrow F_e = 4$  (2 and 3); and (c) experimentally measured spectra for  $F_g = 3 \rightarrow F_e = 2, F_g = 3 \rightarrow F_e = 3$ , and  $F_g = 3 \rightarrow F_e = 4$  transitions. . . . . 82

5.8 Spectral profile with artificial variation in hyperfine splitting of  $F_g = 3 \rightarrow F_e = 2$  transition of  $^{85}\text{Rb}$  with respect to circular orthogonal ( $\sigma \perp \sigma$ ) configuration of coupling and probe beams. . . . . 83

## Chapter 1

# Introduction

## 1.1 Laser Spectroscopy

Ever since the invention of lasers in the 1960s [1] and later acquiring knowledge of Bose-Einstein Condensation (BEC) in 1995 [2–4], technological evolution involving lasers has required laser frequency stabilization. External cavity diode lasers are extensively used in AMO physics research, and active frequency stabilization of free running lasers to some stable reference is paramount for various applications, including gravitational-wave detectors [5], precision measurements [6], laser cooling [7], and optical clocks [8–10]. An external reference is generated to be utilized in conjunction with the laser cavity’s feedback control for this frequency stabilization. The Doppler-free locking signal generated using saturation absorption spectroscopy (SAS) [11, 12] is a commonly used technique for laser frequency locking. Doppler-free locking approaches offer enhanced precision and a narrower range for locking. The enhanced accuracy is a result of a more pronounced increase in spectral sensitivity. The approach employed in this methodology, wherein the laser frequency is precisely adjusted to align with the Doppler-free peak, presents a harmonious trade-off between precision and the extent of tuning capabilities. It offers consistent frequency stability without necessitating a wide array of modifications.

Frequency modulated spectroscopy (FMS) [13, 14] is another noteworthy technique in which the laser frequency is precisely synchronized with the maximum point of an atomic reference signal. FMS demonstrates an outstanding signal-to-noise ratio, rendering it highly suitable for scenarios that prioritize sensitivity. Whereas polarizing spectroscopy (PS) [15–17] presents itself as a viable alternative in cases where frequency modulation and phase-sensitive detection are not favored. The phase-locked loop can provide a reference signal that has a dispersion-like characteristic, making it suited for peak locking. This approach enables the achievement of stable frequency locking without the requirement of frequency modulation, thereby simplifying the experimental configuration and



decreasing its complexity. The main aim of these techniques is to generate a dispersive-like reference signal to provide feedback for locking the laser, with zero crossings representing the atomic resonance.

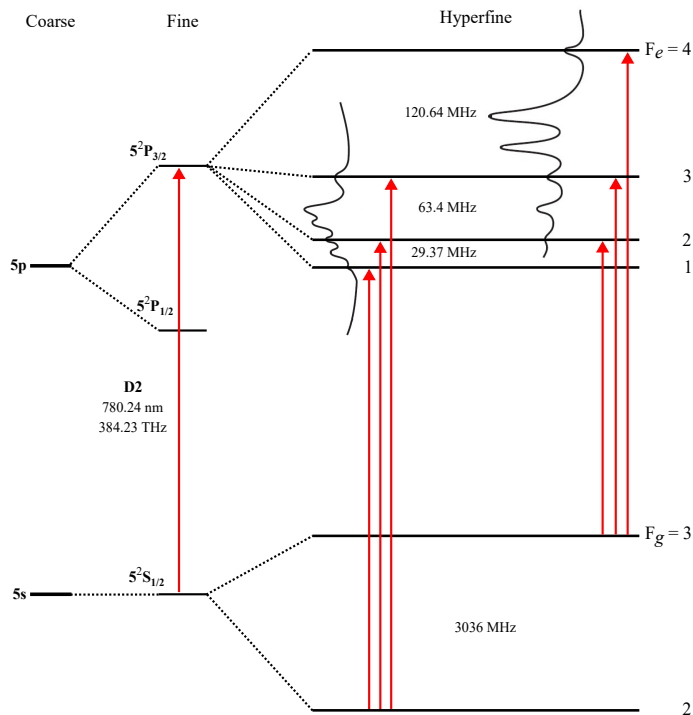


**Figure 1.1:** Energy level (not to scale) diagram of  $^{85}\text{Rb}$  atoms

In general, the techniques for laser frequency stabilization use the pump-probe scheme, where a weak probe beam in a vapor cell has a negligible effect on the population in the ground state of atoms and a pump beam coming from the opposite direction influences the population significantly. Due to this pump-probe scheme, crossover resonances also show up, along with hyperfine transition lines in the absorption spectrum. Moreover, the reference or locking signal can also have distinct lines for these crossover resonances. Modulation transfer spectroscopy (MTS) [18–22] exhibits the ability to generate steeper signal gradients with zero background, and the signals are mostly influenced by the contribution originating from closed atomic transitions. The aforementioned secondary

characteristic proves to be particularly advantageous in cases where the spectrum under consideration comprises multiple closely spaced transitions.

This thesis presents the MTS signals for the  $F_g = 3 \rightarrow F_e = 4$  and  $F_g = 2 \rightarrow F_e = 3$  D2 transition lines of  $^{85}\text{Rb}$  and  $^{87}\text{Rb}$  atoms, respectively. Furthermore, the MTS of  $F_g = 2 \rightarrow F_e = 1$  transition of  $^{85}\text{Rb}$  serves as an example to illustrate how this technique may provide a single spectral line for laser frequency stabilization, even in the presence of many closely spaced hyperfine transitions. In addition to this, V-type two-color Modulation transfer Spectroscopy (TCMTS) has been demonstrated experimentally and theoretically for the D2 transition line of Rb atoms. In six configurations in total, the probe beam is resonant on  $F_g = 3 \rightarrow F_e = 2, 3,$  and  $4$  transitions of  $^{85}\text{Rb}$  and  $F_g = 2 \rightarrow F_e = 1, 2,$  and  $3$  of  $^{87}\text{Rb}$  with scanning and modulating pump beam across  $F_g = 3 \rightarrow F_e = 4$  transition of  $^{85}\text{Rb}$  and  $F_g = 2 \rightarrow F_e = 3$  of  $^{87}\text{Rb}$ , respectively. This technique provides the advantage of preparing various configurations of pump and probe beams.

### 1.1.1 Atomic Structure

This work focuses on the D2 transition line [23, 24] of Rubidium (Rb). Rb has two naturally occurring isotopes: 72% abundant  $^{87}\text{Rb}$  with nuclear spin angular momentum ( $I$ ) = 3/2 and 28% abundant  $^{85}\text{Rb}$  with  $I = 5/2$ . The ground state (5s) with one possible value of electronic angular momentum ( $J$ ) is labeled as  $5^2S_{1/2}$ , whereas next excited state (5p) with two allowed values are labeled as  $5^2P_{1/2}$  and  $5^2P_{3/2}$ . Furthermore, depending on the total angular momentum ( $F$ ), the hyperfine energy levels take values from  $|J - I|$  to  $|J + I|$ . The coarse, fine, and hyperfine structure of  $^{85}\text{Rb}$  is shown in Fig. 1.1. The ground and excited state of  $^{85}\text{Rb}$  take 2 and 4 values, respectively:

$$\begin{array}{ll}
 F_g = 2 & m_{F_g=2} = +2, +1, 0, -1, -2 \\
 F_g = 3 & m_{F_g=3} = +3, +2, +1, 0, -1, -2, -3
 \end{array}$$

$$\begin{aligned}
 F_e = 1 & \quad m_{F_e=1} = +1, 0, -1 \\
 F_e = 2 & \quad m_{F_e=2} = +2, +1, 0, -1, -2 \\
 F_e = 3 & \quad m_{F_e=3} = +3, +2, +1, 0, -1, -2, -3 \\
 F_e = 4 & \quad m_{F_e=4} = +4, +3, +2, +1, 0, -1, -2, -3, -4
 \end{aligned}$$

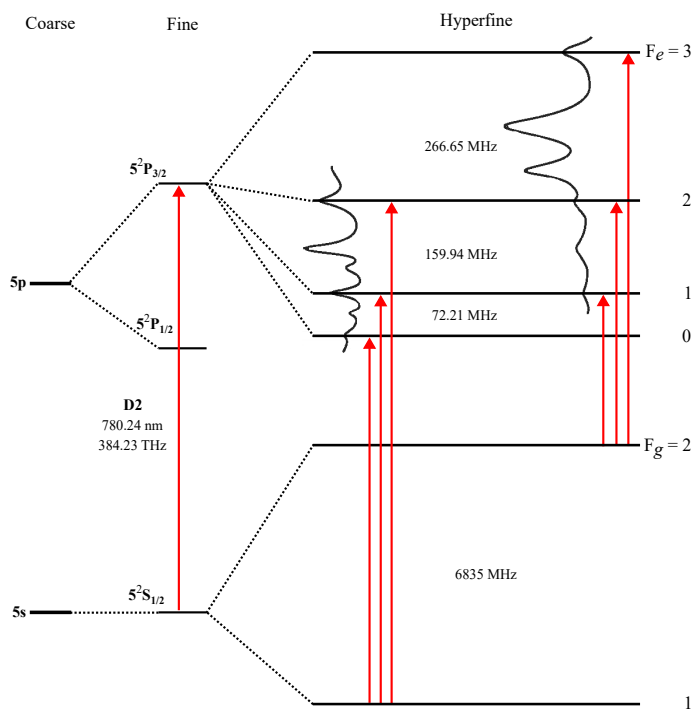


**Figure 1.2:** Energy level (not to scale) diagram of  $^{87}\text{Rb}$  atoms

The ground and excited hyperfine state of  $^{87}\text{Rb}$  also take 2 and 4 values, respectively, as shown in Fig. 1.2 and their magnetic sublevels are:

$$\begin{aligned}
 F_g = 1 & & m_{F_g=1} = +1, 0, -1 \\
 F_g = 2 & & m_{F_g=2} = +2, +1, 0, -1, -2 \\
 \\ \\
 F_e = 0 & & m_{F_e=0} = 0 \\
 F_e = 1 & & m_{F_e=1} = +1, 0, -1 \\
 F_e = 2 & & m_{F_e=2} = +2, +1, 0, -1, -2 \\
 F_e = 3 & & m_{F_e=3} = +3, +2, +1, 0, -1, -2, -3
 \end{aligned}$$

### 1.1.2 Saturation Absorption Spectroscopy

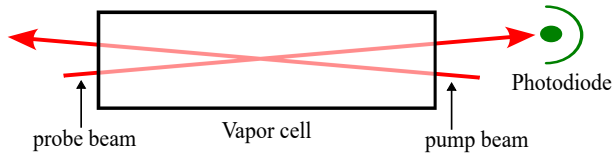


**Figure 1.3:** Basic experimental arrangement for Saturation Absorption Spectroscopy

Saturation Absorption Spectroscopy (SAS) is a well developed technique to get spectral profile of an atomic system [25–27]. In a simple pump-probe scheme, as shown in Fig. 1.3, a weak probe beam passes through the vapor cell with a strong pump beam coming from the opposite direction. Both the pump and probe beams originate from the same laser source, resulting in them having identical frequencies. The role of a strong pump beam is to saturate the atomic gas so that the probe beam becomes transparent. The probe beam’s intensity is measured by the photodiode, which is the SAS signal.

For simplicity, we consider a two level system that has two resonant laser beams (pump and probe) from the same laser to go from ground to excited state, as shown in Fig. 1.4a. The velocities of the atoms within the vapor cell adhere to a

probability distribution known as the Maxwell-Boltzmann distribution. The laser frequency in the lab frame ( $f_{lab}$ ) is shifted to the laser frequency in the frame of atoms ( $f_{atom}$ ) by atoms moving with velocity  $v_{atom}$  due to the Doppler shift.

$$f_{atom} \left(1 - \frac{v_{atom}}{c}\right) = f_{lab} \tag{1.1.1}$$

Where  $c$  is the speed of light. The presence of finite velocities results in an effective broadening of the apparent atomic transition. This leads to the idea of Doppler free spectroscopy, and a second high intensity counter-propagating pump beam, along with a weak probe beam, is sent through the cell. Both beams, resonant to the same atomic transition, interact with the same velocity group of atoms. A bump appears in the spectrum due to the reduction of absorption of probe beam in the presence of a strong pump beam, as shown in Fig. 1.4b. This bump is used as a resonance frequency reference.

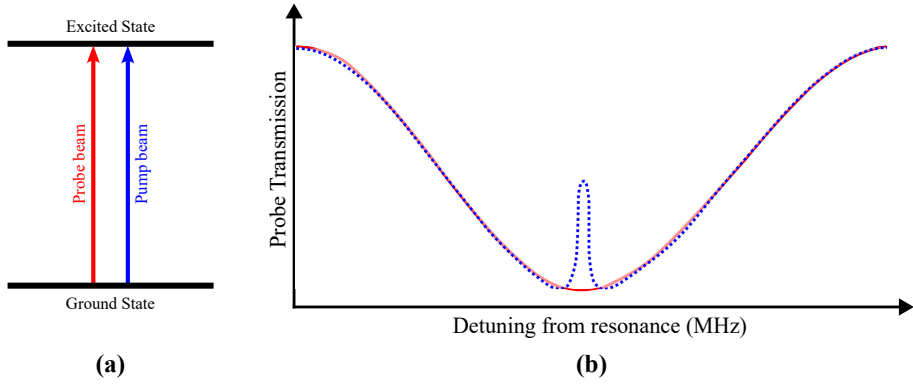


**Figure 1.4:** (a) Simple two level energy level diagram (b) Transmission spectra of the probe beam; the blue dotted line is in the presence of a pump beam, whereas the red line is only a probe beam.

### Experimental Setup

A laser beam of 780 nm from the master laser of a tapered amplifier based laser system (TA100, Toptica Inc.) passes through an optical window and a transmitted beam is used as the pump beam. The pump beam passes through a Half-wave plate (HWP) and Polarizing beam splitter (PBS) to get P-polarized beam. The

pump beam ( $780 \mu\text{W}$ ) passes through an Rb vapor cell that measures 5 cm in length and 2.5 cm in diameter. The beam then double passes through the neutral density filter (NDF) and quarter-wave plate (QWP) by reflecting back through a mirror that makes it an S-polarized probe beam ( $332.3 \mu\text{W}$ ). The probe beam passes in a counter-propagating direction of the pump beam through the Rb vapor cell and gets reflected by the PBS to be detected by the photodetector (PDA36A-EC, Thorlabs).

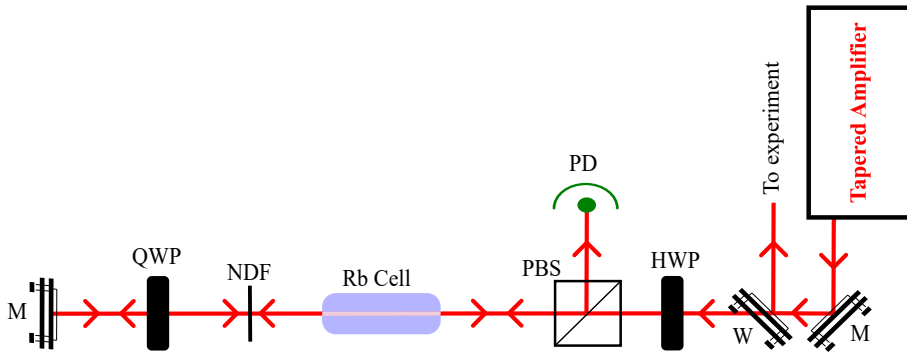


**Figure 1.5:** Schematic diagram of experimental setup. Component symbols: W: window; HWP: half-wave plate; QWP: quarter-wave plate; PBS: polarizing beam splitter; M: mirror; NDF: neutral density filter PD: photo-detector.

### Spectra

The Rb vapor has thermal motion and atoms move at different velocities depending on their temperature and follow the Maxwellian distribution in thermal equilibrium. Because of their motion at certain velocity, atoms in the vapor cell observe shift in frequency of the weak probe laser beam. Instead of three clear lines for  $F_g = 3 \rightarrow F_e = 2, 3, \text{ and } 4$  transition lines, one Doppler broadened line is recorded in presence of just probe beam. The counter-propagating strong pump beam interacts with the same velocity of atoms as the probe beam and saturates these atoms. There is a decrease in absorption of the weak probe beam, which produces a dip in the spectra and is termed a lamb-dip.

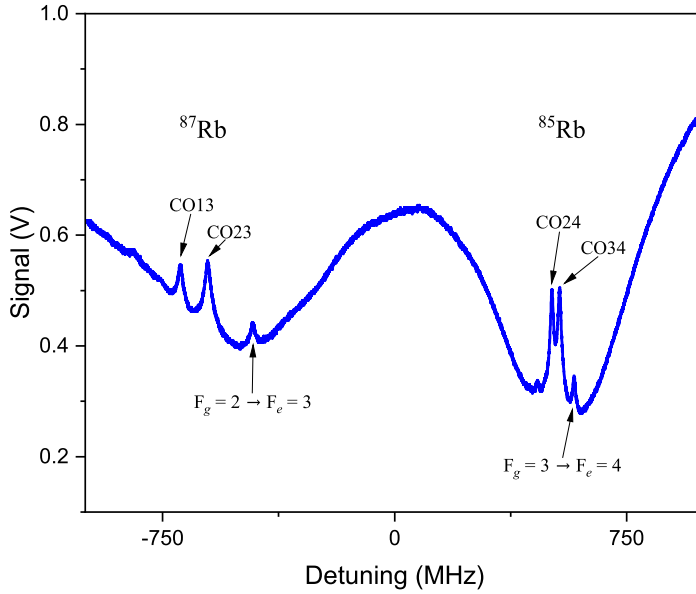


**Figure 1.6:** SAS spectral profile of D2 transition line of Rb atoms

The SAS signal comprising of the lamb-dips for D2 transition lines from  $F_g = 3$  of  $^{85}\text{Rb}$  and  $F_g = 2$  of  $^{87}\text{Rb}$  atoms is shown in Fig. 1.6. The crossover transitions also show up along with the hyperfine transition lines. The pump laser beam frequency ( $f_{lab}$ ) described in Eq. 1.1.1 is red-shifted from the resonant frequency ( $f_r$ ) due to the motion of atoms with a velocity ( $-v_{atom}$ ). Similarly, the probe beam frequency is blue-shifted from the resonant frequency ( $f_b$ ) by the same atoms.

$$f_{atom}\left(1 - \frac{v_{atom}}{c}\right) = f_r$$

$$f_{atom}\left(1 + \frac{v_{atom}}{c}\right) = f_b$$

By adding these two equations,

$$f_{atom} = \frac{(f_r + f_b)}{2} \quad (1.1.2)$$

which indicates that the crossover transition lies exactly between two hyper-fine transition lines.

## 1.2 Magneto-Optical Trapping (MOT)

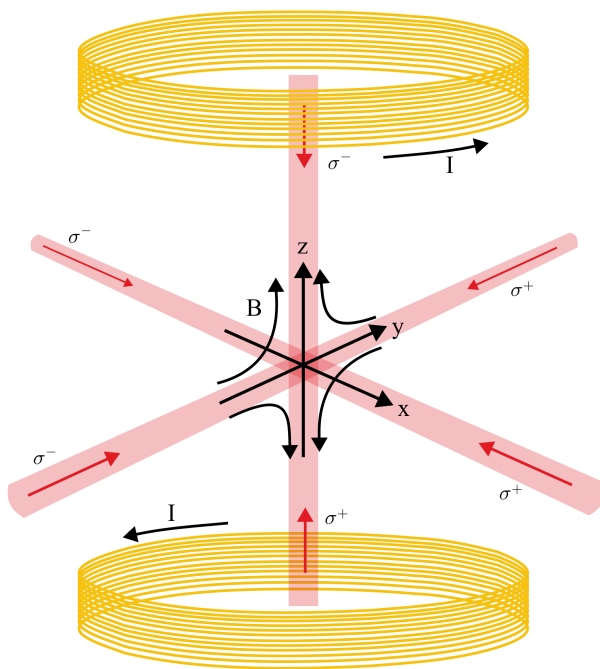


**Figure 1.7:** MOT configuration with three pairs of laser beams and a pair of anti-Helmholtz coils.

The ability to cool and trap neutral atoms with light was first demonstrated in 1987 [28]. The Magneto-Optical Trapping (MOT) employs three pairs of laser beams that are mutually orthogonal and counter-propagating, along with a quadrupole magnetic field, to achieve simultaneous cooling and trapping of the atoms. With one electron in their valance shell, alkali-metal atoms  $^{85}\text{Rb}$  [29–32],  $^{87}\text{Rb}$



[33],  $^{40}\text{K}$  [34],  $^{41}\text{K}$  [35],  $^6\text{Li}$  [36],  $^7\text{Li}$  [37],  $^{23}\text{Na}$  [38] and  $^{133}\text{Cs}$  [39–41] provide a natural choice for cold atom experiments [42]. The cycling transitions from the upper ground states of alkali-metal atoms,  $F_g = 3$  of  $^{85}\text{Rb}$  and  $F_g = 2$  of  $^{87}\text{Rb}$  shown in Figs 1.1 and 1.2, respectively, provide the trapping force. Type-I ( $F_e > F_g$ ) MOTs are extensively studied as the atom is always in a cooling cycle. If the atom decays to another lower state, a repump laser is used to bring it back to the cycle. Whereas type-II ( $F_e \leq F_g$ ) MOTs [32, 43] are more complex as atoms cannot scatter photons continuously without being optically pumped to a dark state and are still not fully understood. For  $F_g = 2 \rightarrow F_e = 1$  cycling transition  $F_e < F_g$ , the ground and excited Zeeman sublevels do not couple, which makes the excited hyperfine level the dark state and do not contribute to the trapping so that weak trapping force happens. Zeeman splitting of cooling transitions, polarization of the laser beams, and mixing of closely spaced hyperfine energy levels play a significant role in trapping force in type-II cooling transitions [44]. Atoms trapped in the  $F_g = 2$  hyperfine ground state form a ring like structure to balance Doppler and Sisyphus forces. In addition to cycling transitions, non-cycling transitions have also been investigated for sodium atoms [45, 46]. Ultracold atoms produced by MOT are utilized for a variety of applications, including quantum information processing [47–51], non-linear optics [52–54], and many-body simulations [55–57].

Since a laser beam may exert a force on an atom in the direction of its propagation, it stands to reason that trapping atoms between two laser beams propagating in opposite directions might be possible. However, the forces would be effectively cancelled out if the laser beams' frequency matched that of the cycle transition. Red detuning of laser beams below the cycling transition frequency is one possible solution to this problem. The idea behind this method stems from the fact that atoms have a specific velocity. By utilizing the Doppler effect on the laser detuning, namely the red detuning, we may alter the equilibrium of power between the two forces. When the beam moves in the opposite direction of the atom, the Doppler shift causes a reduction in the detuning, resulting in an amplified force magnitude. Conversely, the frequency of the second beam will shift

even farther from the transition (blue detuning), leading to a reduction in the force applied to the atom. In this manner, a force term will arise, acting along the axis of propagation for the two beams. In order to achieve a comprehensive three-dimensional setup utilizing this particular technique, it is necessary to employ three pairs of counter-propagating laser beams that are red detuned, with each pair aligned along one of the three mutually perpendicular axes. The atoms will exhibit a stochastic motion like a random walk, akin to their behavior when immersed in a viscous fluid. This phenomenon is commonly denoted as optical molasses [58].

To induce spatial confinement, it is necessary to introduce a magnetic field gradient into the optical molasses. Hence, the utilization of the atom's internal structure is employed to enhance light absorption in close proximity to the trap's center. Let's imagine a simplified situation where we have a one-dimensional magneto-optical trap (MOT) that is aligned in the z-axis. For this configuration, we consider the existence of an atom in its lowest energy level, known as the ground state, with a total angular momentum quantum number  $J = 0$ . likewise an atom in its higher energy state, referred to as the excited state, has  $J = 1$ . The magnetic field is denoted by the equation  $B_z = bz$  and causes a Zeeman shift in the energy level. The quantum number  $m$  in this simplified system has three possible values: +1, 0, and -1. The polarization of the counter-propagating beams is essential in a magneto-optical trap (MOT). The beam that is traveling in the positive z direction is required to possess right circular polarization  $\sigma^+$ , while the other beam necessitates left circular polarization  $\sigma^-$ . The significance of these polarizations lies in their adherence to the selection rules, which dictate that the  $\sigma^+$  can exclusively induce transition to the  $m = +1$  state, whereas the  $\sigma^-$  can only facilitate the transition to the  $m = -1$  state.

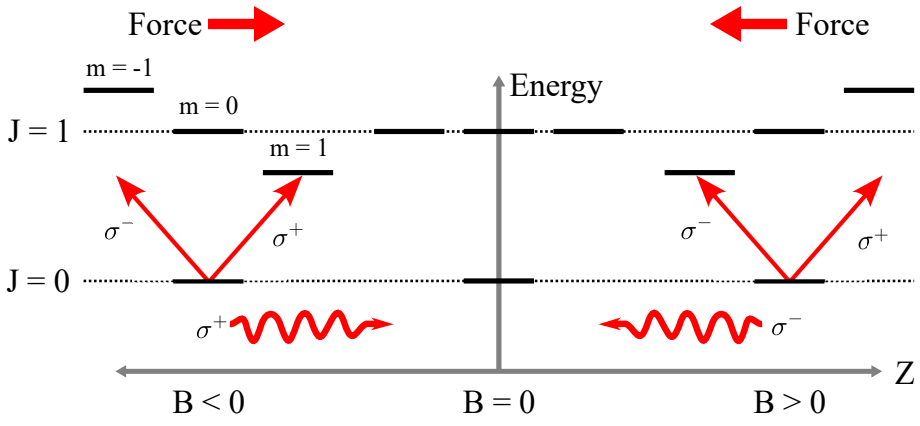


**Figure 1.8:** Energy level diagram of atom under the influence of magnetic field in 1D MOT

The counter-propagating beams bring selection rules into play, which give rise to a force exerted on the atoms, consistently directed towards the center of the trap, as depicted in Fig. 1.8. This force is characterized as the spatial confinement term, which, in conjunction with the damping term, effectively traps the atoms. A complete three-dimensional MOT consists of three orthogonally polarized pairs of counter-propagating beams, along three perpendicular axes. The location of their intersection will occur precisely at the centroid of a "spherical quadrupole" magnetic field, which can be produced by employing a set of anti-Helmholtz coils. The depicted arrangement is illustrated in Fig. 1.7. MOT is the initial stage in the progression towards conducting experiments involving ultracold atoms. This method effectively confines them at a sufficiently low temperature and high density, enabling the utilization of subsequent techniques such as evaporative cooling. In order to ensure proper functionality of the MOT, it is important to employ a repumping frequency aligned with the red-detuned cycle transition. The repumper beam is not red-detuned but plays a crucial role in the operation of a MOT by ensuring that all atoms remain in the cycle transition.

In this thesis, MTS has been utilized to generate a dispers-ive-like tunable reference signal that does not compromise on amplitude and signal gradient for the  $F_g = 3 \rightarrow F_e = 4$  and  $F_g = 2 \rightarrow F_e = 1$ , D2 transition lines of the  $^{85}\text{Rb}$  atom. Furthermore, the Tunable Modulation Transfer Spectroscopy (TMTS) generated

for these transitions are used for Type I and Type II MOT of atoms in the  $F_g = 3$  and  $F_g = 2$  energy levels of the  $5S_{1/2}$  ground state, respectively. In the case of the  $F_g = 2 \rightarrow F_e = 1$  cycling transition, it is observed that the ground and excited Zeeman sublevels do not couple. Consequently, the excited hyperfine level can be considered as the dark state, leading to its inability to contribute to the trapping process. As a result, a weak trapping force is observed.

### 1.3 Electromagnetically Induced Absorption (EIA) and Electromagnetically Induced Transparency (EIT)

Following the observation of electromagnetically induced absorption (EIA) [59] and electromagnetically induced transparency (EIT) [60], many methods have been developed to convert EIA into EIT and vice versa. According to Gozzini *et al.* [61], the magneto-optic resonances have the ability to be tuned in a continuous manner, transitioning from EIT to EIA. This transition is achieved by altering the relative handedness of the circular polarizations of both the coupling and probe beams. The Hanle effect can be tuned from EIT to EIA by manipulating the polarization ellipticity of a control beam [62]. The conversion between EIT and EIA in a three-level lambda system was achieved by introducing a second control beam that propagates in the opposite direction to the first beam [63]. The phenomenon of transitioning from absorption occurring inside transparency to transparency occurring within transparency has been documented in cesium atoms by the manipulation of the probe beam's power [64–66]. Zhukov *et al.* [67] conducted an experiment utilizing the  $D_2$  line of  $^{87}\text{Rb}$  in the Hanle configuration. The researchers investigated the impact of various factors, including intensity, polarization, geometry (co-propagating or counter-propagating), and wavelength of the coupling beam. McGloin *et al.* [68] examined the dependence of polarization on the magnitude dependence of EIT. Sign reversal of EIA had also been studied with orthogonal circularly polarized laser beams by changing the power

of the coupling beam [69]. The study conducted by Song *et al.* [70] investigated the impact of temperature on EIT in cesium (Cs) atoms using linear orthogonal coupling and probing beams. Theoretical investigations have suggested the potential application of a metasurface (MS) with switching capabilities from EIT to EIA in the terahertz region [71]. In their study, Grewal *et al.* [72] investigated the impact of neighboring hyperfine levels on EIA observed in the Hanle configuration. Specifically, they examined the influence of the polarizations of the coupling and probe lasers on the open transitions of the D2 lines of  $^{87}\text{Rb}$ , where  $F_e \leq F_g$ . Nevertheless, it was theoretically infeasible to determine the complete absorption of the entire D2 line by incorporating the Doppler effect due to the computational intricacies associated with its consideration. We conducted an investigation on degenerate two-level systems (DTLS) of Rb atoms in order to get insights into the underlying mechanisms of EIA and EIT [73, 74]. The works stated above did not take into account the neighboring effects in relation to variations of polarization rotation.

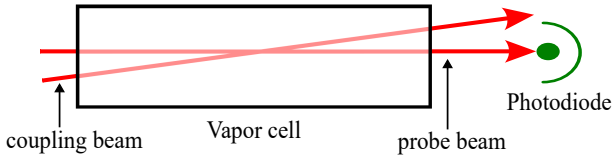


**Figure 1.9:** Basic experimental arrangement for Electromagnetically Induced Absorption and Transparency

Subsequently, it was discerned that in order to comprehend the intricacies of EIA and EIT, it is imperative to examine neighboring degenerate multilevel systems (DMLS) differently from DTLS. [75–78]. The study conducted by Zee-shan *et al.* [76] highlights the significance of both neighboring effects and the polarizations of coupling and probe beams in understanding the mechanisms of EIA and EIT in scenarios involving perpendicular and parallel orientations of linear and circular polarizations. The EIA in  $^{85}\text{Rb}$  atoms can be converted into EIT by artificially enhancing the hyperfine energy separation, provided that the coupling and probe beams have the same circular polarization [77]. Conversely,

the amplitude of EIT decreases when the hyperfine energy splitting of  $^{85}\text{Rb}$  is artificially increased, particularly when the coupling and probe beams have orthogonal circular polarizations [78]. Both EIA and EIT are essential for various applications including slow and fast light generation [79], lasing without inversion [80], precision magnetometry [81–83], high-resolution spectroscopy [84], quantum information science [85–90], enhancement of refractive index [91] and optical switching [92].

In this thesis, we extend the angle between the polarization axis of coupling and probe laser beams to determine the critical angle for the conversion between EIA and EIT considering neighboring effects in the case of linear polarization of the beams as shown in Fig. 1.9. The dependence of angle  $\theta_R$  between the polarization axes of the coupling and probe laser beams in cases where EIT can convert to EIA have also been observed and calculated for the  $^{85}\text{Rb}$  ( $F_g = 3 \rightarrow F_e = 2, 3, \text{ and } 4$ ) in the low power regimes of the coupling ( $50\mu\text{W}$ ) and probe ( $15\mu\text{W}$ ) beams. The polarization of the coupling and probe beams is initially linear parallel; however, the polarization for the coupling beam is changed to the point where both beams are linear orthogonal. EIAs show up above 0 degrees ( $F_g = 3 \rightarrow F_e = 4$ ) and below 10 degrees ( $F_g = 3 \rightarrow F_e = 4$ ) EIT shows up in the experimental results. However, EIAs show up above 10 degrees ( $F_g = 3 \rightarrow F_e = 2 \text{ and } 3$ ) and below 20 degrees ( $F_g = 3 \rightarrow F_e = 2 \text{ and } 3$ ) EIT shows up in the experimental results. In lower ground state hyperfine levels  $^{85}\text{Rb}$  ( $F_g = 2 \rightarrow F_e = 1, 2, \text{ and } 3$ ) all the time EIT shows up regardless of excited state hyperfine levels. The closed transition of  $F_g = 2 \rightarrow F_e = 1$  contributes significantly to EIT. Those experimental trends match well with DMLS calculations considering neighboring states. Additionally, we present the study on the impact of Doppler broadening on EIA and EIT in a degenerate two-level system. Specifically, we analyze the impacts of neighboring transitions on the  $F_g = 2 \rightarrow F_e = 1, 2, \text{ and } 3$  transitions of the D2 line in  $^{87}\text{Rb}$ . The investigation focuses on the examination of two distinct polarization configurations, linear parallel and linear perpendicular, in relation to the coupling and probe lasers. The hyperfine spacings of the  $5P_{3/2}$  state are artificially varied to achieve this. We further demonstrate the correlation between

the spectral features and the hyperfine spacing for circular parallel and circular orthogonal polarizations of coupling and probe. This correlation is determined by intentionally manipulating the hyperfine spacing of  $^{85}\text{Rb}$  atoms.

## 1.4 Organization of Dissertation

The remaining thesis is organized as follows:

- i) **Chapter 2** presents MTS and TCMTS for cyclic transitions of D2 line. Detail overview of basic model of MTS and experimental results of TCMTS are presented.
- ii) **Chapter 3** extends the MTS by incorporating its ability to tune light and presents MOT by stabilizing trap laser with TMTS. Type I and Type II MOT of  $^{85}\text{Rb}$  are presented.
- iii) **Chapter 4** aims to address the role of angle between the polarization axis of coupling and probe laser beams and neighboring hyperfine transitions to control EIA and EIT. Presents a comparison between theoretical and experimental results.
- iv) **Chapter 5** explores the effects on EIA and EIT due to neighboring transitions by artificially varying the hyperfine spacings.

# Two-color Modulation Transfer Spectroscopy

## 2.1 Overview

The stability of frequency against fluctuations is of significant importance in experiments conducted in the field of atomic and molecular physics. Modulation transfer spectroscopy (MTS) is a technique that produces a dispersive-like signal devoid of background noise in closed systems. This method is particularly valuable in scenarios involving multiple closely spaced hyperfine energy levels. In this chapter, we investigate the MTS signal for  $5^2S_{1/2} (F_g = 3) \rightarrow 5^2P_{3/2} F_e = 4$  of  $^{85}\text{Rb}$  and  $5^2S_{1/2} (F_g = 2) \rightarrow 5^2P_{3/2} F_e = 3$  of  $^{87}\text{Rb}$  atoms in a pump-probe scheme. Furthermore, MTS is extended to two-color MTS (TCMTS), where modulated pump beam is scanning across transitions from  $5^2S_{1/2} (F_g = 3)$  ground hyperfine state of D2 transition line of  $^{85}\text{Rb}$  and probe beam is fixed at  $5^2S_{1/2} (F_g = 3) \rightarrow 5^2P_{3/2} F_e = 2, 3,$  and  $4$  transition lines in three experimental arrangements. For  $^{87}\text{Rb}$  atoms, modulated pump beam is scanning across transitions from  $5^2S_{1/2} (F_g = 2)$  ground hyperfine state of D2 transition line and probe beam is fixed at  $5^2S_{1/2} (F_g = 2) \rightarrow 5^2P_{3/2} F_e = 1, 2,$  and  $3$  transition lines in three experimental arrangements.

This chapter is organized as follows: Section 2.2 presents background of MTS, experimental setup and MTS signal recorded for  $F_g = 3 \rightarrow F_e = 4$  transition of  $^{85}\text{Rb}$  atoms and  $F_g = 2 \rightarrow F_e = 3$  transition of  $^{87}\text{Rb}$  atoms. Section 2.3 covers TCMTS signal for  $F_g = 3 \rightarrow F_e = 2, 3,$  and  $4$  transitions of  $^{85}\text{Rb}$  atoms and  $F_g = 2 \rightarrow F_e = 1, 2, 3$  transitions of  $^{87}\text{Rb}$  atoms, while Section 2.3 presents some concluding remarks.

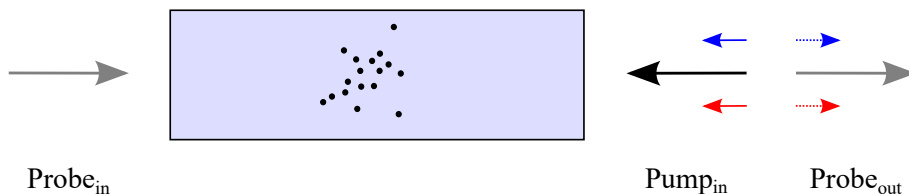
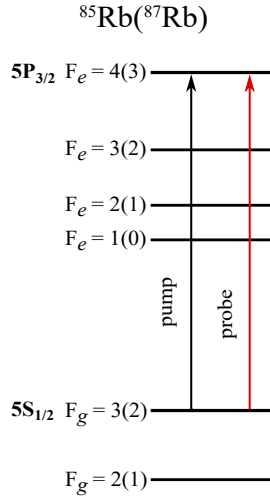


Figure 2.1: Schematic diagram of basic MTS setup.



## 2.2 Modulation Transfer Spectroscopy



**Figure 2.2:** Energy level diagram of MTS. The pump beam is modulated by EOM.

In a pump-probe scheme, as shown in Fig. 2.2, a strong pump beam traverses an Electro-Optic Modulator (EOM), which is controlled by an oscillator operating at a frequency denoted as  $f_m$ . The phase-modulated light that is transmitted can be characterized by a carrier frequency denoted as  $f_c$ , along with sidebands that are spaced apart by the modulation frequency  $f_m$ . If a sinusoidal modulation with a frequency of  $f_m$  and a modulation index of  $\beta$  is incorporated, the optical field of the pump beam with a carrier frequency of  $f_c$  can be expressed as

$$E = E_0 e^{i(f_c t + \beta \sin(f_m t))} \quad (2.2.1)$$

The Fourier transformation gives

$$\begin{aligned}
 E = E_0 e^{i f_c t} \{ & J_0(\beta) + J_1(\beta) e^{i f_m t} - J_{-1}(\beta) e^{-i f_m t} \\
 & + J_2(\beta) e^{2i f_m t} + \dots \} \quad (2.2.2a)
 \end{aligned}$$

Here  $J_n(\beta)$  are Bessel functions. The higher order terms can be ignored for  $\beta \ll 1$  as their magnitude is relatively small.

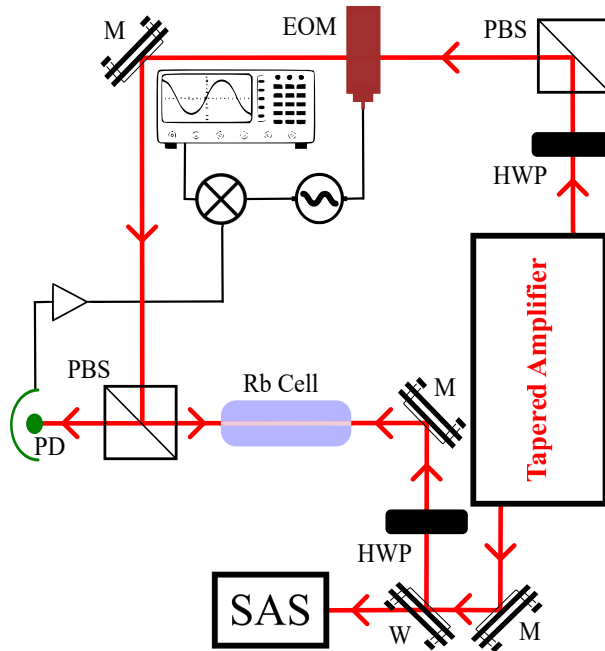
$$E = E_0 \{ J_0(\beta) e^{i f_c t} + J_1(\beta) e^{i(f_c + f_m)t} - J_{-1}(\beta) e^{i(f_c - f_m)t} \} \quad (2.2.2)$$

The presence of three distinct frequency components  $f_c$ ,  $f_c + f_m$  and  $f_c - f_m$  in the beam can be inferred from the expansion following phase modulation. The two components  $f_c + f_m$  and  $f_c - f_m$  are referred to as "sidebands," as they are positioned on either side of the major frequency component, with their placement determined by the modulation frequency  $f_m$ . The modulated pump beam transfers this modulation to counter-propagating probe beam in the vapor cell by a nonlinear interaction called four wave mixing as shown in Fig. 2.1. The signal recorded by detector is obtained by  $S(f_m) = |E|^2$

## 2.2.1 Experimental Setup

A laser beam of 780 nm from the master laser of a tapered amplifier based laser system (TA100, Toptica Inc.) passes through an optical window to reflect the low power beam to be used as a probe beam measuring 130  $\mu\text{W}$  using a power meter (PM100D with photodiode power sensor S130C, Thorlabs) right before the Rb vapor cell as shown in Fig. 2.3. The vapor cell measures 10 cm in length and 2.5 cm in diameter, and the experiment is performed at 20<sup>0</sup> C room temperature. The transmitted part of the beam from the optical window is used for the reference SAS setup. The amplified beam from the tapered amplifier passes through a Half-wave plate and a polarizing beam splitter (PBS) to get an S-Polarized pump beam. The pump beam passes through an electro-optic modulator (EOM, PM7-NIR\_5, QUBIG) connected to the function generator (DG1022, RIGOL) through a 50 OHM low-pass filter (SLP-1.9+, Mini Circuits). The second channel of the function generator is connected to the phase detector (ZRPD-1+, Mini Circuits), feeding a sinusoidal wave of 5.11 MHz to both the EOM and phase detector. The modulated pump beam (559.5  $\mu\text{W}$ ) passes through the Rb vapor cell in the counter-propagating direction of the probe beam. Both the S-Polarized pump and

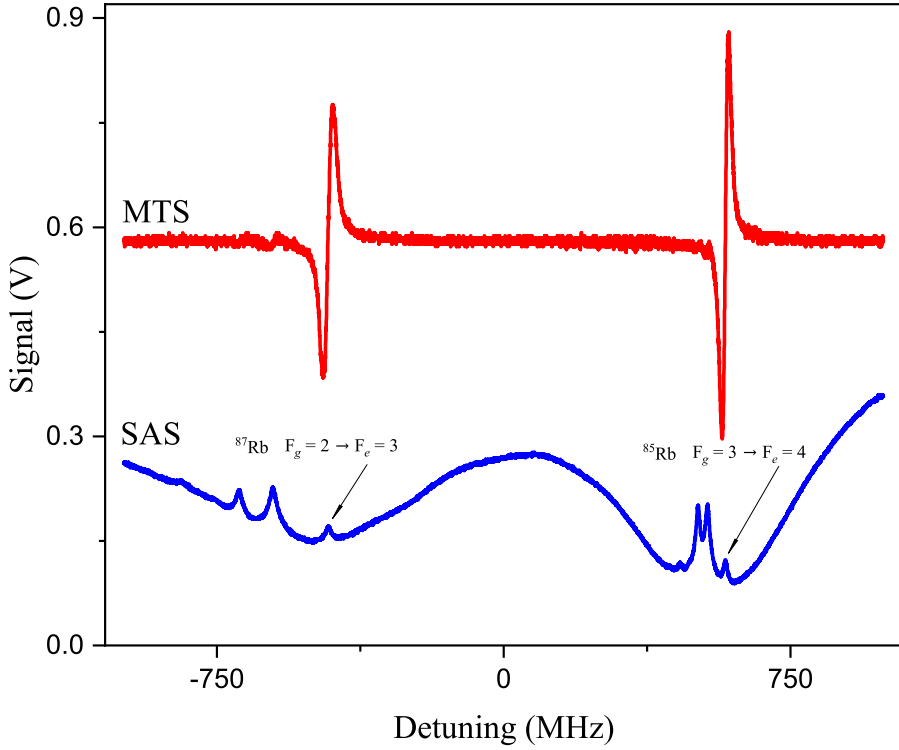
P-Polarized probe beams measure 4.2 mm in diameter. The probe beam falls on the photodetector (PDA8A2, Thorlabs). The output of the photodetector is amplified by an amplifier (ZFL-500, Mini Circuits) and connected to the phase detector through a 50 OHM low-pass filter (SLP-1.9+, Mini Circuits). The output of the phase detector is our MTS signal.



**Figure 2.3:** Schematic diagram of experimental setup. Component symbols: SAS: saturation absorption spectroscopy; W: window; HWP: half-wave plate; PBS: polarizing beam splitter; EOM: electro-optic modulator; M: mirror; PD: photo-detector.

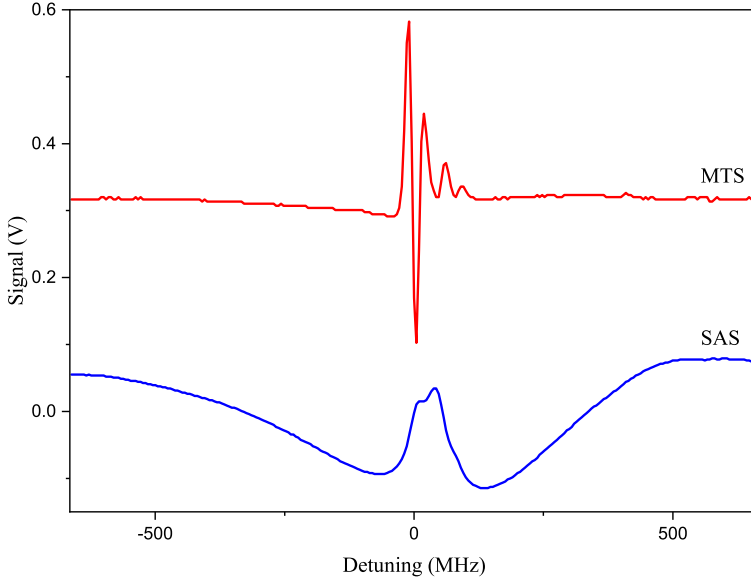
## 2.2.2 Results and Discussion

Fig. 2.4 shows MTS and SAS signal for the  $^{85}\text{Rb } F_g = 3 \rightarrow F_e = 4$  and  $^{87}\text{Rb } F_g = 2 \rightarrow F_e = 3$  transitions of rubidium. The MTS signal has a consistently flat characteristic with a background signal that is negligible. The reason for this phenomenon is because modulation transfer occurs exclusively when the sub-Doppler resonance condition is met. As a result, the stability of the baseline is largely unaffected by the residual linear-absorption effect.



**Figure 2.4:** Comparison between SAS and MTS signals for the  $^{85}\text{Rb } F_g = 3 \rightarrow F_e = 4$  and  $^{87}\text{Rb } F_g = 2 \rightarrow F_e = 3$  transitions

The MTS signal is characterized by a single zero crossing, which exhibits a substantial peak-to-peak amplitude for transitions between hyperfine states. The signal exhibiting the largest peak-to-peak amplitude consistently corresponds to the closed transition. This can offer benefits, especially when dealing with several closely spaced hyperfine transitions, such as the transitions  $^{85}\text{Rb } F_g = 2 \rightarrow F_e = 1$  shown in Fig 2.5. The hyperfine spacing for  $^{85}\text{Rb } F_g = 2 \rightarrow F_e = 1$  is small in comparison to  $^{85}\text{Rb } F_g = 3 \rightarrow F_e = 4$  plus the ground state hyperfine energy levels are not coupled to the excited state hyperfine energy levels ( $F_g > F_e$ ) making it hard to record the spectral features.



**Figure 2.5:** Comparison between SAS and MTS signals for  $^{85}\text{Rb } F_g = 2 \rightarrow F_e = 1$  transition.

## 2.3 Two-color Modulation Transfer Spectroscopy

MTS is useful for active frequency stabilization because it facilitates the frequency-dependent transfer of modulation from the pump to the probe beam without directly modulating the probe beam. Advantage of multi-color MTS is that various configuration of pump and probe beams can be prepared. Thus, the spectra with sub-Doppler linewidths can be obtained for the various transitions in the various range of energy and configuration. We demonstrate V-type of TCMTS experimentally and theoretically for D2 line of Rb atoms considering Zeeman sublevels to solve optical Bloch equation, where probe beam is resonant on  $F_g = 3 \rightarrow F_e = 2, 3,$  and  $4$  transition of  $^{85}\text{Rb}$  and  $F_g = 2 \rightarrow F_e = 1, 2$  and  $3$  of  $^{87}\text{Rb}$  with scanning and modulating pump beam across  $F_g = 3 \rightarrow F_e = 4$  transition of  $^{85}\text{Rb}$  and  $F_g = 2 \rightarrow F_e = 3$  of  $^{87}\text{Rb}$ , respectively, as shown in Fig. 2.6. We realize that TCMTS signals of transitions of  $^{85}\text{Rb}$  and  $^{87}\text{Rb}$  behave differently in comparison largely due to the difference in hyperfine spacing.

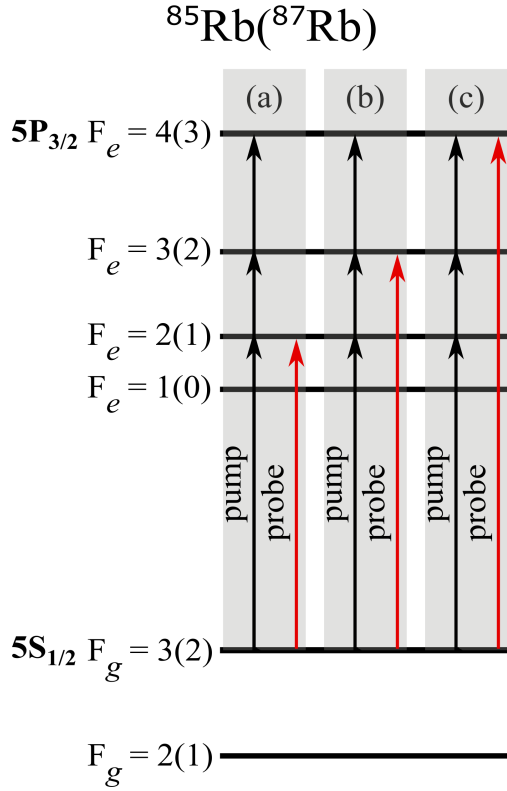


**Figure 2.6:** Energy Level diagram of TCMTS. The modulated pump beam is scanning across transitions from  $F_g = 3$  ( $F_g = 2$ ) of  $^{85}\text{Rb}$  ( $^{87}\text{Rb}$ ) atoms whereas, the probe beam is fixed at (a)  $F_g = 3 \rightarrow F_e = 2$  ( $F_g = 2 \rightarrow F_e = 1$ ) (b)  $F_g = 3 \rightarrow F_e = 3$  ( $F_g = 2 \rightarrow F_e = 2$ ), and (c)  $F_g = 3 \rightarrow F_e = 4$  ( $F_g = 2 \rightarrow F_e = 3$ ) resonance lines of  $^{85}\text{Rb}$  ( $^{87}\text{Rb}$ ) atoms.

### 2.3.1 Experimental Setup

The laser beam of 780 nm from an external cavity diode laser (DLpro, Toptica Inc.) passes through an optical window, and the reflected part is used for SAS setup. The SAS signal is fed to the diode laser controller (DLCpro, Toptica Inc.) for frequency stabilization. The transmitted part from the optical window passes through a Halfwave plate (HWP) and the polarizing beam splitter (PBS), and the P-polarized beam is the probe beam for the experiment.

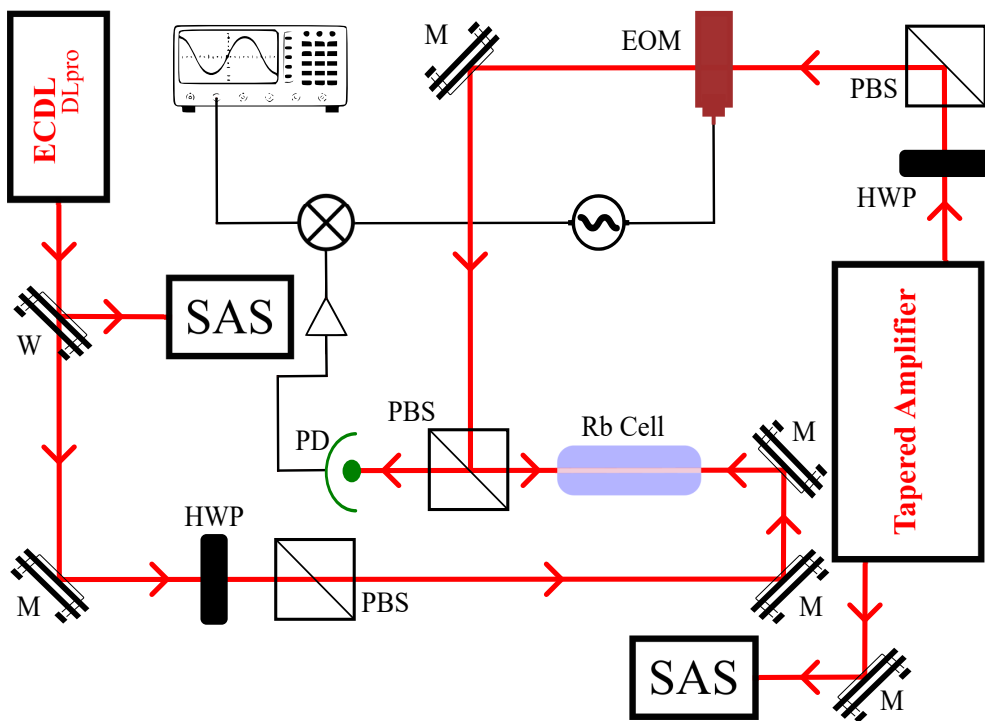


**Figure 2.7:** Schematic diagram of experimental setup. Component symbols: SAS: saturation absorption spectroscopy; W: window; HWP: half-wave plate; PBS: polarizing beam splitter; EOM: electro-optic modulator; M: mirror; PD: photo-detector.

Another beam of the same wavelength from a tapered amplifier based laser system (TA100, Toptica Inc.) passes through a pair of HWP and PBS, and the S-polarized beam is passed through an electro-optic modulator (EOM, PM7-NIR\_5, QUBIG) as shown in Fig. 2.7. The modulated beam is the pump beam for the experiment. The pump beam in the counter-propagating direction of the probe beam passes through the Rb vapor cell, which measures 10 cm in length and 2.5 cm in diameter. The diameter of both the S-polarized pump ( $559.5 \mu\text{W}$ ) and P-polarized probe ( $130 \mu\text{W}$ ) beams is 4.2 mm and the experiment is performed at  $20^{\circ}\text{C}$  room temperature. The test beam from the master laser of TA100 is used for the reference SAS setup for the pump beam. The photodetector (PDA8A2, Thorlabs) receives the probe beam and feeds the output to an amplifier (ZFL-500, Mini Circuits), which is connected to a 50 OHM low-pass filter (SLP-1.9+,

Mini Circuits) and then connected to a phase detector (ZRPD-1+, Mini Circuits). A function generator (DG1022, RIGOL) feeds a sinusoidal wave of 5.11 MHz to both the EOM and phase detector. The output of the phase detector with another 50 OHM low-pass filter (SLP-1.9+, Mini Circuits) is our TCMTS signal.

### 2.3.2 Results and Discussion

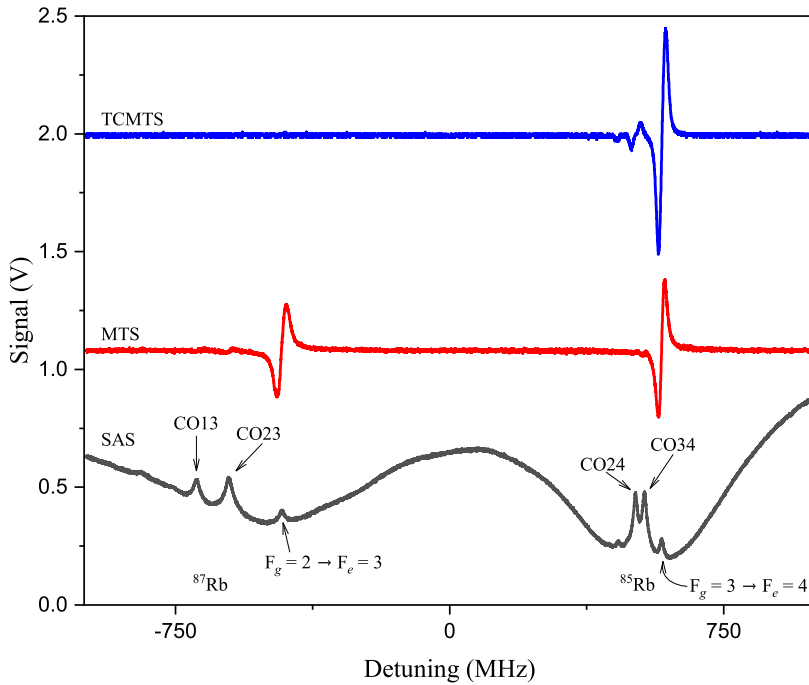


**Figure 2.8:** Comparison of SAS, MTS, and TCMTS signals

We conducted two cases of V-type TCMTS experiment. In the first experiment, we probed the resonant excited states originating from the higher ground state of  $^{85}\text{Rb}$  D2 transition line, while the pump beam scanning through the transition from  $^{85}\text{Rb}$   $F_g = 3$  hyperfine ground state. In the second experiment, we probed the resonant excited states originating from the higher ground state of  $^{87}\text{Rb}$  D2 transition line, while the pump beam scanning across the transition from  $F_g = 2$  hyperfine ground state.



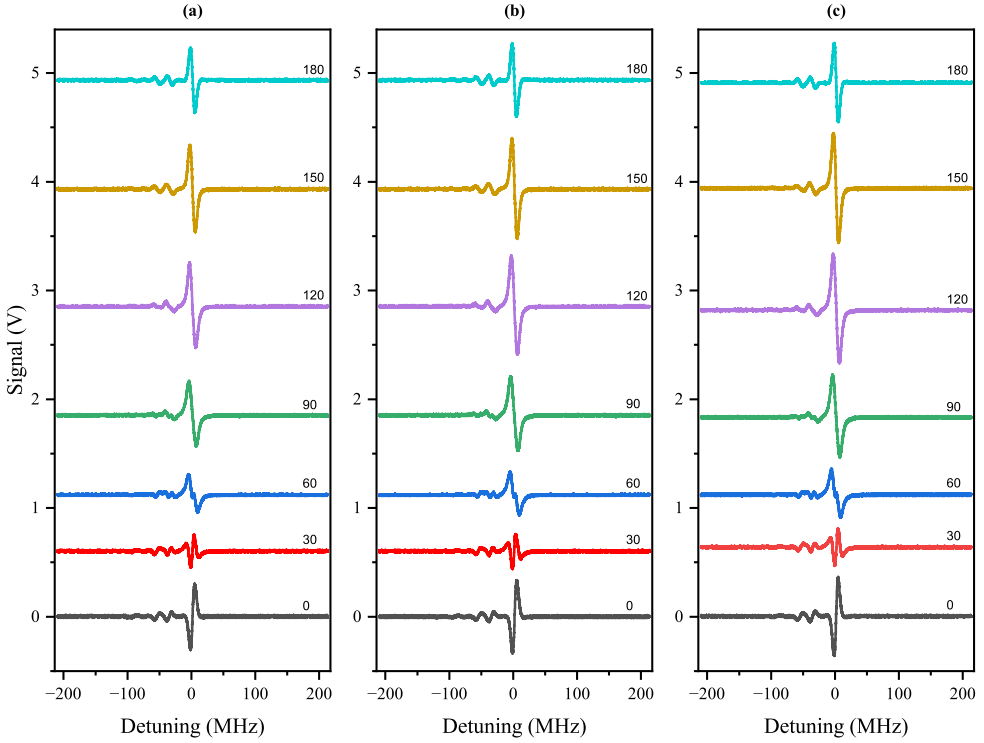


**Figure 2.9:** TCMTS signals with phase  $\phi = 0$  to  $180$  of (a) probe beam is fixed at  $^{85}\text{Rb } F_g = 3 \rightarrow F_e = 2$  transition while pump beam is scanning across the transitions from  $^{85}\text{Rb } F_g = 3$ , (b) probe beam is fixed at  $^{85}\text{Rb } F_g = 3 \rightarrow F_e = 3$  transition while pump beam is scanning across the transitions from  $^{85}\text{Rb } F_g = 3$ , and (c) probe beam is fixed at  $^{85}\text{Rb } F_g = 3 \rightarrow F_e = 4$  transition while pump beam is scanning across the transitions from  $^{85}\text{Rb } F_g = 3$ .

Fig. 2.8 presents a comparison between SAS, MTS, and TCMTS. MTS has both pump and probe beams scanning the transitions from upper ground hyperfine state of D2 transition line whereas TCMTS has only pump beam scanning the transitions from upper ground hyperfine state of D2 transition line. In the experimental results shown in Fig. 2.8, the probe beam for TCMTS is fixed at  $^{85}\text{Rb } F_g = 3 \rightarrow F_e = 4$  transition line. While two MTS signals for  $^{85}\text{Rb } F_g = 3 \rightarrow F_e = 4$  and  $^{87}\text{Rb } F_g = 2 \rightarrow F_e = 3$  transitions show up, just one larger TCMTS signal for  $^{85}\text{Rb } F_g = 3 \rightarrow F_e = 4$  transition show up. This is largely because of the

probe beam fixed at the  $^{85}\text{Rb } F_g = 3 \rightarrow F_e = 4$  transition. TCMTS has advantage over MTS that it only generates signals for transition in consideration and various configuration of pump and probe beams can be prepared.

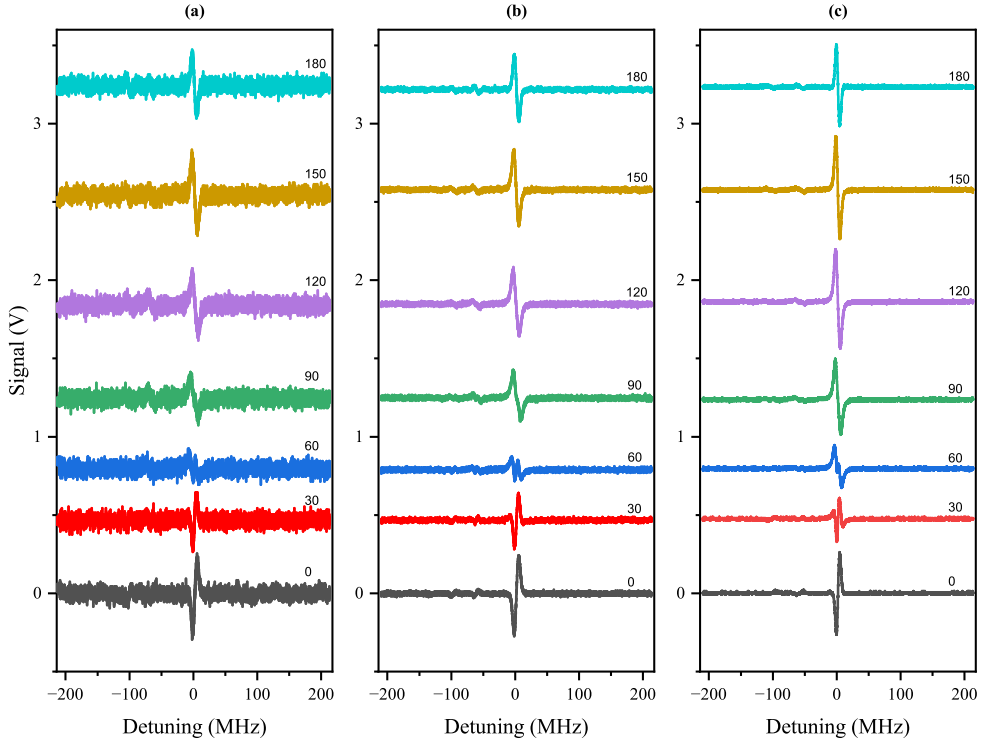


**Figure 2.10:** TCMTS signals with phase  $\phi = 0$  to 180 of (a) probe beam is fixed at  $^{87}\text{Rb } F_g = 2 \rightarrow F_e = 1$  transition while pump beam is scanning across the transitions from  $^{87}\text{Rb } F_g = 2$  (plots are 25 times the original signal), (b) probe beam is fixed at  $^{87}\text{Rb } F_g = 2 \rightarrow F_e = 2$  transition while pump beam is scanning across the transitions from  $^{87}\text{Rb } F_g = 2$  (plots are 6 times the original signal), and (c) probe beam is fixed at  $^{87}\text{Rb } F_g = 2 \rightarrow F_e = 3$  transition while pump beam is scanning across the transitions from  $^{87}\text{Rb } F_g = 2$ .

In the first case of  $^{85}\text{Rb}$  atoms in a pump-probe scheme, the pump beam is scanning the transitions from the upper ground hyperfine state  $F_g = 3$ . The probe beam, in three experimental arrangements, is fixed at three different transitions  $F_g = 3 \rightarrow F_e = 2$ ,  $F_g = 3 \rightarrow F_e = 3$ , and  $F_g = 3 \rightarrow F_e = 4$ , as shown in Fig. 2.9(a-c)

respectively. In Fig. 2.9(a), the TCMTS signal is recorded at phase angle  $\phi = 0, 30, 60, 90, 120, 150,$  and  $180$ . The TCMTS signals generated for the probe beam fixed at  $^{85}\text{Rb } F_g = 3 \rightarrow F_e = 2$  are the smallest in amplitude at each respective phase angle. As we go on to the probe beam fixed at  $^{85}\text{Rb } F_g = 3 \rightarrow F_e = 3$  transition shown in Fig. 2.9(b) the amplitude of TCMTS signals gets larger at each respective phase angle. So is the arrangement of pump beam fixed at  $^{85}\text{Rb } F_g = 3 \rightarrow F_e = 3$  shown in Fig. 2.9(c) which has the largest amplitude at each respective phase angle among the three transitions. The TCMTS signal at  $\phi = 150$  degrees has the largest amplitude of all three experimental arrangements. There could be two factors associated with the difference in amplitude of the three transitions. First, the MTS generates a signal only for the closed transitions due to the nonlinear interaction between the pump and probe beams in the vapor cell, which is also termed as the four wave mixing. Both  $F_g = 3 \rightarrow F_e = 2$  and  $F_g = 3 \rightarrow F_e = 3$  are open transitions, and the nonlinear interaction between the pump and probe beams could be weak. Secondly, Doppler broadening may effect the strength of TCMTS as the hyperfine splitting between  $F_e = 4$  and  $F_e = 2$  is larger than that of  $F_e = 4$  and  $F_e = 3$  and conversely, the TCMTS signals for  $F_g = 3 \rightarrow F_e = 2$  are smaller than that of  $F_g = 3 \rightarrow F_e = 3$ .

In the second case of  $^{87}\text{Rb}$  atoms, the pump beam beam is scanning across the transitions from the upper hyperfine ground state  $F_g = 2$ . The probe beam is fixed at three transitions  $F_g = 2 \rightarrow F_e = 1, F_g = 2 \rightarrow F_e = 2,$  and  $F_g = 2 \rightarrow F_e = 3,$  as shown in Fig. 2.10(a-c) respectively, in three experimental arrangements. Similar to  $^{85}\text{Rb}$  atoms, the TCMTS signals generated at  $\phi = 0, 30, 60, 90, 120, 150,$  and  $180$  by fixing the probe beam at  $F_g = 2 \rightarrow F_e = 1$  transition are the weakest as shown in Fig. 2.10(a). However, the difference in amplitudes is larger than that of  $^{85}\text{Rb}$ , as shown in Fig. 2.11. The amplitudes of TCMTS  $F_g = 2 \rightarrow F_e = 2$  shown in Fig. 2.10(b) is larger than  $F_g = 2 \rightarrow F_e = 1$  and  $F_g = 2 \rightarrow F_e = 3$  has the strongest signals at each respective phase angle, as shown in Fig. 2.10(c). The difference in amplitude is larger because of the the difference in hyperfine splitting of  $^{85}\text{Rb}$  and  $^{87}\text{Rb}$ .

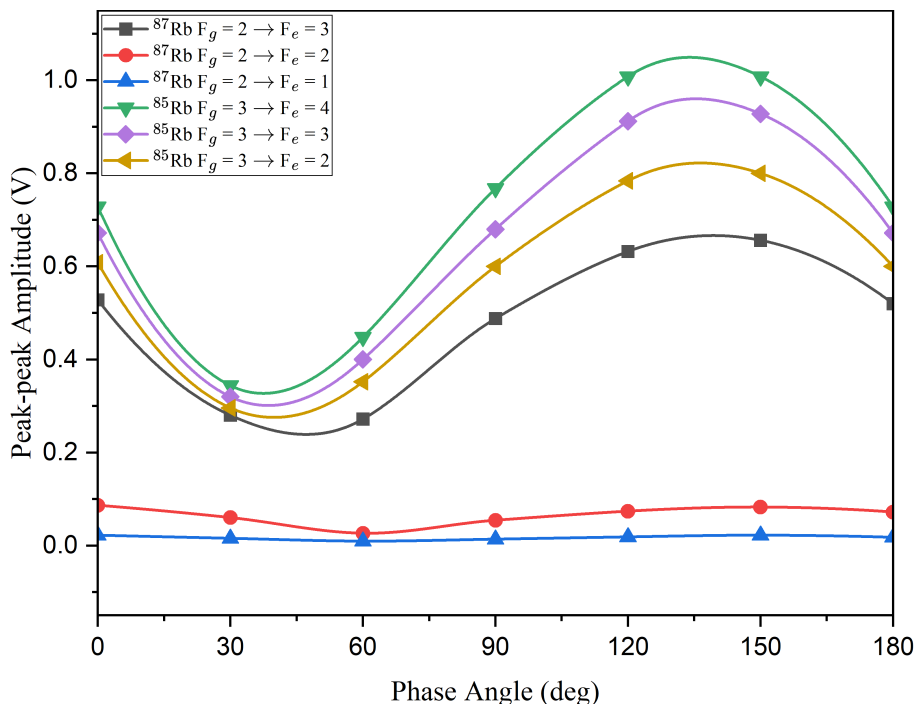


**Figure 2.11:** Comparison of TCMTS signals with probe beam fixed at  $^{87}\text{Rb } F_g = 2 \rightarrow F_e = 1, 2,$  and 3 resonance lines with pump beam scanning across transitions from  $F_g = 2,$  and  $^{85}\text{Rb } F_g = 3 \rightarrow F_e = 2, 3,$  and 4 resonance lines with pump beam scanning across transitions from  $F_g = 3.$

## 2.4 Summary

The dispersive-like nature of the MTS signal is demonstrated for the D2 transition line of Rb atoms. MTS generates a distinct line with a single zero crossing and substantial peak-to-peak amplitude for a closed transition between hyperfine states. The MTS signals are generated for the  $F_g = 3 \rightarrow F_e = 4$  transition of  $^{85}\text{Rb}$  and the  $F_g = 2 \rightarrow F_e = 3$  transition of  $^{87}\text{Rb}$  atoms. In addition, an MTS signal for the  $F_g = 2 \rightarrow F_e = 1$  transition of  $^{85}\text{Rb}$  atoms is shown to show that it can produce signals with almost no background for closely spaced hyperfine transitions. Furthermore, MTS is extended to TCMTS with the capability to do MTS for high-lying excited states with various configurations of pump and probe beams. In a total of six experimental arrangements, three for  $^{85}\text{Rb}$  and three for

$^{87}\text{Rb}$  atoms, TCMTS signals are generated. In the first case, the modulated pump beam is scanning across transitions from the upper hyperfine ground state  $^{85}\text{Rb}$   $F_g = 3$ . The probe is fixed at  $F_g = 3 \rightarrow F_e = 2$ ,  $F_g = 3 \rightarrow F_e = 3$ , and  $F_g = 3 \rightarrow F_e = 4$  for three different experimental arrangements. The smallest signal amplitude is recorded when probe beam is fixed at  $F_g = 3 \rightarrow F_e = 2$  transition at respective values of  $\phi$  and probe beam fixed at  $F_g = 3 \rightarrow F_e = 4$  transition produces the strongest TCMTS signals. For  $^{87}\text{Rb}$  atoms, pump beam is scanning across transitions from the upper hyperfine ground state  $F_g = 2$ , whereas probe is fixed at  $F_g = 2 \rightarrow F_e = 1$ ,  $F_g = 2 \rightarrow F_e = 2$ , and  $F_g = 2 \rightarrow F_e = 3$ . Similar to  $^{85}\text{Rb}$  atoms, weakest signal amplitude is recorded when probe beam is fixed at  $F_g = 2 \rightarrow F_e = 1$  transition at respective values of  $\phi$  and probe beam fixed at  $F_g = 2 \rightarrow F_e = 3$  transition produces the strongest TCMTS signals. The difference in the amplitudes is largely due to the fact that  $^{85}\text{Rb}$  and  $^{87}\text{Rb}$  have different hyperfine splitting.

## Chapter 3

# Magneto-optical Trapping

## 3.1 Overview

Incorporating modulation transfer spectroscopy (MTS) can tune a laser beam below the resonance line, which is necessary for laser cooling and trapping experiments. Tunable Modulation Transfer Spectroscopy (TMTS) gives off a signal that has negligible background and a zero crossing that is accurately centered on the resonant closed transition line. The TMTS signal is generated for  $5^2S_{1/2} (F_g = 3) \rightarrow 5^2P_{3/2} F_e = 4$  of  $^{85}\text{Rb}$  and  $5^2S_{1/2} (F_g = 2) \rightarrow 5^2P_{3/2} F_e = 3$  of  $^{87}\text{Rb}$  atoms in a pump-probe scheme. Furthermore, as the main theme of this Chapter is Magneto-Optical trapping (MOT), the TMTS signals are generated and utilized for cooling and trapping of atoms in  $5^2S_{1/2} (F_g = 3)$  and  $5^2S_{1/2} (F_g = 2)$  hyperfine states of  $^{85}\text{Rb}$  atoms.

This chapter is organized as follows: Section 3.2 presents the background and technique to generate TMTS signal. Section 3.3 describes MOT for atoms in upper and lower hyperfine ground state of D2 transition line of  $^{85}\text{Rb}$  atoms. The last Section 3.4 presents some concluding remarks.

## 3.2 Tunable Modulation Transfer Spectroscopy

In experiments where the laser beam's frequency needs to be either shifted down (red detuning) or shifted up (blue detuning) without changing the main frequency of the laser itself, Tunable Modulation Transfer Spectroscopy could play a really important role with the dispersive-like signal it offers. The standard saturation absorption spectroscopy signal for sub-Doppler lineshapes is generated when a probe laser beam is monitored in the presence of a counter propagating pump beam in an atomic or molecular system. Accordingly, TMTS employs a pump-probe scheme where a pump beam is double passed through two acousto-optic modulators (AOM) for frequency tuning and through electro-optic modulator (EOM) for phase modulation. The velocity ( $v_{pm}$ ) group of atoms resonant with

the pump beam can be written as

$$\omega_0 = \omega_L + 2(\omega_1 + \omega_2) + k v_{pm}$$

$$v_{pm} = \frac{1}{k} \{ \omega_0 - \omega_L - 2(\omega_1 + \omega_2) \} \quad (3.2.1)$$

where  $\omega_0$  is the frequency of atomic resonance at which the laser is locked,  $\omega_L$  is the laser frequency and  $\omega_1$  and  $\omega_2$  are the driving frequencies of AOM-1 and AOM-2, respectively. Similarly, the velocity ( $v_{pb}$ ) group resonant with the probe beam can be written as

$$\omega_0 = \omega_L - k v_{pb}$$

$$v_{pb} = \frac{1}{k} (\omega_L - \omega_0) \quad (3.2.2)$$

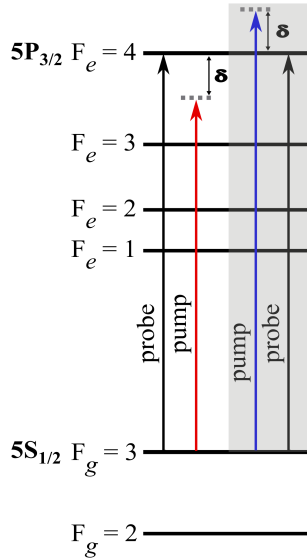


**Figure 3.1:** Energy Level diagram of TMTS. The color of the line indicates whether the laser beam is detuned to the red or blue side of the resonance line in two different experimental setups.

For saturated absorption, both pump and probe beams are resonant with the same velocity group and we can write,

$$v_{pm} = v_{pb}$$

$$\omega_0 - \omega_L - 2(\omega_1 + \omega_2) = \omega_L - \omega_0$$

$$\omega_L = \omega_0 - \delta \tag{3.2.3}$$

where  $\delta = \omega_1 + \omega_2$ . The off-set locking is now possible, where laser frequency is subtracted from  $\omega_0$  by  $\delta$ . Thus, laser scanning frequency depends on  $\delta$ . In two experimental settings, as shown in Fig. 3.1, TMTS signal is generated. The nonlinear process in the vapor cell insures that atom does not relax into other ground state and the baseline stability becomes nearly independent of residual absorption hence, a dispersive like signal with zero background is generated for cyclic atomic transitions.

### 3.2.1 Experimental Setup

A test beam of wavelength 780 nm from a master external cavity diode laser of a tapered amplifier based laser system (TA100, Toptica Inc.) passes through an optical window. The transmitted beam is used for the reference saturation absorption spectroscopy (SAS) setup, while the reflected part is used as a probe beam for TMTS, as shown in Fig. 3.2. The laser beam of the same wavelength coming from a tapered amplifier passes through a half-wave plate (HWP) and polarizing beam splitter (PBS-1) to divide the beam into two components. The P-polarized component of the beam is used for the magneto-optical trap, whereas the S-polarized component is the pump beam for TMTS. The S-polarized beam gets reflected again from PBS-2 and passes through AOM-1 (3080-122, Gooch & Housego), which is fixed at 100 MHz. The -1st order diffracted beam double passes through



a quarter-wave plate (QWP) after reflecting back from the mirror, which changes it to a P-polarized beam. The beam passes through AOM-1 again, and the -1st order diffracted beam, which is now P-polarized, gets transmitted through PBS-2 to pass through AOM-2 (3080-122, Gooch & Housego). The AOM-2 is also fixed at 100 MHz, and the beam double passes through the AOM-2 and the QWP placed next to it and changes back to an S-polarized beam. The beam reflects from PBS-2 now and passes through EOM (PM7-NIR\_5, QUBIG). The modulated beam gets reflected from PBS-3 to go into the Rb cell.

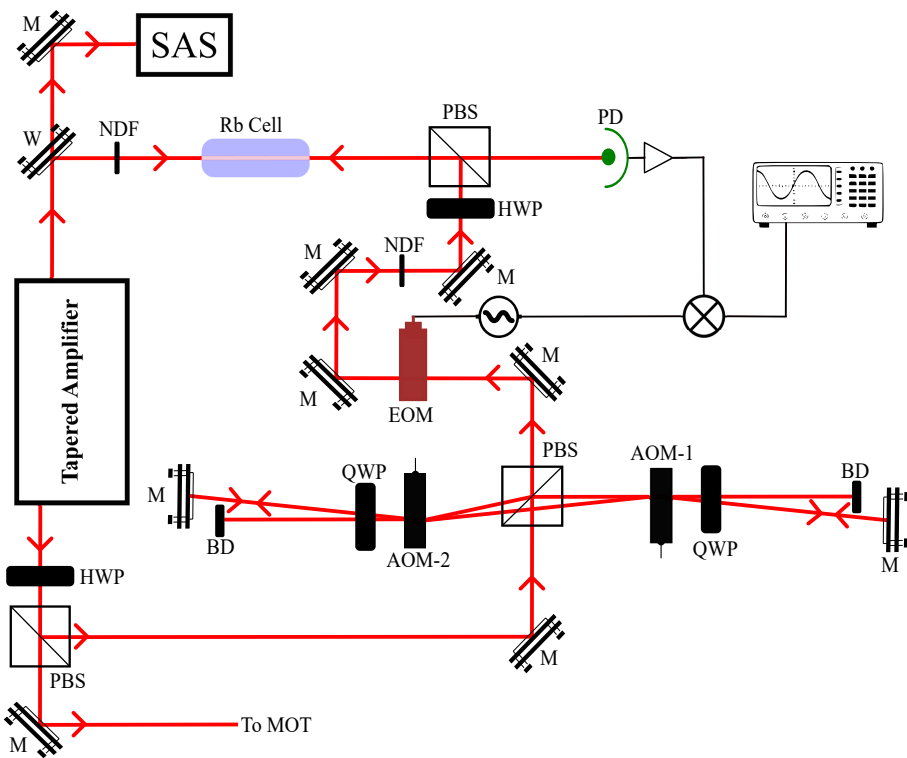


**Figure 3.2:** Schematic diagram of experimental setup. Component symbols: SAS: saturation absorption spectroscopy; NDF: neutral density filter; W: window; HWP: half-wave plate; QWP: Quarter-wave plate; PBS: polarizing beam splitter; AOM: acousto-optic modulator; EOM: electro-optic modulator; M: mirror; BD: beam dump; PD: photo-detector.

The vapor cell measures 10 cm in length and 2.5 cm in diameter and the experiment is performed at 20<sup>0</sup> C room temperature. The diameter of both the S-

polarized pump ( $796 \mu\text{W}$ ) and P-polarized probe ( $100.3 \mu\text{W}$ ) beams is 4.2 mm. The pump beam is detuned by -200 MHz ( $-100-100 = -200$ ). The pump beam transfers modulation to the probe beam, which transmits from PBS-3 and falls on the photodetector (PDA8A2, Thorlabs). The photodetector (PD) output is fed to an amplifier (ZFL-500, Mini Circuits), a 50 OHM low-pass filter (SLP-1.9+, Mini Circuits), and then connected to a phase detector (ZRPD-1+, Mini Circuits). A function generator (DG1022, RIGOL) feeds a sinusoidal wave of 5.11 MHz to both the EOM and phase detector. The output of the phase detector with another 50 OHM low-pass filter (SLP-1.9+, Mini Circuits) is our TMTS signal.

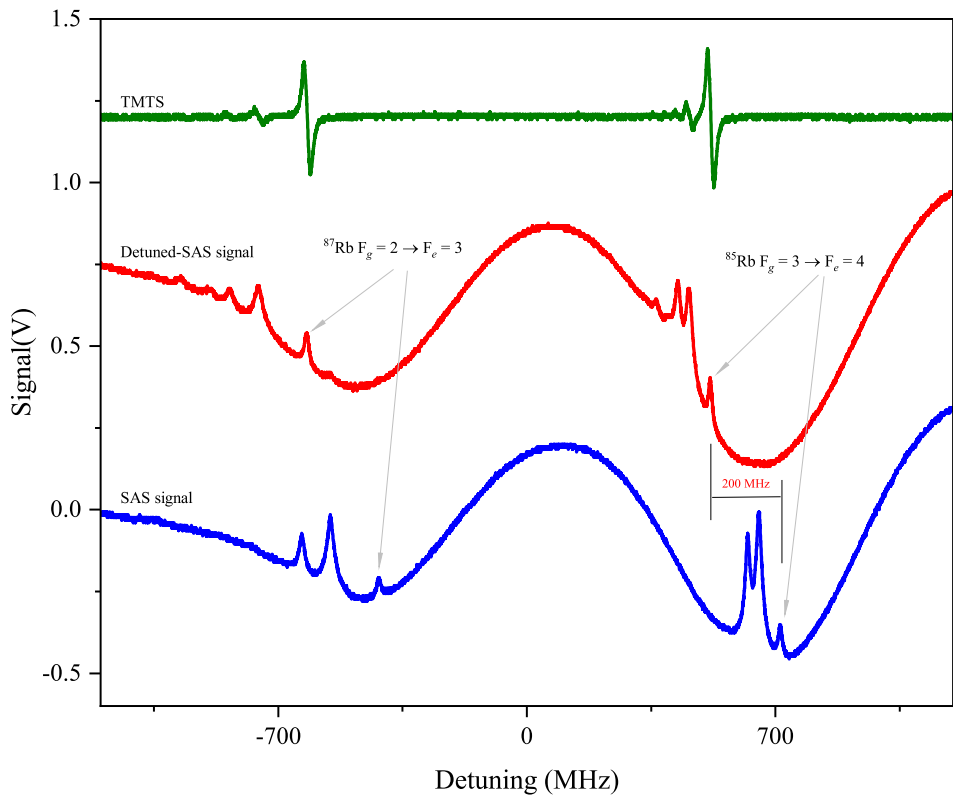


**Figure 3.3:** Comparison of SAS and red detuned SAS and TMTS by 200 MHz. The blue line is SAS signal, red line is detuned SAS signal, and green line is TMTS signal.

### 3.2.2 Results and Discussion

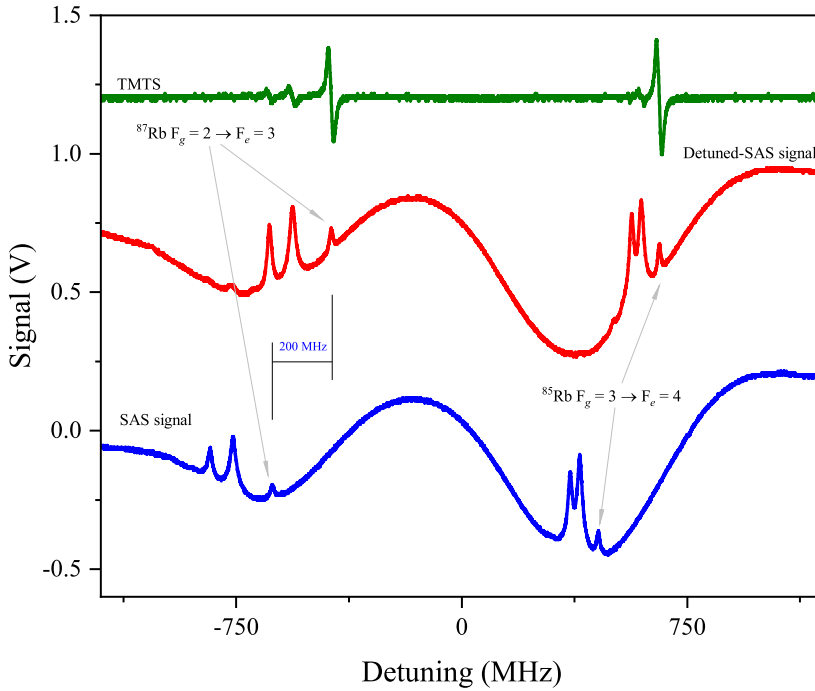


**Figure 3.4:** Comparison of SAS and blue detuned SAS and TMTS by 200 MHz

In the first setting, the pump beam traverses AOM-1 and undergoes reflection, resulting in a double pass through AOM-1. The pump beam then traverses AOM-2 in a double pass configuration. The driving frequency for both AOM-1 and AOM-2 is 100 MHz. The pump beam undergoes a detuning of  $2(100+100)$  MHz as a result of all four instances of the beam going through AOMs utilizing +1 order beam and by Eq. 3.2.3 the pump beam is red detuned by 200 MHz. The red detuned beam passes through EOM for phase modulation and is sent to vapor cell. In a nonlinear process the pump beam transfers modulation to probe beam and dispersive-like TMTS signals are generated with negligible background with

their zero crossings accurately centered on the  $^{85}\text{Rb } F_g = 3 \rightarrow F_e = 4$  and  $^{87}\text{Rb } F_g = 2 \rightarrow F_e = 3$  D2 transition lines, as shown in Fig. 3.3. The blue line is reference SAS signal with zero detuning. The red and green lines are detuned SAS and TMTS signals, respectively. It can be seen clearly that the TMTS signal is shifted to the red side by 200 MHz.

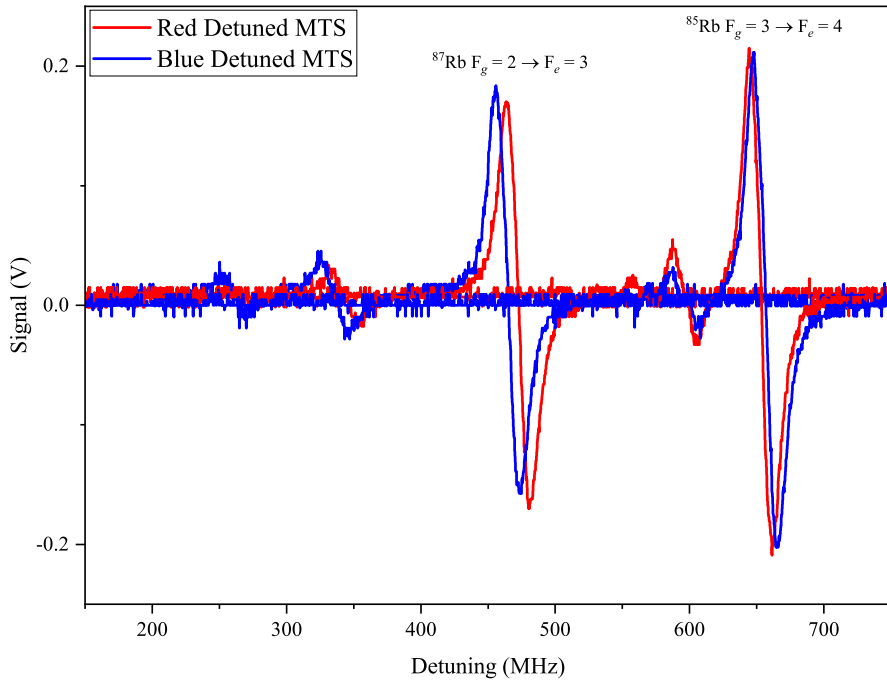


**Figure 3.5:** Comparison between red and blue detuned TMTS signals.

In the second setting, the pump beam traverses AOM-1 and AOM-2 in a double pass configuration. The driving frequency for both AOM-1 and AOM-2 is 100 MHz. The pump beam undergoes a detuning of  $2(-100-100)$  MHz as a result of all four instances of the beam going through AOMs utilizing -1 order beam and by Eq. 3.2.3 the pump beam is blue detuned by 200 MHz. The blue detuned beam is sent through an EOM to induce phase modulation, after which it is subsequently directed towards Rb vapor cell. In a non-linear process, the pump beam facilitates the transfer of modulation to the probe beam, resulting in the generation of dispersive-like TMTS signals for  $^{85}\text{Rb } F_g = 3 \rightarrow F_e = 4$  and  $^{87}\text{Rb } F_g = 2$

→  $F_e = 3$  D2 transition lines, as shown in Fig. 3.4. The blue line is reference SAS signal with zero detuning. The red and green lines are detuned SAS and TMTS signals, respectively. The TMTS signal can be seen to be shifted to the blue side of detuning by 200 MHz with no change in peak to peak amplitude and signal gradient, as shown in Fig. 3.5.

### 3.3 Magneto-Optical Trap

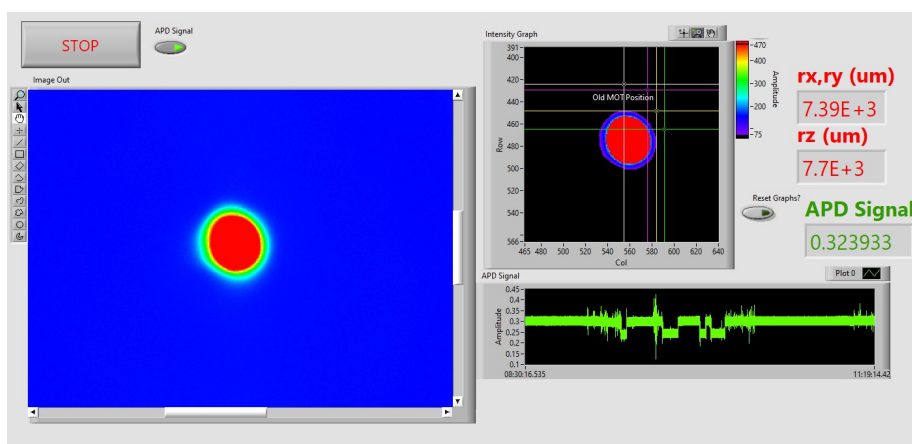
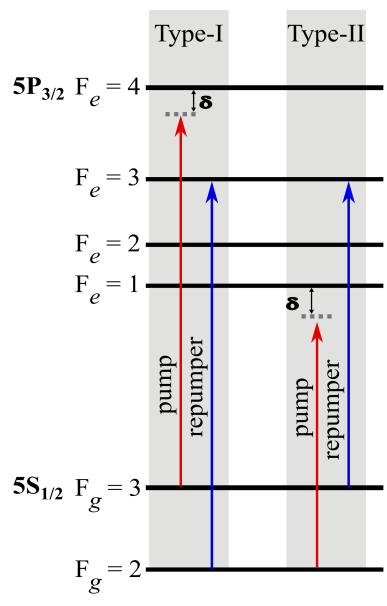


Figure 3.6: GUI for MOT using LabVIEW

The Magneto-Optical Trap (MOT) utilizes two force components to achieve the two different goals of spatially confining and cooling atoms. Given the understanding that a laser beam possesses the capability to apply a force on an atom in alignment with its propagation, it is reasonable to consider the feasibility of confining atoms between two laser beams that propagate in opposite directions. Nevertheless, in the event if the frequency of the laser beams precisely matched that of the cycling transition, the resultant forces would effectively nullify each other. One possible solution to this predicament involves the use of red detuning of laser beams below the cycling transition frequency. The rationale behind this approach lies in the observation that atoms possess a certain velocity, denoted

as  $v$ . By using the Doppler shift in laser detuning, it becomes possible to selectively enhance one force over another. When the beam propagates in the opposite direction of the atom, the Doppler shift will result in a decrease in the detuning, leading to an increase in the force magnitude exerted by the beam. In contrast, the second beam will shift further away from the transition, resulting in a reduction in the force exerted on the atom. Consequently, a force will manifest along the axis of propagation for the two beams. In order to achieve a comprehensive three-dimensional architecture utilizing this particular technique, it is vital to employ three sets of counterpropagating red detuned laser beams along three mutually perpendicular axes. Nevertheless, the force experienced by the atoms is not due to spatial confinement, but rather a damping or viscous factor. Another beam termed as repumper beam is used to bring back those atoms to the cooling cycle that may relax into other ground state after emitting photon.



**Figure 3.7:** Energy level diagram of Type-I and Type-II MOT.

To induce spatial confinement, it is necessary to introduce a magnetic field gradient alongside the optical molasses. Thus, we utilize the internal structure of the atom in order to enhance the absorption of light in close proximity to

the trap's center. The counter-propagating beams give rise to a force exerted on the atoms, consistently directed towards the center of the trap due to selection rules as discussed in Chapter 1. An further crucial aspect to consider in the laser system constructed for this thesis is to the imaging of the atoms and fluorescence detection. With imaging and fluorescence detection it is possible to calculate the number of atoms in the MOT using the following:

$$N = \frac{i}{\gamma_p \frac{L\Omega}{4\pi} \eta_{PD} e} \quad (3.3.1)$$

where  $i$ ,  $\gamma_p$ ,  $L$ ,  $\Omega$ ,  $\eta_{PD}$  and  $e$  are Avalanche photodiode's photocurrent, single atom's scattering rate, optics loss, solid angle, quantum efficiency of detector and charge on an electron, respectively. The imaging using CCD camera, as shown in Fig. 3.6, can be used to determine the volume of MOT by Gaussian fitting and density of trapped atoms can be given by:

$$n = \frac{N}{(2\pi)^{\frac{3}{2}} r_1^2 r_2} \quad (3.3.2)$$

where  $r_1$  is the width and  $r_2$  is the height of the atomic mixture. In order to execute this procedure, a combination of the cycle and repumping transition frequencies are used for D2 transition of Rb atoms, as shown in Fig. 3.7.

### 3.3.1 Experimental Setup

A laser beam of 780 nm from an external cavity diode laser of a tapered amplifier based laser system (TA100, Toptica Inc.) is divided into S-polarized and P-polarized components. The S-polarized part is sent to TMTS setup as described in Sec. 3.2. The P-polarized part is sent to fiber coupler (F810APC-780, Thorlabs) for better beam mode. The beam is expanded to 2 cm in diameter using optical beam expander (GBE03-B, Thorlabs). The beam then is divided into three part to be sent into ultrahigh vacuum chamber (UHVC). A pair of Half-wave plate (HWP) and Quarter-wave plate (QWP) is used for these three trap laser beams to convert the beams from linearly polarized beams to circularly polarized beams of

desired handedness for MOT.

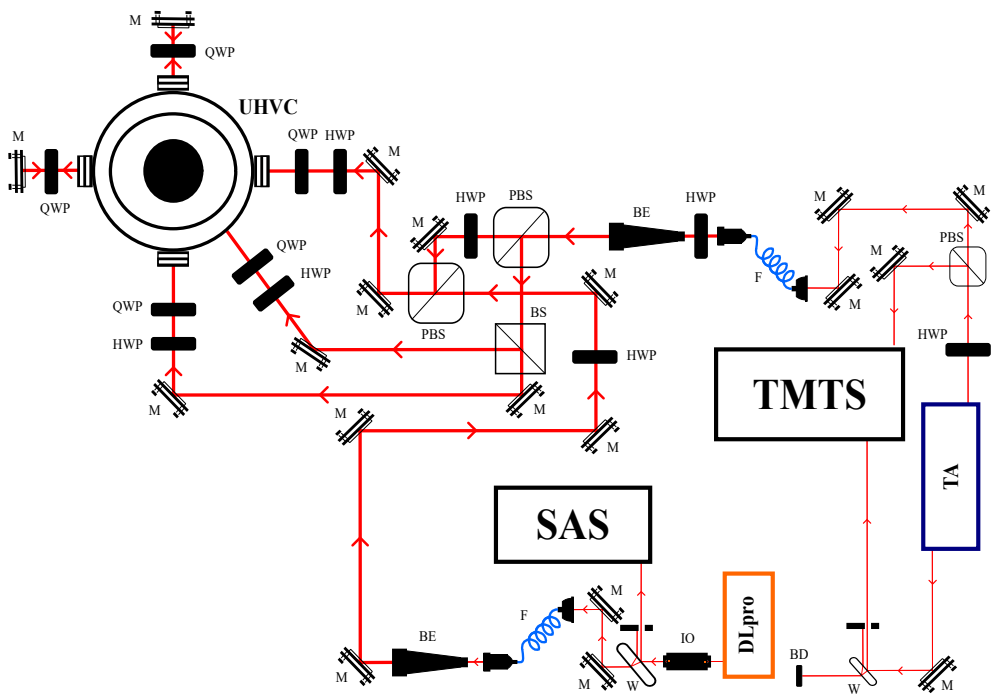


**Figure 3.8:** Schematic diagram of experimental setup. Component symbols: SAS: saturation absorption spectroscopy; TMTS: tunable modulation transfer spectroscopy; W: window; HWP: half-wave plate; QWP: Quarter-wave plate; PBS: polarizing beam splitter; BE: beam expander; M: mirror; OI: optical isolator; BD: beam dump; UHVC: ultra-high vacuum chamber.

The repumper beam of 780 nm from an external cavity diode laser (DLpro, Toptica Inc.) is also fed to fiber coupler (F810APC-780, Thorlabs) and expanded to 2 cm in diameter using lenses. The repumper beam goes into the chamber along one of the trap beams, as shown in Fig. 3.8. The Rb getter enclosed in the UHVC is fed current by an externally connected power supply. The UHVC has a pair of anti-Helmholtz coils to confine the atoms at the center of the chamber. The fluorescence of MOT is measured using Avalanche photodiode (APD, Hamamatsu C5460-01) and MOT imaging is facilitated by CCD (acA1300-30gm, Basler) camera. Hardware interfacing is done using LabVIEW for APD and CCD camera, as shown in Fig. 3.6.



### 3.3.2 Results and Discussion

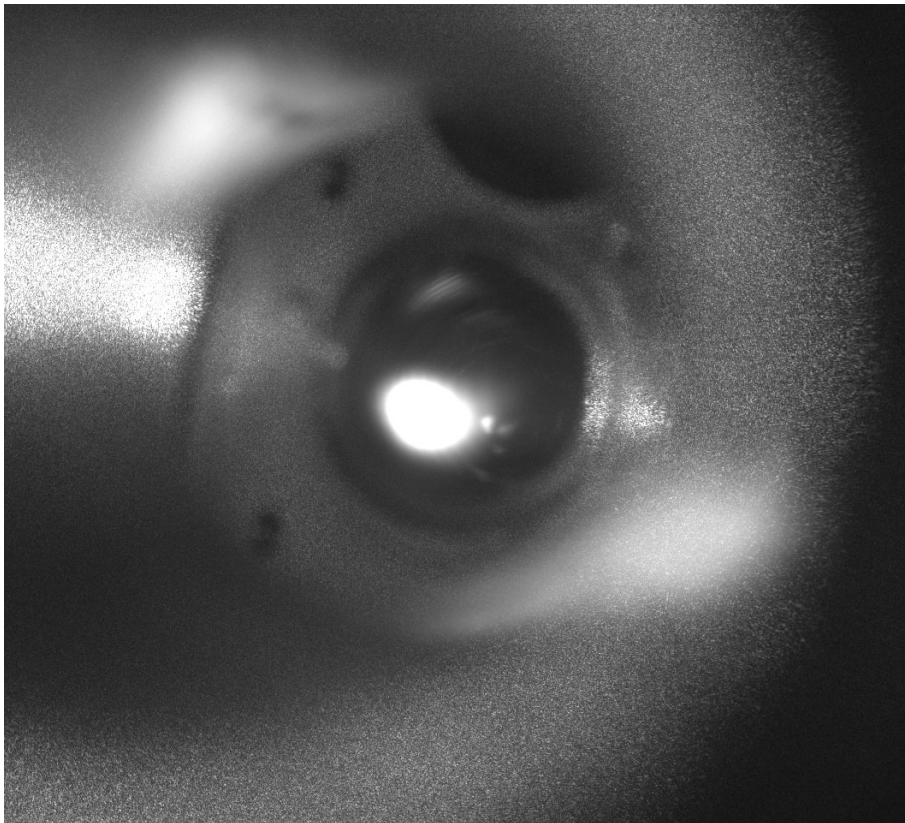


**Figure 3.9:** Image of MOT for atoms in  $^{85}\text{Rb } F_g = 3$  hyperfine ground state.

Laser cooling and trapping are done for atoms in both upper  $^{85}\text{Rb } F_g = 3$  and lower  $^{85}\text{Rb } F_g = 2$  hyperfine ground state of D2 transition line. In the first case of type-I MOT, trap laser is red detuned by 13 MHz and the TMTS reference signal is used to lock the laser at  $^{85}\text{Rb } F_g = 3 \rightarrow F_e = 4$ . The repumper laser is locked by SAS at  $^{85}\text{Rb } F_g = 2 \rightarrow F_e = 3$ . Fig. 3.9 shows the MOT for the atom in the upper hyperfine ground state in a UHVC with the background pressure of  $\sim 5.3 \times 10^{-8}$  torr and current of  $\sim 3$  A passing through Rb-getter to produce Rb vapors in the chamber. Total power of three orthogonal pairs of trap beams and repumper beams is 65.3 mW with beam diameter 2 cm. Two anti-Helmholtz coils, with

current of 3.2 A passing through upper coil and 3.4 A passing through lower coil, are used to generate magnetic field gradient to confine atoms at the center. The width and height of atomic cloud are 0.78 cm and 0.72 cm, respectively, which is full width at half maximum (FWHM) calculated by Gaussian fitting the pixel data of image from CCD camera, as shown in Fig. 3.6. No. of Rb atoms trapped in MOT are measured to be  $4.8 \times 10^6$  with corresponding density of  $7.6 \times 10^5 \text{ cm}^{-3}$ . The shape of MOT with  $F_g < F_e$  cyclic transition forms a spherical shape with no chances of forming a ring shaped cloud with above mentioned parameters and alignment of the laser beams.

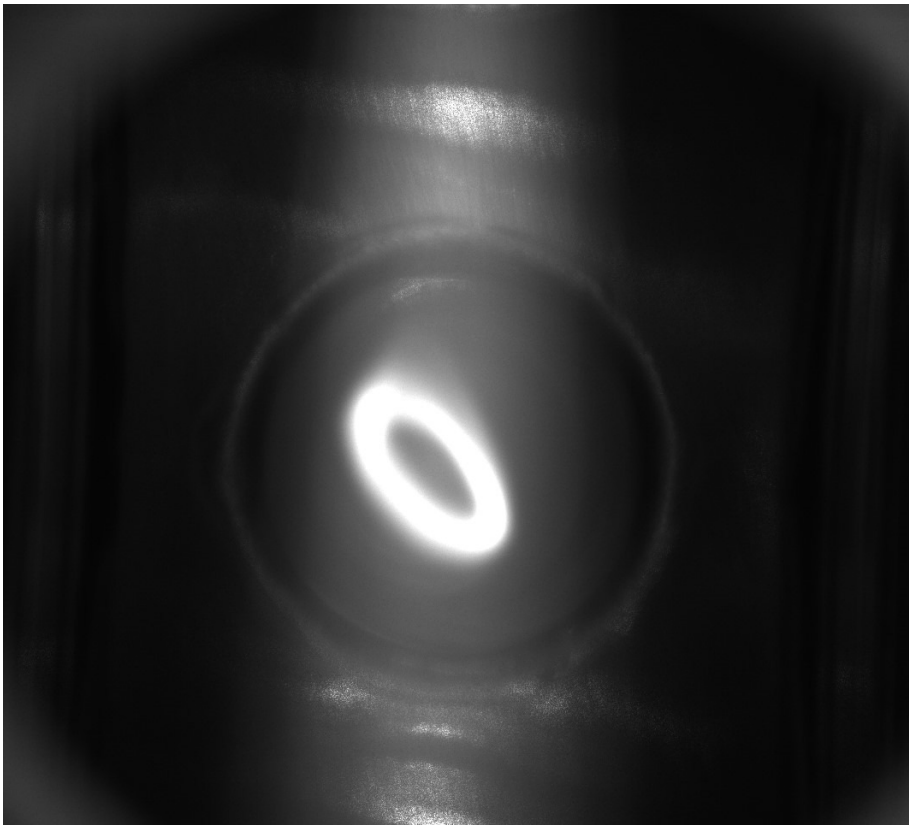


**Figure 3.10:** Image of MOT for atoms in  $^{85}\text{Rb } F_g = 2$  hyperfine ground state.

In the second case of type-II MOT, where  $F_g > F_e$ , trap laser is red detuned by 10 MHz and the TMTS reference signal is used to lock the laser at  $^{85}\text{Rb } F_g =$

$2 \rightarrow F_e = 1$  transition. The repumper laser is locked at  $^{85}\text{Rb } F_g = 3 \rightarrow F_e = 3$  by SAS. Fig. 3.10 shows the MOT for the atom in the lower hyperfine ground state with same trap parameters as for the first case. Only difference is the coils current of 3.3 A passing through upper coil and 3 A passing through the lower coil, are used to generate magnetic field gradient to confine atoms at the center. Instead of forming a spherical cloud of atom, a ring shaped MOT shows up. It is possible to get the ring shaped MOT by misaligning the laser beams [93, 94]. We tried to change the alignment of the laser beams but the center always stays hollow. Laser cooling and trapping for atoms in lower hyperfine ground state have been reported before [32] but they used the technique to stabilize the laser frequency that uses external magnetic field [95]. As the Zeeman sublevels of ground and excited states are not coupled well in case of  $F_g > F_e$ , the uncoupled excited state act as dark states and trapping force becomes weak. Zeeman splitting of cooling transitions, polarization of the laser beams and mixing of closely spaced hyperfine energy levels play a significant role in trapping force in type-II cooling transitions. It becomes more complex as atom cannot scatter photons continuously without being optically pumped to a dark state and still not understood fully.

### 3.4 Summary

The ability of MTS to produce distinct line with negligible background with zero crossing accurately centered at the resonance frequency of the cyclic transition is utilized alongside AOM to generate TMTS. In two cases, a red detuned and a blue detuned TMTS signal by 200 MHz are generated for  $^{85}\text{Rb } F_g = 3 \rightarrow F_e = 4$  and  $^{87}\text{Rb } F_g = 2 \rightarrow F_e = 3$  D2 cyclic transition lines. It offers Independence of peak to peak amplitude and signal gradient from tuning of laser beam.

The requirement of laser beam to be detuned below the resonance frequency for MOT is achieved by TMTS for type-I ( $F_g < F_e$ ) and type-II ( $F_g > F_e$ ). For type-I MOT, trap laser is locked at  $F_g = 3 \rightarrow F_e = 4$  D2 transition line of  $^{85}\text{Rb}$  atoms. Three orthogonal pairs of trap beams are red detuned by 13 MHz. The repumper laser's frequency is stabilized using SAS at  $F_g = 2 \rightarrow F_e = 3$  transition

of  $^{85}\text{Rb}$  atoms.  $4.8 \times 10^6$  no of Rb atoms are trapped with corresponding density of  $7.6 \times 10^5 \text{ cm}^{-3}$  of atomic mixture. On the other hand, trap beams for type-II MOT are locked at  $F_g = 2 \rightarrow F_e = 1$  D2 transition line of  $^{85}\text{Rb}$  atoms using TMTS. The repumper is locked at  $F_g = 3 \rightarrow F_e = 3$  transition with SAS. The atomic cloud forms a ring shape for Type-II MOT and exhibit greater complexity due to the inability of atoms to scatter photons in a continuous manner without undergoing optical pumping to a dark state. The complete understanding of this phenomenon is still lacking. Zeeman splitting, polarization of the laser beams, alignment of laser beam and mixing of closely spaced hyperfine energy levels play a significant role in trapping force in type-II cooling transitions.

## Chapter 4

# EIA and EIT with Varying Linear Polarization

## 4.1 Overview

In this chapter, the measurement and calculation of critical angle  $\theta_R$  between the polarization axes of the coupling and probe have been conducted, specifically in cases where Electromagnetically Induced Transparency (EIT) observes an increase in amplitude or can be transformed into Electromagnetically Induced Absorption (EIA). Both coupling and probe laser beams have linear polarization. The investigations focus on the D2 line of the  $^{85}\text{Rb}$  and  $^{87}\text{Rb}$  atoms. This involves the observation of two distinct ground state hyperfine lines, specifically  $F_g = 2$  and  $F_g = 3$ , in the case of  $^{85}\text{Rb}$  atoms, and  $F_g = 1$  and  $F_g = 2$ , in the case of  $^{87}\text{Rb}$  atoms, respectively.

The initial polarization of both the coupling and probe beams is linear and parallel. The angle between the polarization axes of the coupling and probe is varied by changing the angle of the coupling beam in 10-degree increments up to 90 degrees, and a spectral profile is recorded for each  $\theta_R$ . Closed transitions,  $F_g = 3 \rightarrow F_e = 4$  of  $^{85}\text{Rb}$  and  $F_g = 2 \rightarrow F_e = 3$  of  $^{87}\text{Rb}$ , have EITs at 0 degrees and switch to EIAs at a higher  $\theta_R$ . Furthermore, open transitions,  $F_g = 3 \rightarrow F_e = 2$  and  $3$  of  $^{85}\text{Rb}$  and  $F_g = 2 \rightarrow F_e = 1$  and  $2$  of  $^{87}\text{Rb}$  have EITs at a smaller  $\theta_R$ , but as the angle increases, the EITs switch to EIAs, which is largely due to the influence of neighboring hyperfine transitions. Closed transition  $F_g = 3 \rightarrow F_e = 4$  of  $^{85}\text{Rb}$  ( $F_g = 2 \rightarrow F_e = 3$  of  $^{87}\text{Rb}$ ) has EIT at 0 degrees due to neighboring  $F_g = 3 \rightarrow F_e = 2$  and  $3$  ( $F_g = 2 \rightarrow F_e = 1$  and  $2$ ) open transitions of  $^{85}\text{Rb}$  ( $^{87}\text{Rb}$ ). Likewise, open transitions  $F_g = 3 \rightarrow F_e = 2$  and  $3$  of  $^{85}\text{Rb}$  ( $F_g = 2 \rightarrow F_e = 1$  and  $2$  of  $^{87}\text{Rb}$ ) have EIAs at a larger  $\theta_R$  due to the strong EIA of the neighboring closed transition  $F_g = 3 \rightarrow F_e = 4$  ( $F_g = 2 \rightarrow F_e = 3$ ). This has been confirmed by the calculation of the absorption profiles for degenerate two level systems (DTLS) without neighboring transitions and degenerate multi level systems (DMLS) with

neighboring transitions.

Transitions from lower ground hyperfine energy levels of  $^{85}\text{Rb}$  and  $^{87}\text{Rb}$  are open systems. Consequentially, the spectral profiles of  $F_g = 2 \rightarrow F_e = 1, 2,$  and  $3$  transitions of  $^{85}\text{Rb}$  and  $F_g = 1 \rightarrow F_e = 0, 1,$  and  $2$  transitions of  $^{87}\text{Rb}$  exhibit EITs. By comparing the experimental spectra with DTLS and DMLS absorption profiles, it is evident that the influence of neighboring transitions on each transition causes the amplitude of EITs to increase for transitions from lower ground hyperfine energy levels.

This chapter is organized as follows: Section 4.2 presents theoretical background. Section 4.3 showcases the experimental procedures used. Section 4.4 presents the measured and calculated results, while the last Section 4.5 presents some concluding remarks.

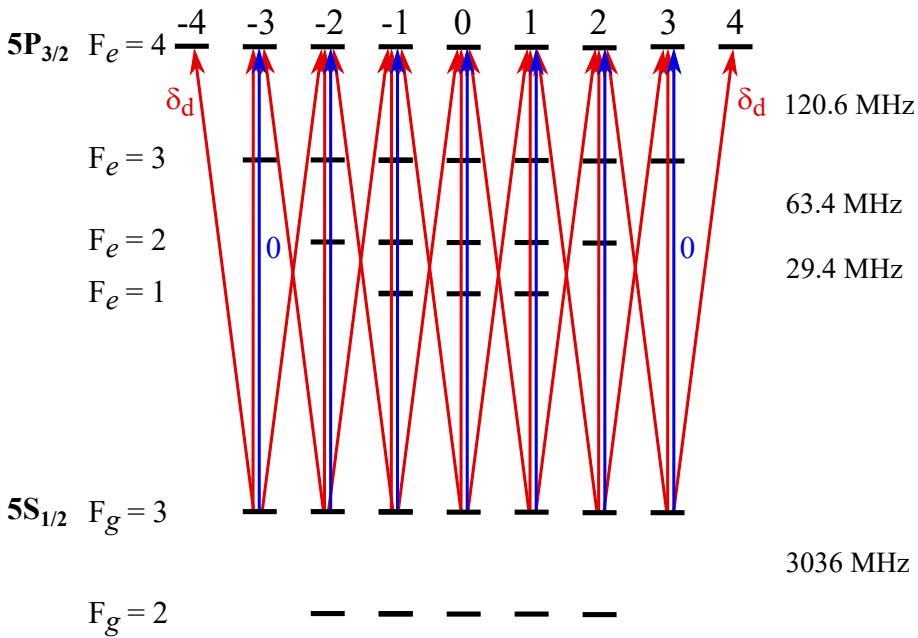


**Figure 4.1:** Energy level diagram for the  $F_g = 3 \rightarrow F_e = 4$  transitions of  $^{85}\text{Rb}$  D2 line. The blue and red lines imply the transitions excited by coupling and probe beams, respectively.

## 4.2 Theoretical Background

We solved the following density matrix equation for the  $F_g = 3 \rightarrow F_e = 2, 3$ , and 4 transitions of the  $^{85}\text{Rb}$  D2 line:

$$\dot{\rho} = - (i/\hbar) [H_0 + V, \rho] + \dot{\rho}_{\text{relax}}, \quad (4.2.1)$$

where  $\rho$  is the density operator, and  $H_0$  and  $V$  are the atomic and interaction Hamiltonians, respectively. The energy level diagram under consideration is shown in Fig. 4.1. The atomic Hamiltonian in Eq. (4.2.1) is given by

$$H_0 = - \sum_{j=2}^4 \sum_{m=-j}^j \hbar (\delta_c + \Delta_{4j}) |F_e = j, m\rangle \langle F_e = j, m|, \quad (4.2.2)$$

where  $\delta_c (= d_c - kv)$  is the effective detuning of the coupling beam,  $d_c$  is the detuning of the coupling beam,  $k$  is the wave vector, and  $v$  is the velocity of an atom. For later purpose,  $\delta_p (= d_p - kv)$  is defined for the probe beam similarly. In Eq. (4.2.2),  $\Delta_{4j}$  is the frequency spacing between the states  $|F_e = 4\rangle$  and  $|F_e = j\rangle$ . The interaction Hamiltonian in Eq. (4.2.1) is given by

$$\begin{aligned}
 V = & \frac{\hbar}{2} \Omega_p e^{-i\delta_d t} \sum_{q=-1}^1 \sum_{F_e=2}^4 \sum_{m=-3}^3 a_q C_{3,m}^{F_e, m+q} |F_e, m+q\rangle \langle F_g, m| \\
 & + \frac{\hbar}{2} \Omega_c \sum_{F_e=2}^4 \sum_{m=-3}^3 C_{3,m}^{F_e, m} |F_e, m\rangle \langle F_g, m| + \text{h.c.}, \quad (4.2.3)
 \end{aligned}$$

where  $\delta_d = d_p - d_c$  and  $\Omega_p$  ( $\Omega_c$ ) is the Rabi frequency of the probe (coupling) beam. In Eq. (4.2.3), h.c. represents the hermitian conjugate and  $C_{F_g, m_g}^{F_e, m_e}$  is the normalized transition strength between the states  $|F_e, m_e\rangle$  and  $|F_g, m_g\rangle$  [96]. In Eq. (4.2.1),  $\dot{\rho}_{\text{relax}}$  denotes the term associated with relaxation phenomena [97].

Because the quantization axis is chosen as the direction of the electric field of the coupling beam, the coupling beam excites the transitions with  $\Delta m = 0$  as formulated in Eq. (4.2.3). Then, the probe beam excites the transitions with

$\Delta m = 0$  and  $\pm 1$ , and the coefficients in Eq. (4.2.3) for the probe beam are given by

$$a_{\pm 1} = \mp 2^{-1/2} \sin \theta, \quad a_0 = \cos \theta. \quad (4.2.4)$$

The transitions by the coupling and probe beams are represented by the blue and red arrows in Fig. 4.1, respectively. In Fig. 4.1, “0” and “ $\delta_d$ ” denote the effective detuning of the coupling and probe beams with respect to the detuning of the coupling beam, respectively.

The mixing of laser frequencies via atoms leads to creation of many oscillation frequencies for the density matrix elements. Then, the interaction of photons up to the third order, the matrix elements for the optical coherences are decomposed explicitly as follows:

$$\begin{aligned} \rho_{e_{m+q}, g_m}^j &= \rho_{e_{m+q}, g_m}^{j(1)} e^{-i\delta_d t} + \rho_{e_{m+q}, g_m}^{j(2)} \\ &\quad + \rho_{e_{m+q}, g_m}^{j(3)} e^{i\delta_d t} + \rho_{e_{m+q}, g_m}^{j(4)} e^{-2i\delta_d t}, \end{aligned} \quad (4.2.5)$$

$$\begin{aligned} \rho_{e_{m\pm 2}, g_m}^j &= \rho_{e_{m\pm 2}, g_m}^{j(1)} + \rho_{e_{m\pm 2}, g_m}^{j(2)} e^{-i\delta_d t} \\ &\quad + \rho_{e_{m\pm 2}, g_m}^{j(3)} e^{-2i\delta_d t}, \end{aligned} \quad (4.2.6)$$

$$\rho_{e_{m\pm 3}, g_m}^j = \rho_{e_{m\pm 2}, g_m}^{j(1)} e^{-i\delta_d t}, \quad (4.2.7)$$

where  $q = 0, \pm 1$  in Eq. (4.2.5) and  $\rho_{e_{m'}, g_m}^j \equiv \langle F_e = j, m' | \rho | F_g = 3, m \rangle$ . The decomposition of Zeeman coherence are given by

$$\rho_{e_m^j, e_{m+q}^j} = \rho_{e_m^j, e_{m+q}^j}^{(1)} + \rho_{e_m^j, e_{m+q}^j}^{(2)} e^{-i\delta_d t} + \rho_{e_m^j, e_{m+q}^j}^{(3)} e^{i\delta_d t}, \quad (4.2.8)$$

$$\rho_{e_m^j, e_{m+2}^j} = \rho_{e_m^j, e_{m+2}^j}^{(1)}, \quad (4.2.9)$$

where  $q = 0, 1$  in Eq. (4.2.8), and  $\rho_{e_{m'}, e_m^j}^j \equiv \langle F_e = j, m' | \rho | F_e = j, m \rangle$ . The Zeeman coherences for the ground state are decomposed similarly as those presented in Eqs. (4.2.8) and (4.2.9). The populations, diagonal matrix elements of the density



operator, are decomposed as follows:

$$\rho_{\mu_m^j, \mu_m^j} = \rho_{\mu_m^j, \mu_m^j}^{(1)} + \rho_{\mu_m^j, \mu_m^j}^{(2)} e^{-i\delta_d t} + \rho_{\mu_m^j, \mu_m^j}^{(2)*} e^{i\delta_d t}, \quad (4.2.10)$$

where  $\mu = e$  or  $g$  and  $\rho_{\mu_m^j, \mu_m^j}^{(1)}$  is real.

Inserting the Hamiltonians and decomposed density matrix elements into Eq. (4.2.1), a series of coupled time-dependent differential equations is obtained, which is then solved in a steady-state regime to find the density matrix elements as a function of detunings and velocity. After averaging over the Maxwell-Boltzmann velocity distribution, we obtain the absorption coefficient for the probe beam as follows:

$$\alpha = -\frac{3\lambda^2 N_{\text{at}}}{2\pi \Omega_p} \int_{-\infty}^{\infty} \frac{dv}{\sqrt{\pi} v_{\text{mp}}} e^{-(v/v_{\text{mp}})^2} \times \text{Im} \left[ \sum_{j=2}^4 \sum_{q=-1}^1 \sum_{m=-3}^3 a_q^* C_{3,m}^{Fe, m+q} \rho_{e_{m+q}, g_m}^{(1)} \right], \quad (4.2.11)$$

where  $\lambda$  is the wavelength of lasers,  $v_{\text{mp}}$  is the most probable speed of atoms, and in the cell, and  $N_{\text{at}}$  is the atomic density in the cell.

### 4.3 Experimental Setup

A laser beam of wavelength 780 nm from a single tunable external cavity diode laser (DLpro, Toptica Inc.) passes through an optical window, reflecting a small portion of it for saturation absorption spectroscopy (SAS), while the rest goes to a polarizing beam splitter (PBS-1), as shown in Fig. 4.2. A half-wave plate (HWP) is placed before PBS-1 to divide the beam into coupling and probe beams and maintain the beam power ratio between the two resulting beams. The probe beam is magnified by a factor of five to 4 mm in diameter with the beam expander (GBE05-B, Thorlabs) and is aimed at the vapor cell after passing through the beam splitter (BS). A HWP before BS maintains the polarization of the probe beam. The vapor cell has dimensions of 5 cm in length and 2.5 cm in diameter.

The vapor cell is protected from the effects of stray magnetic fields and the earth's magnetic field by five layers of  $\mu$ -metal sheet. The coupling beam is scanned by passing through two acousto-optic modulators (AOM). The first AOM-1 (3080-122, Gooch & Housego) is fixed at 80 MHz using the AOM driver (1080AF-AINA-1.0 HCR, Gooch & Housego), and the other AOM-2 (3080-122, Crystal Technology, Inc.) is scanned by  $\pm 1$  MHz at -80 MHz using the deflector driver (DE-802EM26, IntraAction). To match the polarization of the probe beam (P-polarized), another set of HWP and PBS is used for the coupling beam. A beam expander (GBE05-B, Thorlabs) also expands the coupling beam to 4 mm in diameter. Both probe and coupling beams meet at BS, and HWP is placed on the coupling beam before it falls onto BS to specify  $\theta_R$ . For 10 different settings of HWPs placed before the BS, spectral profiles are recorded for 6 transitions ( $F_g = 2 \rightarrow F_e = 1, 2, 3$  and  $F_g = 3 \rightarrow F_e = 2, 3, 4$ ) of  $^{85}\text{Rb}$  and 6 transitions ( $F_g = 1 \rightarrow F_e = 0, 1, 2$  and  $F_g = 2 \rightarrow F_e = 1, 2, 3$ ) of  $^{87}\text{Rb}$  for the D2 line of Rb atoms.

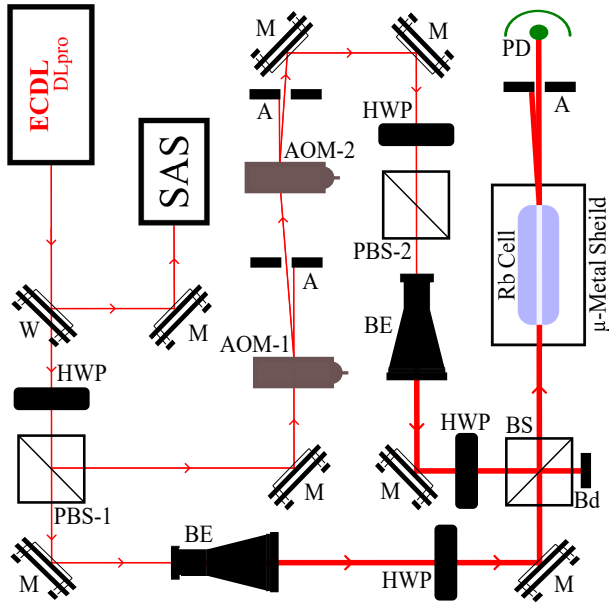


**Figure 4.2:** Schematic diagram of experimental setup. Component symbols: SAS: saturation absorption spectroscopy; W: window; HWP: halfwave plate; PBS: polarizing beam splitter; BE: beam expander; A: aperture; AOM: acousto-optic modulator; M: mirror; BS: beam splitter; Bd: beam dump; PD: photodetector.

The SAS setup is similar to that described in Chap. 1 and includes a vapor cell that measures 10cm in length and 2.5cm in diameter. The photodetector (PDA36A-EC, Thorlabs) detects the probe beam of the SAS setup and feeds the output to the Diode Laser Controller (DLC pro, Toptica Inc.) for laser frequency stabilization.

At first, both the coupling and probe beams are P-polarized and  $\theta_R$  between them is 0 degrees. The co-propagating beams pass through the vapor cell, and only the probe beam is detected at the photodetector (PDA36A-EC, Thorlabs). An intersection angle of 0.1mRad is maintained between the probe and coupling beams. The experiment is performed at room temperature. The polarization of the probe beam stays P-polarized while the HWP rotates the polarization of the coupling beam by 10 degrees for the second spectral profile. Similarly, spectral profiles are recorded at 20, 30, 40, 50, 60, 70, 80, and 90 degree  $\theta_R$  between the probe and coupling beams.

## 4.4 Results and Discussion

In cases where EIT can be changed to EIA and vice versa for coupling and probe laser beams with linear polarization, the critical  $\theta_R$  for switching from EIT to EIA have been calculated and measured for transitions from  $F_g = 2$ , and 3 of  $^{85}\text{Rb}$  and  $F_g = 1$ , and 2 of  $^{87}\text{Rb}$ , D2 line of Rb atoms. The four cases are:

- $F_g = 2 \rightarrow F_e = 1, 2, \text{ and } 3$  transitions of  $^{85}\text{Rb}$
- $F_g = 3 \rightarrow F_e = 2, 3, \text{ and } 4$  transitions of  $^{85}\text{Rb}$
- $F_g = 1 \rightarrow F_e = 0, 1, \text{ and } 2$  transitions of  $^{87}\text{Rb}$
- $F_g = 2 \rightarrow F_e = 1, 2, \text{ and } 3$  transitions of  $^{87}\text{Rb}$

With increasing  $\theta_R$ , the spectral profiles change from EIT to EIA for atoms with higher hyperfine energy levels ( $^{85}\text{Rb } F_g = 3$  and  $^{87}\text{Rb } F_g = 2$ ) and stay the same for atoms with lower hyperfine energy levels ( $^{85}\text{Rb } F_g = 2$  and  $^{87}\text{Rb } F_g = 1$ ).

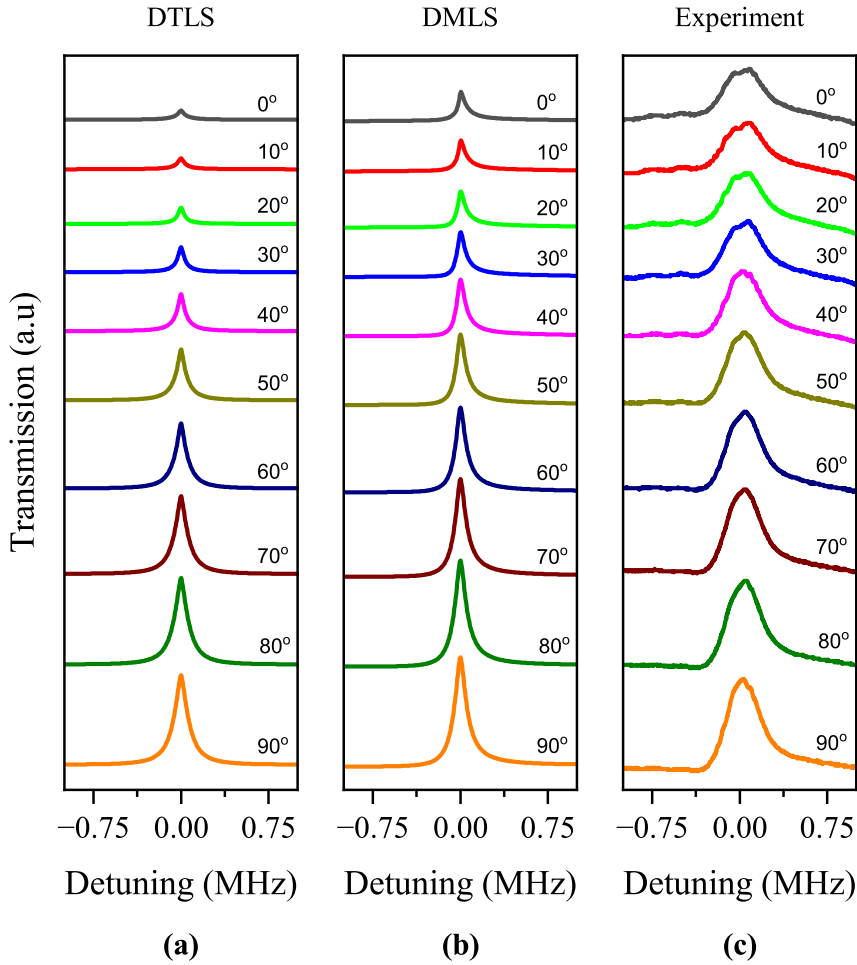


**Figure 4.3:** Comparison of calculated and measured spectra for  $F_g = 2 \rightarrow F_e = 1$  transition considering (a) pure two-level resonant transition (b) a transition resonant at  $F_g = 2 \rightarrow F_e = 1$  with neighboring hyperfine transitions  $F_g = 2 \rightarrow F_e = 2$  and  $F_g = 2 \rightarrow F_e = 3$  (c) experimentally measured spectra for resonant transition  $F_g = 2 \rightarrow F_e = 1$ .

#### 4.4.1 $F_g = 2 \rightarrow F_e = 1, 2, \text{ and } 3$ transitions of $^{85}\text{Rb}$

The spectral profiles of transitions from the lower hyperfine energy level  $F_g = 2$  of the D2 line of  $^{85}\text{Rb}$  are shown as EITs in Figs. 4.3 (c), 4.4 (c), and 4.5 (c) for all  $\theta_R$  from 0 degrees ( $\pi \parallel \pi$ ) to 90 degrees ( $\pi \perp \pi$ ). The experimental spectra

match up well with the DMLS absorption profiles shown in Figs. 4.3 (b), 4.4 (b), and 4.5 (b). However, the DTLS absorption profiles shown in Figs. 4.3 (a), 4.4 (a), and 4.5 (a) have lower EIT amplitudes at all rotational angles of polarization. This demonstrates unequivocally that the neighboring transitions influence the spectral features of each transition.

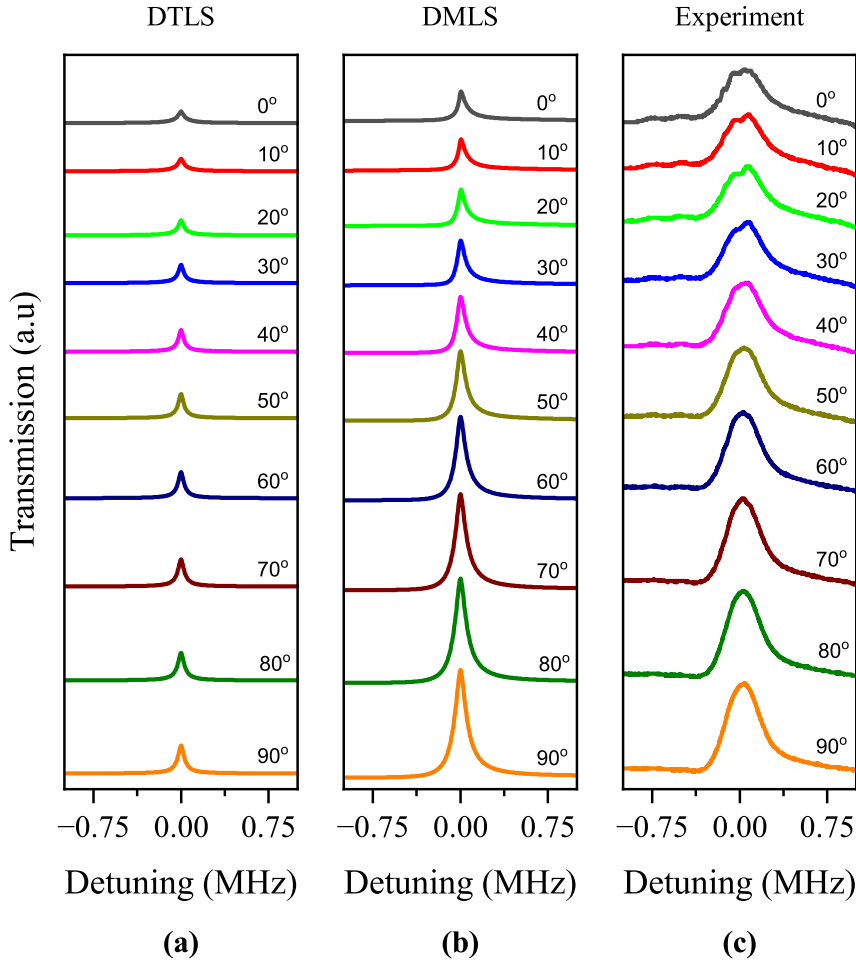


**Figure 4.4:** Comparison of calculated and measured spectra for  $F_g = 2 \rightarrow F_e = 2$  transition considering (a) pure two-level resonant transition (b) a transition resonant at  $F_g = 2 \rightarrow F_e = 2$  with neighboring hyperfine transitions  $F_g = 2 \rightarrow F_e = 3$  and  $F_g = 2 \rightarrow F_e = 1$  (c) experimentally measured spectra for resonant transition  $F_g = 2 \rightarrow F_e = 2$ .

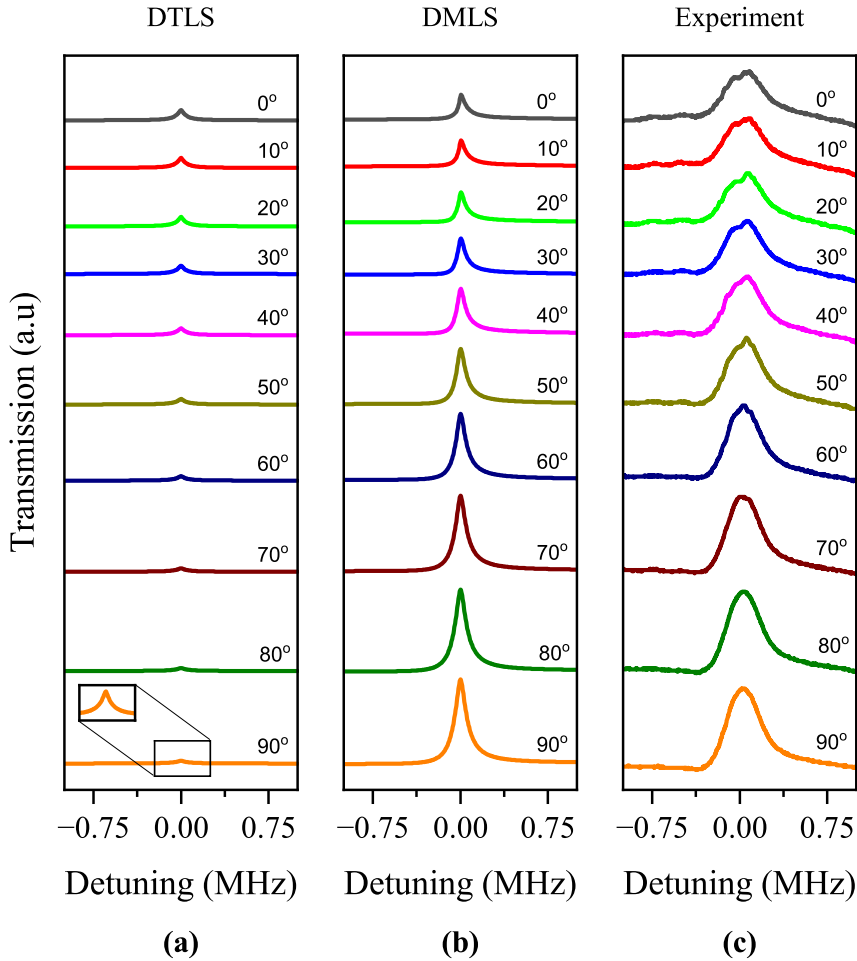


**Figure 4.5:** Comparison of calculated and measured spectra for  $F_g = 2 \rightarrow F_e = 3$  transition considering (a) pure two-level resonant transition (b) a transition resonant at  $F_g = 2 \rightarrow F_e = 3$  with neighboring hyperfine transitions  $F_g = 2 \rightarrow F_e = 1$  and  $F_g = 2 \rightarrow F_e = 2$  (c) experimentally measured spectra for resonant transition  $F_g = 2 \rightarrow F_e = 3$ .

As shown in Fig. 4.3, the amplitude of EIT at 0 degree goes up as  $\theta_R$  increases for  $F_g = 2 \rightarrow F_e = 1$ . This is true for experimental spectra, DMLS, and DTLS calculation results. The amplitude at each respective  $\theta_R$  for DMLS is larger than that of DTLS, which is due to the contribution from the neighboring  $F_g = 2 \rightarrow F_e = 2$  and  $F_g = 2 \rightarrow F_e = 3$  transitions. The influence of neighboring transitions is

more clear in comparison of the DTLS and DMLS calculations of  $F_g = 2 \rightarrow F_e = 2$  and  $F_g = 2 \rightarrow F_e = 3$  transitions.

The DTLS EITs of the  $F_g = 2 \rightarrow F_e = 2$  transition at all  $\theta_R$  are quite small in comparison to the DMLS. Higher amplitudes of DMLS are due to the neighboring  $F_g = 2 \rightarrow F_e = 1$  and  $F_g = 2 \rightarrow F_e = 3$  transitions. Like the  $F_g = 2 \rightarrow F_e = 1$  transition, the  $F_g = 2 \rightarrow F_e = 2$  transition has an increase in amplitude as  $\theta_R$  goes up. This is shown in Fig. 4.4 for experimental spectra, DMLS, and DTLS calculations, and it is also true for the  $F_g = 2 \rightarrow F_e = 2$  transition. In contrast to the  $F_g = 2 \rightarrow F_e = 1$  and  $F_g = 2 \rightarrow F_e = 2$  transitions, the DTLS of  $F_g = 2 \rightarrow F_e = 3$  sees a decrease in amplitude with increasing  $\theta_R$ . On the other hand, experimental spectra and DMLS absorption profiles increase in amplitude as the  $\theta_R$  goes up from 0 to 90 degrees, as shown in Fig. 4.5. Even though the amplitudes of DTLS decrease as the  $\theta_R$  goes up, the amplitudes of the DMLS spectral profiles and experimental spectra increase as the  $\theta_R$  goes up. This is because the EITs of neighboring  $F_g = 2 \rightarrow F_e = 2$  and  $F_g = 2 \rightarrow F_e = 1$  transitions make the amplitude of this transition go up.

#### 4.4.2 $F_g = 3 \rightarrow F_e = 2, 3,$ and $4$ transitions of $^{85}\text{Rb}$

Transitions from the upper ground hyperfine energy level of the D2 line of  $^{85}\text{Rb}$  switch from EIT to EIA with an increase in the  $\theta_R$ . The  $F_g = 3 \rightarrow F_e = 4$  transition is a closed system, whereas  $F_g = 3 \rightarrow F_e = 2$  and  $F_g = 3 \rightarrow F_e = 3$  are open systems. This is why the DTLS of  $F_g = 3 \rightarrow F_e = 4$  shown in Fig. 4.6 (a) are EIAs and the DTLS of  $F_g = 3 \rightarrow F_e = 3$  shown in 4.7 (a) and  $F_g = 3 \rightarrow F_e = 2$  shown in 4.8 (a) are EITs. Figs. 4.6 (b)-(c), 4.7 (b)-(c), and 4.8 (b)-(c) show that DMLS absorption profiles and experimental spectra are EITs at small  $\theta_R$  and EIAs at larger angles.

The closed  $F_g = 3 \rightarrow F_e = 4$  transition has EIT at 0 degrees ( $\pi \parallel \pi$ ) due to the neighboring open  $F_g = 3 \rightarrow F_e = 3$  and  $F_g = 3 \rightarrow F_e = 2$  transitions. With an increase in the  $\theta_R$ , EIT switches to EIA at 10 degrees, as shown in Figure 4.6 (b)-(c). Further increasing the rotational angle increases the amplitude of EIA, and the maximum amplitude of EIA is recorded at 90 degrees ( $\pi \perp \pi$ ). Although EIT

at 0 degrees is relatively small, it only appears when coupling and probe beams have linear parallel polarizations.

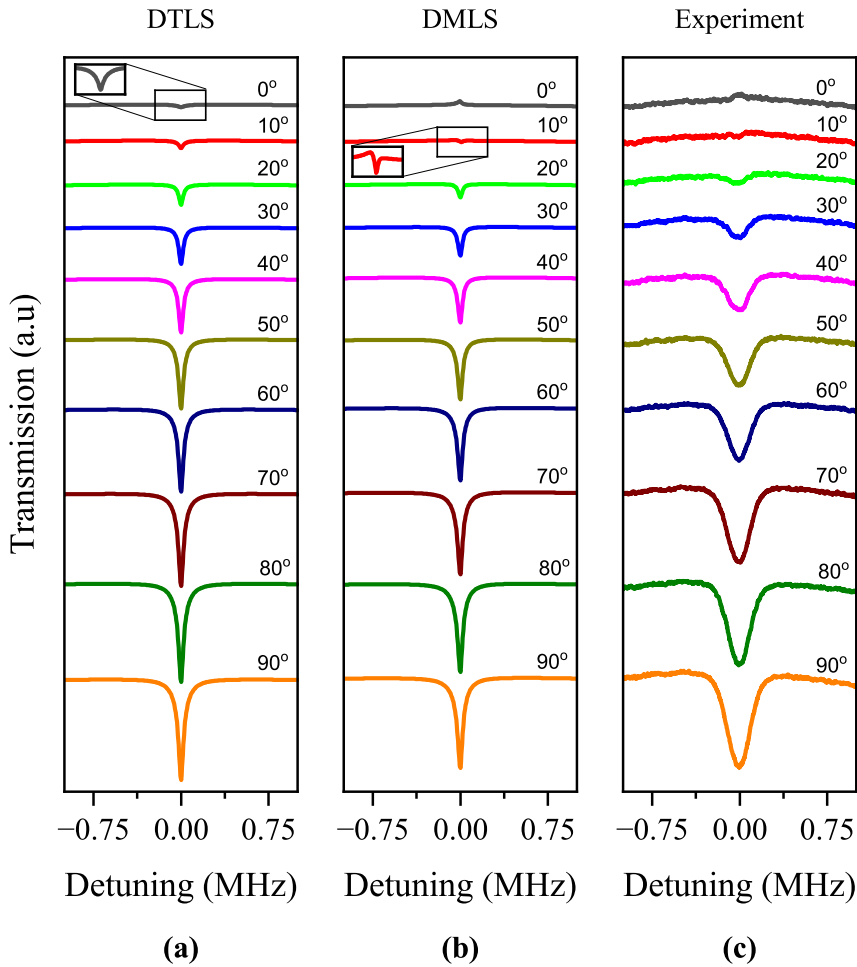


**Figure 4.6:** Comparison of calculated and measured spectra for  $F_g = 3 \rightarrow F_e = 4$  transition considering (a) pure two-level resonant transition (b) a transition resonant at  $F_g = 3 \rightarrow F_e = 4$  with neighboring hyperfine transitions  $F_g = 3 \rightarrow F_e = 3$  and  $F_g = 3 \rightarrow F_e = 2$  (c) experimentally measured spectra for resonant transition  $F_g = 3 \rightarrow F_e = 4$ .



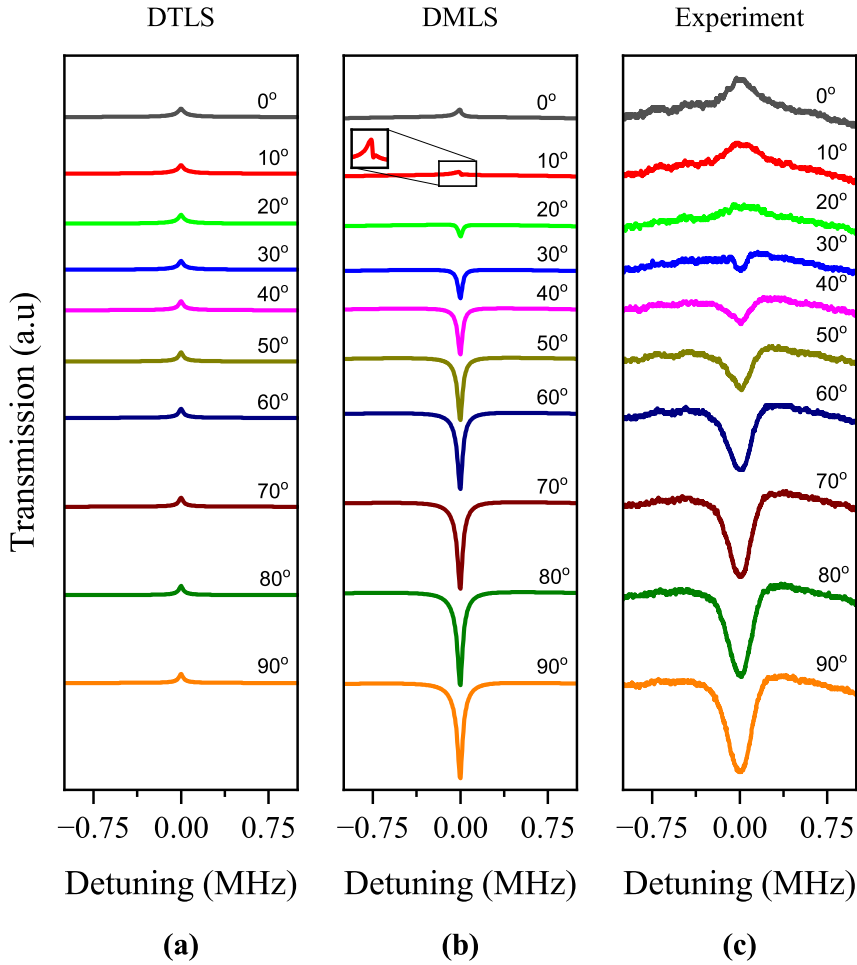


**Figure 4.7:** Comparison of calculated and measured spectra for  $F_g = 3 \rightarrow F_e = 3$  transition considering (a) pure two-level resonant transition (b) a transition resonant at  $F_g = 3 \rightarrow F_e = 3$  with neighboring hyperfine transitions  $F_g = 3 \rightarrow F_e = 2$  and  $F_g = 3 \rightarrow F_e = 4$  (c) experimentally measured spectra for resonant transition  $F_g = 3 \rightarrow F_e = 3$ .

If we do not think about the neighboring effect, the DTLS absorption profile shown in Fig. 4.6 (a) is EIA at 0 degrees and similar to EITs of open transitions from the lower hyperfine ground state  $F_g = 2$  that get stronger as the  $\theta_R$  goes up; the EIA of  $F_g = 3 \rightarrow F_e = 4$  gets stronger as the  $\theta_R$  goes up. DMLS absorption profiles match well with the experimental spectra, as shown in Fig. 4.6.

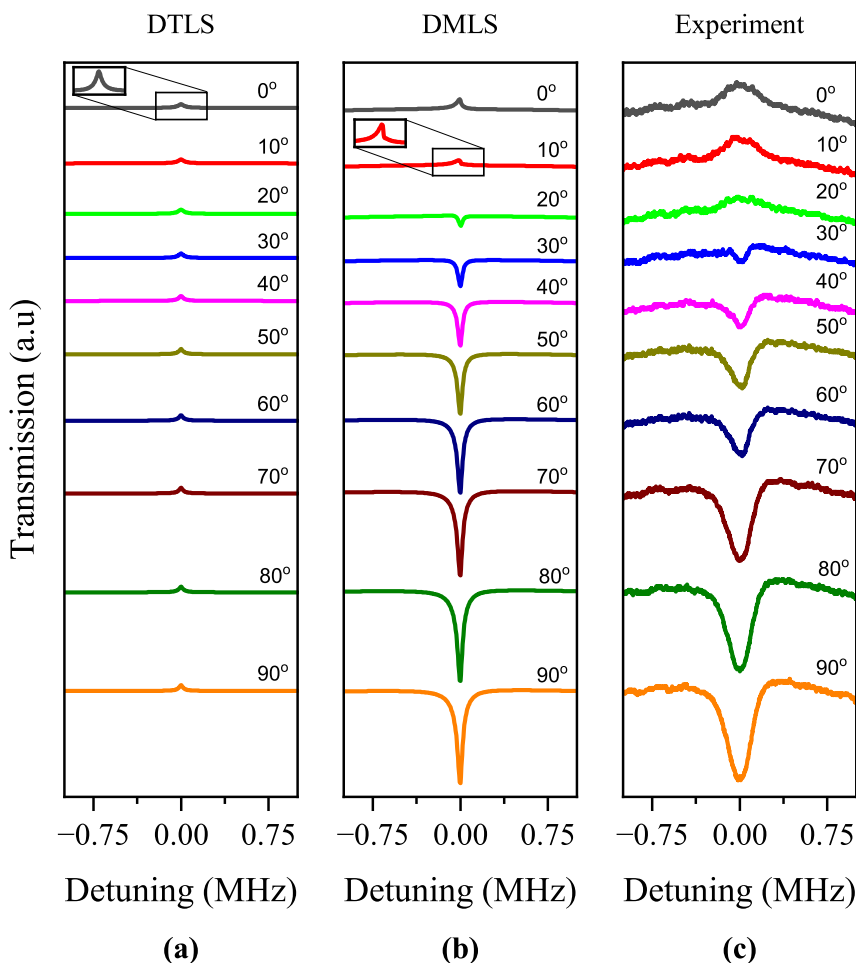


**Figure 4.8:** Comparison of calculated and measured spectra for  $F_g = 3 \rightarrow F_e = 2$  transition considering (a) pure two-level resonant transition (b) a transition resonant at  $F_g = 3 \rightarrow F_e = 2$  with neighboring hyperfine transitions  $F_g = 3 \rightarrow F_e = 3$  and  $F_g = 3 \rightarrow F_e = 4$  (c) experimentally measured spectra for resonant transition  $F_g = 3 \rightarrow F_e = 2$ .

Other transitions,  $F_g = 3 \rightarrow F_e = 3$  (Fig. 4.7) and  $F_g = 3 \rightarrow F_e = 2$  (Fig. 4.8), are open systems but exhibit EIAs at higher  $\theta_R$  because of the strong EIA of  $F_g = 3 \rightarrow F_e = 4$ . EIT instead of EIA appears for DMLS and experimental spectra for  $F_g = 3 \rightarrow F_e = 4$  because of weaker EIA at 0 degrees of DTLS. Also, EIAs grow in amplitude with increasing polarization rotation angle. The  $F_g = 3 \rightarrow F_e =$

3 and  $F_g = 3 \rightarrow F_e = 2$  transitions have EITs for DTLS, but their amplitudes don't change much as the  $\theta_R$  increases. Additionally, EITs of  $F_g = 3 \rightarrow F_e = 3$  and  $F_g = 3 \rightarrow F_e = 2$  transitions are relatively weaker than EIAs of  $F_g = 3 \rightarrow F_e = 4$  in amplitude, as shown in Figs. 4.7 (a), 4.7 (a), and 4.6 (a), respectively. So, there are more chances of open transitions getting influenced by neighboring close  $F_g = 3 \rightarrow F_e = 4$  transition.

Both transitions have EITs at 0 and 10 degrees polarization rotation angles and switch to EIA with further increments, as shown in Figs. 4.7 (b)-(c) and 4.8 (b)-(c). The strongest EIT signal is recorded at 0 degrees polarization rotation angle, whereas after conversion, the EIA grows with the increase in rotational angle, and the strongest EIA is recorded at 90 degrees. Experimental results match well with the calculated absorption profiles.

#### 4.4.3 $F_g = 1 \rightarrow F_e = 0, 1, \text{ and } 2$ transitions of $^{87}\text{Rb}$

The transitions from the lower ground hyperfine energy level  $F_g = 1$  of the D2 line of  $^{87}\text{Rb}$  have EITs at all  $\theta_R$ , as can be seen in Figs. 4.9, 4.10, and 4.11. DTLS absorption profiles at each  $\theta_R$  of  $F_g = 1 \rightarrow F_e = 1$  are stronger than those of  $F_g = 1 \rightarrow F_e = 0$  and  $F_g = 1 \rightarrow F_e = 2$ , as shown in Figs. 4.10 (a), 4.9 (a), and 4.11 (a), respectively. This is different from the type II cycling  $F_g = 2 \rightarrow F_e = 1$  transition of  $^{85}\text{Rb}$  that has the strongest EIT signals and has dominating neighboring effects on other transitions from  $F_g = 2$ . As shown in Figs. 4.9 (b)-(c), 4.10 (b)-(c), and 4.11 (b)-(c), the open  $F_g = 1 \rightarrow F_e = 1$  transition has neighboring effects that dominate the  $F_g = 1 \rightarrow F_e = 0$  and  $F_g = 1 \rightarrow F_e = 2$  transitions for  $^{87}\text{Rb}$  atoms with  $F_g = 1$ .

The comparison of DTLS, DMLS, and experimental spectra for transitions from  $F_g = 1$  is shown in Figs. 4.9 – 4.11. As shown in Fig. 4.9 (a), DTLS exhibit EITs, and their amplitude increases with the increase in  $\theta_R$  for the  $F_g = 1 \rightarrow F_e = 0$  transition. Similar to DTLS, DMLS absorption profiles shown in 4.9 (b) have EITs and get stronger with an increase in  $\theta_R$ . DMLS calculations have a slightly stronger amplitude of EITs because of the neighboring effect from  $F_g = 1 \rightarrow F_e$

$= 1$  and  $F_g = 1 \rightarrow F_e = 2$  transitions.

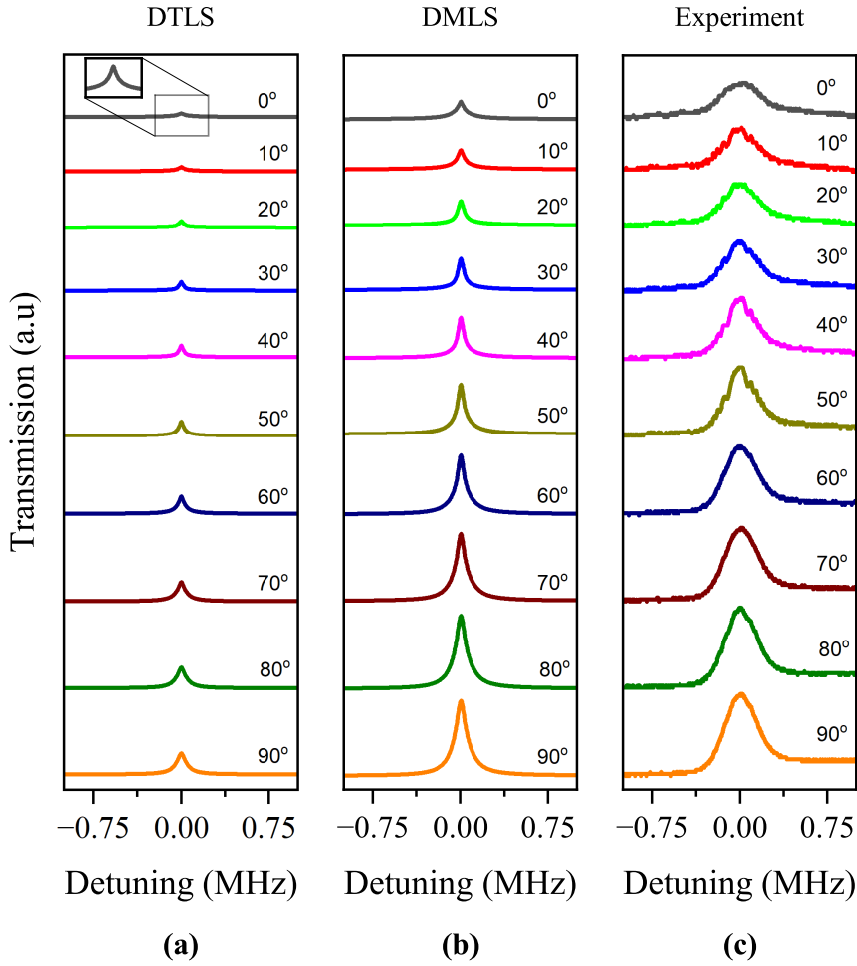


**Figure 4.9:** Comparison of calculated and measured spectra for  $F_g = 1 \rightarrow F_e = 0$  transition considering (a) pure two-level resonant transition (b) a transition resonant at  $F_g = 1 \rightarrow F_e = 0$  with neighboring hyperfine transitions  $F_g = 1 \rightarrow F_e = 1$  and  $F_g = 1 \rightarrow F_e = 2$  (c) experimentally measured spectra for resonant transition  $F_g = 1 \rightarrow F_e = 0$ .

Except for the linewidth, the experimental spectra shown in Fig. 4.9 (c) matches well with the DMLS calculation. DTLS calculations of  $F_g = 1 \rightarrow F_e = 1$  shown in 4.10 (a) follow a similar pattern, as their EITs also get stronger as the  $\theta_R$  goes up, but their amplitude at each  $\theta_R$  is stronger than that of the  $F_g = 1 \rightarrow F_e =$

0 transition. DMLS calculated absorption profiles have stronger amplitudes because of the contribution from neighboring  $F_g = 1 \rightarrow F_e = 0$  and  $F_g = 1 \rightarrow F_e = 2$  transitions, as shown in Fig. 4.10 (b). The experimental spectra in Fig. 4.10 (c) match well with DMLS profiles.

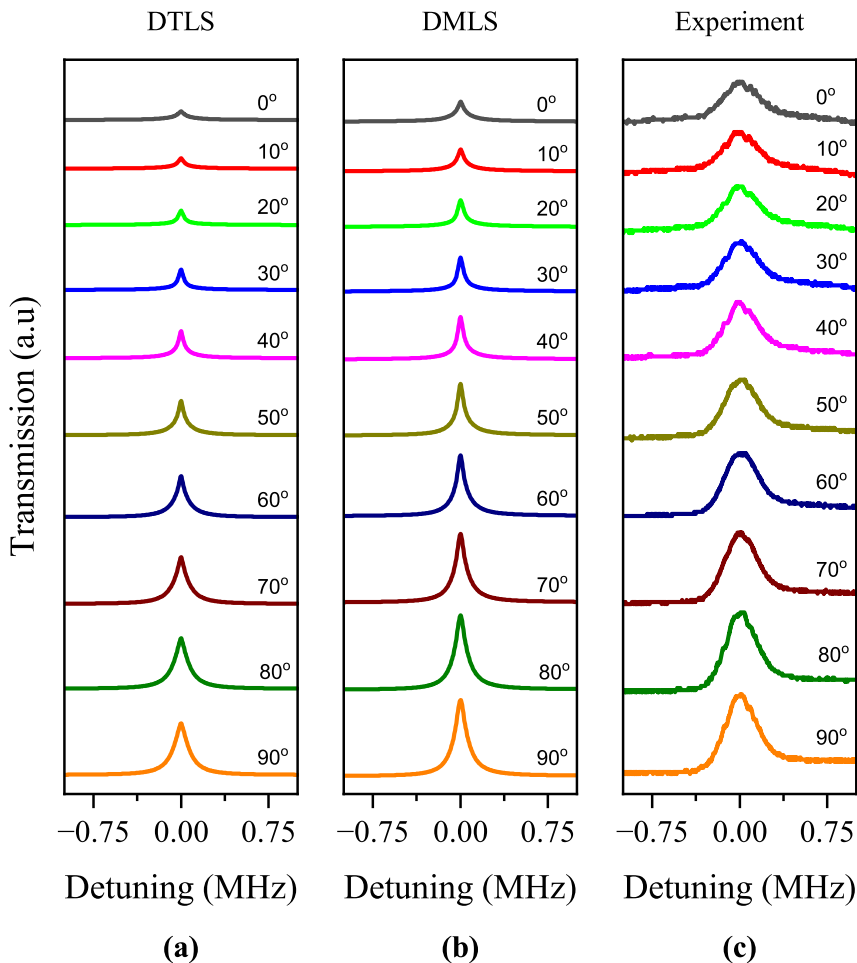


**Figure 4.10:** Comparison of calculated and measured spectra for  $F_g = 1 \rightarrow F_e = 1$  transition considering (a) pure two-level resonant transition (b) a transition resonant at  $F_g = 1 \rightarrow F_e = 1$  with neighboring hyperfine transitions  $F_g = 1 \rightarrow F_e = 0$  and  $F_g = 1 \rightarrow F_e = 2$  (c) experimentally measured spectra for resonant transition  $F_g = 1 \rightarrow F_e = 1$ .

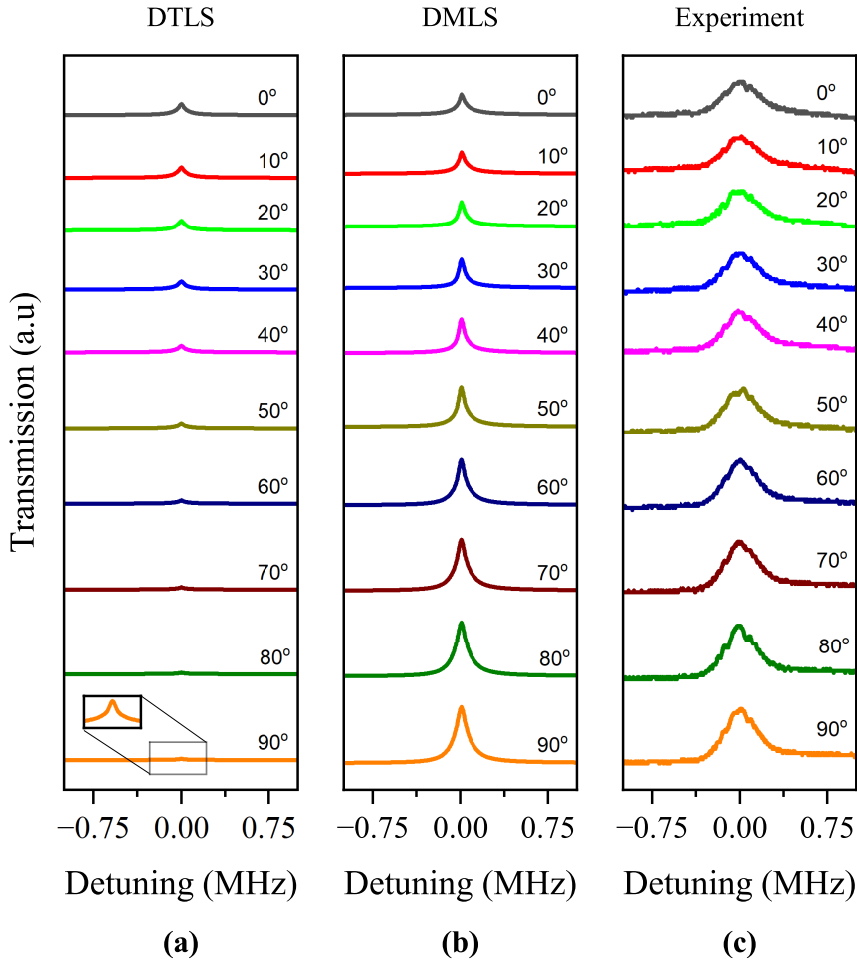


**Figure 4.11:** Comparison of calculated and measured spectra for  $F_g = 1 \rightarrow F_e = 2$  transition considering (a) pure two-level resonant transition (b) a transition resonant at  $F_g = 1 \rightarrow F_e = 2$  with neighboring hyperfine transitions  $F_g = 1 \rightarrow F_e = 0$  and  $F_g = 1 \rightarrow F_e = 1$  (c) experimentally measured spectra for resonant transition  $F_g = 1 \rightarrow F_e = 2$ .

In contrast to the DTLS of  $F_g = 1 \rightarrow F_e = 0$  and  $F_g = 1 \rightarrow F_e = 1$  transitions,  $F_g = 1 \rightarrow F_e = 0$  decreases in amplitude as  $\theta_R$  increases, as shown in Fig. 4.11 (a). This is similar to the  $F_g = 2 \rightarrow F_e = 3$  transition of  $^{85}\text{Rb}$ . Whereas the DMLS calculated absorption profiles shown in figure 4.11 (b) increase with the  $\theta_R$  and have stronger signals at each respective angle. The experimental spectra

match well with the DMLS and increase in amplitude with  $\theta_R$  because of the contribution from the neighboring transitions.

#### 4.4.4 $F_g = 2 \rightarrow F_e = 1, 2,$ and $3$ transitions of $^{87}\text{Rb}$

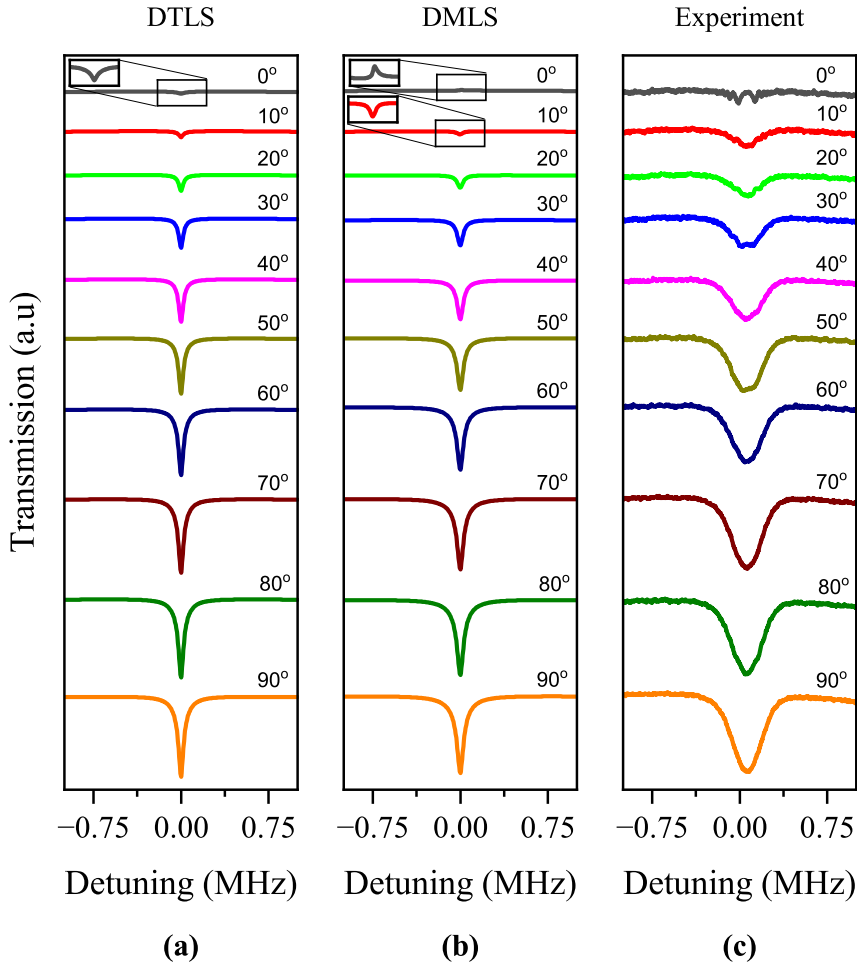


**Figure 4.12:** Comparison of calculated and measured spectra for  $F_g = 2 \rightarrow F_e = 3$  transition considering (a) pure two-level resonant transition (b) a transition resonant at  $F_g = 2 \rightarrow F_e = 3$  with neighboring hyperfine transitions  $F_g = 2 \rightarrow F_e = 1$  and  $F_g = 2 \rightarrow F_e = 2$  (c) experimentally measured spectra for resonant transition  $F_g = 2 \rightarrow F_e = 3$ .

The experimental spectra, DTLS, and DMLS calculated absorption profiles for transitions from the upper ground hyperfine energy level  $F_g = 2$  of the D2 line of  $^{87}\text{Rb}$  are shown in Figs. 4.12, 4.13, and 4.14. A major difference in the effects of neighboring transitions in  $^{87}\text{Rb}$  atoms compared to  $^{85}\text{Rb}$  atoms is that transitions from hyperfine ground states of  $^{87}\text{Rb}$  have larger hyperfine splittings. Instead of EIA, the close  $F_g = 2 \rightarrow F_e = 3$  transition exhibits EIT at a 0 degree  $\theta_R$ , whereas the open  $F_g = 2 \rightarrow F_e = 2$  and  $F_g = 2 \rightarrow F_e = 1$  transitions exhibit EIAs at higher  $\theta_R$ , as shown in Figs. 4.12 (c), 4.13 (c), and 4.14 (c).

The DTLS and DMLS calculated absorption profiles and experimental spectra for the close  $F_g = 2 \rightarrow F_e = 3$  transition are shown in Figs. 4.12 (a)–(c). EIT instead of EIA appears at a 0 degree polarization angle that switches to EIA at 10 degrees. After switching to EIA, the spectral profiles grow in amplitude with an increase in  $\theta_R$ . The maximum amplitude of EIA appears at 90 degrees, as shown in Fig. 4.12 (c). The experimental profiles match well the calculated DMLS absorption spectra shown in Fig. 4.12 (b) with EIT at 0 degrees, and after switching to EIA, they grow. The influence of close-by open  $F_g = 2 \rightarrow F_e = 2$  and  $F_g = 2 \rightarrow F_e = 1$  transitions is what causes EIT at 0 degrees. This is why calculated DTLS absorption profiles without the contribution from neighboring transitions have EIAs at all  $\theta_R$ , as shown in Fig. 4.12 (a). The DTLS EIAs also grow in amplitude with an increase in  $\theta_R$ .

The open  $F_g = 2 \rightarrow F_e = 2$  has growing EITs with increasing  $\theta_R$  for DTLS with relatively small amplitudes, as shown in Fig. 4.13 (a). Because of the dominating close  $F_g = 2 \rightarrow F_e = 3$  transition, the calculated DMLS absorption profiles are switching from EIT to EIA at a 20 degree  $\theta_R$ , as shown in Fig. 4.13 (b). Similarly, experimental spectra show a shift from EIT to EIA in Fig. 4.13 (c). After switching, EIA grows in amplitude with increasing  $\theta_R$ , and maximum amplitude is recorded at a 90 degree  $\theta_R$ . EIT, on the other hand, has maximum amplitude at 0 degrees  $\theta_R$  for both DMLS and experimental spectra.



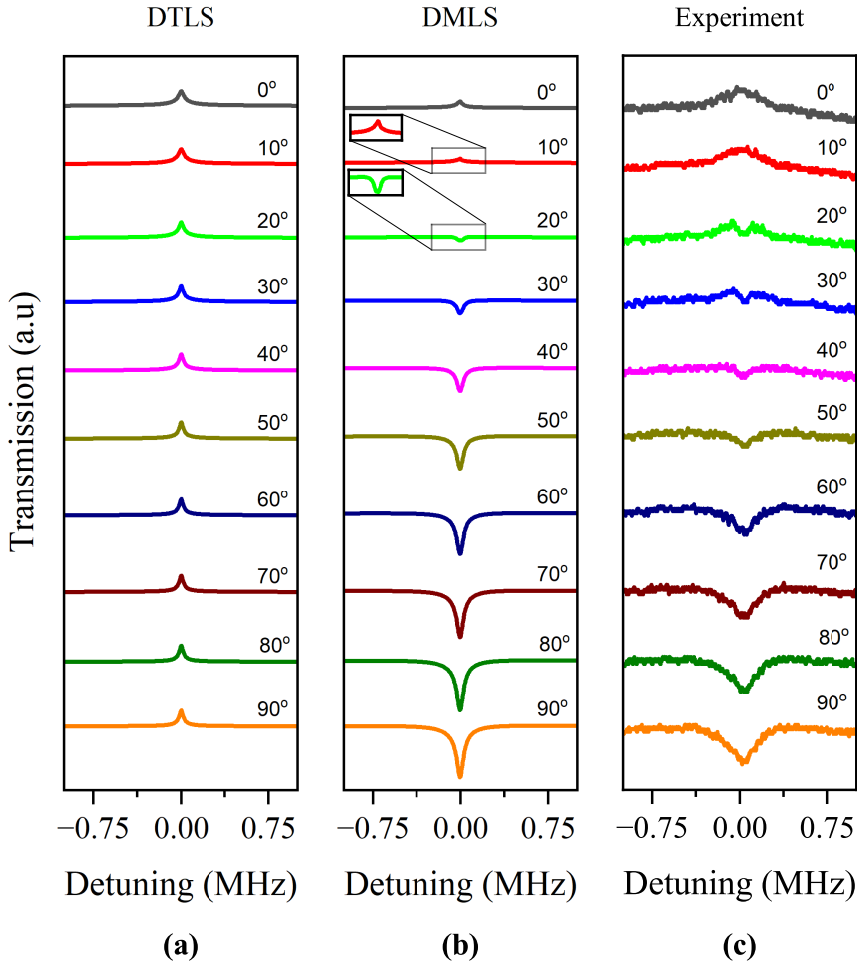


**Figure 4.13:** Comparison of calculated and measured spectra for  $F_g = 2 \rightarrow F_e = 2$  transition considering (a) pure two-level resonant transition (b) a transition resonant at  $F_g = 2 \rightarrow F_e = 2$  with neighboring hyperfine transitions  $F_g = 2 \rightarrow F_e = 3$  and  $F_g = 2 \rightarrow F_e = 1$  (c) experimentally measured spectra for resonant transition  $F_g = 2 \rightarrow F_e = 2$ .

The  $F_g = 2 \rightarrow F_e = 1$  transition also has growing EITs with increasing  $\theta_R$  for DTLS, as shown in Fig. 4.14 (a). This transition is further away from the  $F_g = 2 \rightarrow F_e = 3$  transition because hyperfine splitting is large, which is why the EIT switches to EIA at a larger  $\theta_R$  as compared to  $F_g = 2 \rightarrow F_e = 2$  for DMLS calculations results shown in Fig. 4.14 (b). Experimental spectra switch to EIA at

an even larger angle, as shown in Fig. 4.14 (c), and do not match well the DMLS absorption profiles.

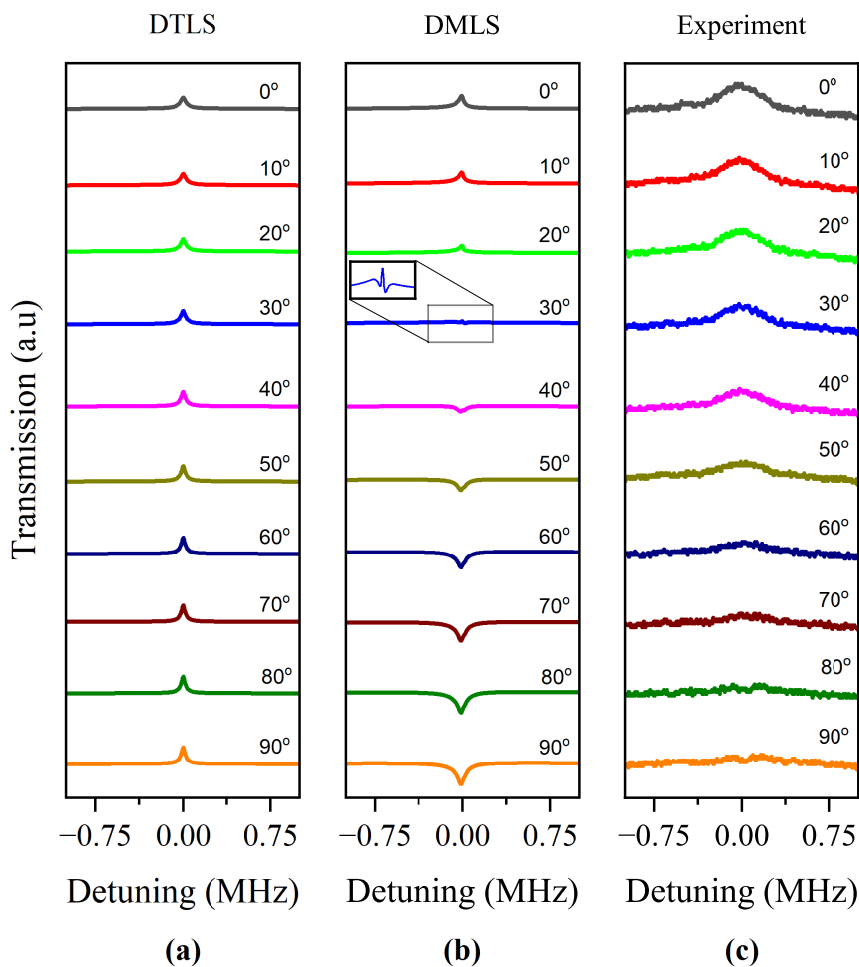


**Figure 4.14:** Comparison of calculated and measured spectra for  $F_g = 2 \rightarrow F_e = 1$  transition considering (a) pure two-level resonant transition (b) a transition resonant at  $F_g = 2 \rightarrow F_e = 1$  with neighboring hyperfine transitions  $F_g = 2 \rightarrow F_e = 3$  and  $F_g = 2 \rightarrow F_e = 2$  (c) experimentally measured spectra for resonant transition  $F_g = 2 \rightarrow F_e = 1$ .

## 4.5 Summary

The measurement and calculation of crucial polarization angles have been carried out within the framework of linear polarization of coupling and probe laser beams, particularly in scenarios where EIT exhibits an amplification in magnitude or can be converted into EIA. The experiments conducted thus far have mostly concentrated on the D2 line of the  $^{85}\text{Rb}$  and  $^{87}\text{Rb}$  atoms. The procedure entails the examination of two separate ground state hyperfine lines,  $F_g = 2$  and  $F_g = 3$  of  $^{85}\text{Rb}$  atoms, and  $F_g = 1$  and  $F_g = 2$  of  $^{87}\text{Rb}$  atoms, correspondingly.

The coupling and probe beams are initially polarized in a linear and parallel configuration. The coupling beam's polarization angle is systematically incremented by 10 degrees, reaching a maximum of 90 degrees. For each increment, a spectral profile is recorded. The closed transitions of  $F_g = 2 \rightarrow F_e = 4$  in  $^{85}\text{Rb}$  and  $F_g = 2 \rightarrow F_e = 3$  in  $^{87}\text{Rb}$  exhibit EIT at an angle of 0 degrees. However, they transition to EIA at a greater  $\theta_R$ . In addition, it is observed that the open transitions  $F_g = 3 \rightarrow F_e = 2$  and 3 of  $^{85}\text{Rb}$ , as well as  $F_g = 2 \rightarrow F_e = 1$  and 2 of  $^{87}\text{Rb}$ , exhibit EIT at lower  $\theta_R$ . However, as the rotational angle increases, these EIT shift to EIA. This transition is mostly attributed to the impact of neighboring hyperfine transitions. This has been confirmed by the calculation of absorption profiles for degenerate two level systems (DTLS) without neighboring transitions, as well as degenerate multi level systems (DMLS) featuring neighboring transitions.

The transitions from the lower ground hyperfine energy levels of  $^{85}\text{Rb}$  and  $^{87}\text{Rb}$  demonstrate EIT. Upon doing a comparative analysis between the experimental spectra and the absorption profiles obtained through DTLS and DMLS calculations, it becomes apparent that the presence of neighboring transitions significantly impacts each transition. This influence leads to an observable increase in the amplitude of EITs for transitions originating from lower ground hyperfine energy levels.

## Chapter 5

# Coherent Control of EIA and EIT

## 5.1 Overview

This chapter provides a description of the effects of neighboring transitions with respect to the artificial variation in the hyperfine splitting of Rb atoms. The influence of neighboring transitions on the exhibition of coherent absorption profiles is significant and the strength of this influence depends on the hyperfine splitting of the states. The chapter is organized as follows: Section 5.2 presents the influence of neighboring transitions with respect to artificially varying hyperfine splitting of  $^{87}\text{Rb}$  atoms with linear parallel ( $\pi\|\pi$ ) and linear perpendicular ( $\pi\perp\pi$ ) configuration of the coupling and probe beams. Section 5.3 describes the influence of neighboring transitions with respect to artificially varying hyperfine splitting of  $^{85}\text{Rb}$  atoms with same circular ( $\sigma\|\sigma$ ) and circular orthogonal ( $\sigma\perp\sigma$ ) configuration of the coupling and probe beams and Sec. 5.4 presents some concluding remarks.

## 5.2 Artificial Variation in Hyperfine Splitting of $^{87}\text{Rb}$

The requirements proposed by Lezama [98] are widely recognized and give rise to electromagnetically induced absorption (EIA) in the context of the degenerate two-level system (DTLS), as expressed below:

- The ground state must exhibit degeneracy
- $F_e = F_g + 1$
- The transition from  $F_g \rightarrow F_e$  must be closed

Nevertheless, the established standards of EIA in DTLS may be compromised under certain circumstances, such as when dealing with a particular polarization configuration and power ratios between coupling and probe beams, among other

factors. The EIA can be compromised by the influence of neighboring transitions, which is contingent upon the spacing between the hyperfine levels in the excited state of the transition. In this study, we investigate the relationship between nearby transitions and spectral profiles in the  $5P_{3/2}$  state of  $^{87}\text{Rb}$ , focusing on the variations that occur as a result of different hyperfine spacings. In addition, we provide instances where Lezama's criteria are not met, specifically in the context of the  $F_g = 2 \rightarrow F_e = 3$  transition of  $^{87}\text{Rb}$  atoms in the  $\pi\|\pi$  configuration, where the broken case of electromagnetically induced transmission (EIT instead of EIA) is observed. This deviation from the expected behavior is distinct from the observed EIAs in the  $\pi\perp\pi$  configuration for the same  $F_g = 2 \rightarrow F_e = 3$  transition, particularly under conditions of low coupling power. Notably, this is the first time such broken cases have been reported. The observation of EITs in the  $\pi\|\pi$  configuration and EIAs in the  $\pi\perp\pi$  configuration for the open  $F_g = 2 \rightarrow F_e = 1$  and 2 transitions can be attributed to the influence of neighboring effects. This study demonstrates that the influence of neighboring transitions on the observed EIA or EIT transformation for the  $F_g = 2 \rightarrow F_e = 1, 2,$  and 3 transitions of the  $^{87}\text{Rb}$  D2 line is contingent upon the polarization configuration of the coupling and probe beams.

### 5.2.1 Methods

The EIA spectra for the perpendicular ( $\pi\perp\pi$ ) and parallel ( $\pi\|\pi$ ) configurations is calculated using the identical methodologies outlined in Sec. 4.2. Given that the sole discrepancy between the calculations outlined in Sec. 4.2 pertains to the configuration of the energy level, we abstain from providing an elaborate exposition of the theoretical background. The atomic energy level diagrams pertaining to the D2 transition lines of  $^{87}\text{Rb}$  are depicted in Fig. 5.1 (a). The figure depicted in Fig. 5.1 (b) illustrates the level schemes that are taken into account for the transition from the ground state  $F_g = 2$  to the excited state  $F_e = 3$ . This transition is studied in the presence of two beams, namely the coupling beam and the probe beam, which are configured in the  $\pi\perp\pi$  and  $\pi\|\pi$  orientations, respectively.

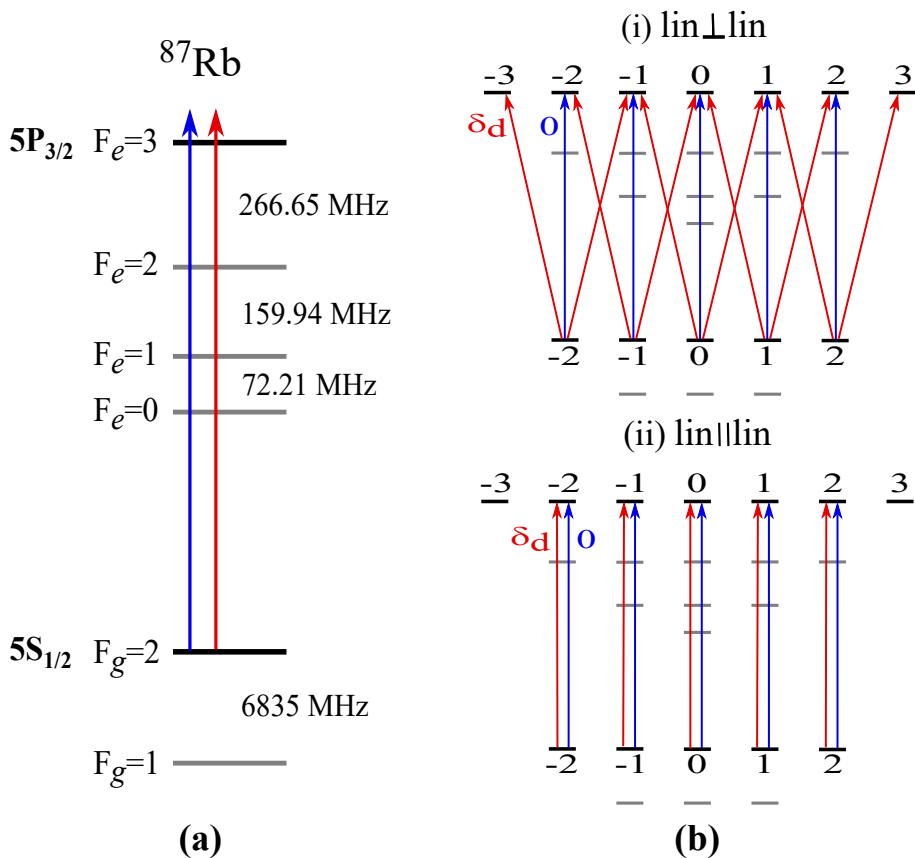


**Figure 5.1:** (a) Energy level diagram of  $^{87}\text{Rb}$  D2 transition line, wherein the red and blue lines indicate transitions by the probe and coupling beams, respectively. (b) Level schemes considered in the case of the  $F_g = 2 \rightarrow F_e = 3$  transition with two coupling and probe beams in (i)  $\pi \perp \pi$  and, (ii)  $\pi \parallel \pi$  configurations.

Fig. 4.2 displays a schematic illustration of the experimental setup. The generation of coupling and probe beams is facilitated through the utilization of a single tunable external cavity diode laser (DLPro, Toptica Inc.). The experimental arrangement of saturation absorption spectroscopy (SAS), as described in Sec. 1.1.2, is employed to stabilize the laser frequency at transition within the D2 line of  $^{87}\text{Rb}$ . The half-wave plate (HWP) is employed to effectively control polarization and sustain powers of  $50 \mu\text{W}$  and  $15 \mu\text{W}$  for the coupling and probe beams, respectively. The scanning detuning ( $\Delta$ ) of the coupling beam is accomplished by

transmitting it through a configuration consisting of two acoustic optic modulators (AOMs) in a single-pass arrangement. In order to achieve a uniform intensity across a 4-mm diameter, both the coupling and probe beams are subjected to a five-fold expansion using beam expanders (BE). A beam splitter (BS) facilitates the passage of co-propagating coupling and probe beams through the vapor cell. A separation angle of approximately  $\sim 0.1$  mRad is maintained in order to separate the probe beam at the photo detector (PD). The study is performed under the ambient conditions, utilizing  $^{87}\text{Rb}$  atoms that were confined within a reference vapor cell. To mitigate the influence of stray and terrestrial magnetic fields within the vapor cell, a protective measure is implemented by enclosing the cell with a layers of five  $\mu$ -metal sheets.

## 5.2.2 Results and Discussion

The first panel of Figs. 4.12, 4.13, and 4.14 recorded at 0 degree presents the comparison between DTLS calculation, degenerate multi-level system (DMLS) calculation and experimental spectra for linear parallel polarization of coupling and probe beams, whereas the last panel of Figs. 4.12, 4.13, and 4.14 recorded at 90 degrees presents the comparison between DTLS calculation, DMLS calculation and experimental spectra for linear perpendicular polarization of coupling and probe beams for the  $F_g = 2 \rightarrow F_e = 3$ ,  $F_g = 2 \rightarrow F_e = 2$ , and  $F_g = 2 \rightarrow F_e = 1$  transitions of D2 line of  $^{87}\text{Rb}$  atoms. The DTLS calculations are done without considering the effects of neighboring transitions, whereas DMLS calculations take into account the effect of neighboring transitions.

The top panel (at 90 degrees) of Fig. 4.12 (a) shows a relatively strong amplitude of EIA for the closed transition  $F_g = 2 \rightarrow F_e = 3$ , when employing a pure DTLS system that fulfills all the required EIA requirements [98]. Two open transitions  $F_g = 2 \rightarrow F_e = 2$  and  $F_g = 2 \rightarrow F_e = 1$  exhibit EITs, as shown in Figs. 4.13 (a), and 4.14 (a). The absorption profiles obtained by considering the neighboring transitions adjacent to the resonant transitions  $F_g = 2 \rightarrow F_e = 1$ ,  $F_g = 2 \rightarrow F_e = 2$ , and  $F_g = 2 \rightarrow F_e = 3$  generate EIAs, primarily caused by the dominant

closed transition  $F_g = 2 \rightarrow F_e = 3$ , shown in top panel of Figs. 4.12 (b), 4.13 (b), and 4.14 (b). Similar trend of all transitions exhibiting EIAs is recorded for the experimentally measured spectra depicted in top panel of Figs. 4.12 (c), 4.13 (c), and 4.14 (c). The amplitude of EIAs exhibits a declining pattern as the excited state angular quantum number  $F_e$  decreases, as observed in both experimental and DMLS calculations that take into account all neighboring transitions. The disparity in amplitude can be attributed to the variation in energy between the hyperfine levels of the excited states  $F_g = 2 \rightarrow F_e = 1$  and  $F_g = 2 \rightarrow F_e = 2$ , which are separated by 426.59 MHz and 266.65 MHz, respectively, from the closed transition  $F_g = 2 \rightarrow F_e = 3$ .

The experimental findings pertaining to  $^{87}\text{Rb}$  atoms showcased in the top panel of Figs. 4.12, 4.13, and 4.14 exhibit a notable resemblance to the outcomes observed first panel of Figs. 4.6, 4.7, and 4.8 for  $^{85}\text{Rb}$  atoms. This suggests that the qualitative impact of neighboring transitions on  $^{87}\text{Rb}$  and  $^{85}\text{Rb}$  is comparable. Hence, it would be quite intriguing to observe the extent to which the impact of neighboring transitions fluctuates based on the hyperfine frequency spacing within the  $5P_{3/2}$  state. In order to investigate this particular phenomenon, we employ a theoretical approach to determine the EIA spectra for atoms of  $^{87}\text{Rb}$ . This is achieved by artificially manipulating the hyperfine frequency spacings. The ratio presented in Fig. 5.2 represents the artificial amplification factor of the hyperfine splittings seen in  $^{87}\text{Rb}$ . For instance, when the ratio is 0.5, the hyperfine splittings exhibit a reduction to half of those observed for  $^{87}\text{Rb}$ .

The calculated results for the  $\pi \perp \pi$  arrangement are illustrated in Fig. 5.2. Fig. 5.2 (a), (b), and (c) present the outcomes pertaining to the transitions  $F_g = 2 \rightarrow F_e = 3$ ,  $F_g = 2 \rightarrow F_e = 2$ , and  $F_g = 2 \rightarrow F_e = 1$ , respectively. These results were obtained through the artificial manipulation of the hyperfine spacings. The EIA in Fig. 5.2 (a) exhibits no changes when subjected to varying hyperfine spacings. The EIA of  $F_g = 2 \rightarrow F_e = 3$  closed transition is very stable. Furthermore, the influence of any open transitions on this transition is negligible. Therefore, the characteristic of EIA remains unchanged irrespective of the amplification factor. In Fig. 5.2 (b), the EIA of  $F_g = 2 \rightarrow F_e = 2$  open transition undergoes a transfor-



mation to a EIT as the ratio grows. With growing ratio, the impact of  $F_g = 2 \rightarrow F_e = 3$  closed transition becomes less pronounced. Therefore, the signal achieves complete transmission. The transition from the EIA to the EIT takes place when the ratio approaches a value of around 1.9. The outcomes corresponding to the  $F_g = 2 \rightarrow F_e = 1$  transition, as seen in Fig. 5.2 (c), demonstrate comparable characteristics to those observed in the  $F_g = 2 \rightarrow F_e = 2$  transition. The transition depicted in Fig. 5.2 (c) takes place at a ratio of 1.2. This value is justifiable as the resonance line for the  $F_g = 2 \rightarrow F_e = 3$  transition is further away compared to the scenario illustrated in Fig. 5.2 (b).

The first panel of Figs. 4.12, 4.13, and 4.14 present calculated and measured spectra for the D2 line of  $^{87}\text{Rb}$  with respect to the  $\pi||\pi$  configuration of coupling and probe laser beams. The first panel of Figs. 4.12 (a), 4.13 (a), and 4.14 (a) depict the calculations of pure DTLS system, whereas the first panel of Figs. 4.12 (b), 4.13 (b), and 4.14 (b) take into account the neighboring transitions. The first panel of Figs. 4.12 (c), 4.13 (c), and 4.14 (c) displays the spectra obtained from experimental measurements of the resonant transitions  $F_g = 2 \rightarrow F_e = 3$ ,  $F_g = 2 \rightarrow F_e = 2$ , and  $F_g = 2 \rightarrow F_e = 1$ .

The  $F_g = 2 \rightarrow F_e = 2$  open transition exhibits the strongest EIT signal for DTLS calculation, as shown in first panel of Fig. 4.13, among other transitions and dominates the neighboring effect onto other transitions. The DMLS considering neighboring transition and experimental spectra obtained for  $F_g = 2 \rightarrow F_e = 3$ ,  $F_g = 2 \rightarrow F_e = 2$ , and  $F_g = 2 \rightarrow F_e = 1$  transitions show up as EITs, as shown in the first panel of Figs. 4.12 (b-c), 4.13 (b-c), and 4.14 (b-c), respectively. The  $F_g = 2 \rightarrow F_e = 1$  transition has the strongest EIT for DMLS calculations and experimental spectra which is largely due to the strong EIT of  $F_g = 2 \rightarrow F_e = 2$  in DTLS. The  $F_g = 2 \rightarrow F_e = 3$  close transition also exhibit weak EITs in DMLS calculation and experimental spectral profile instead of EIA pertaining to the  $F_g = 2 \rightarrow F_e = 2$  open transition.

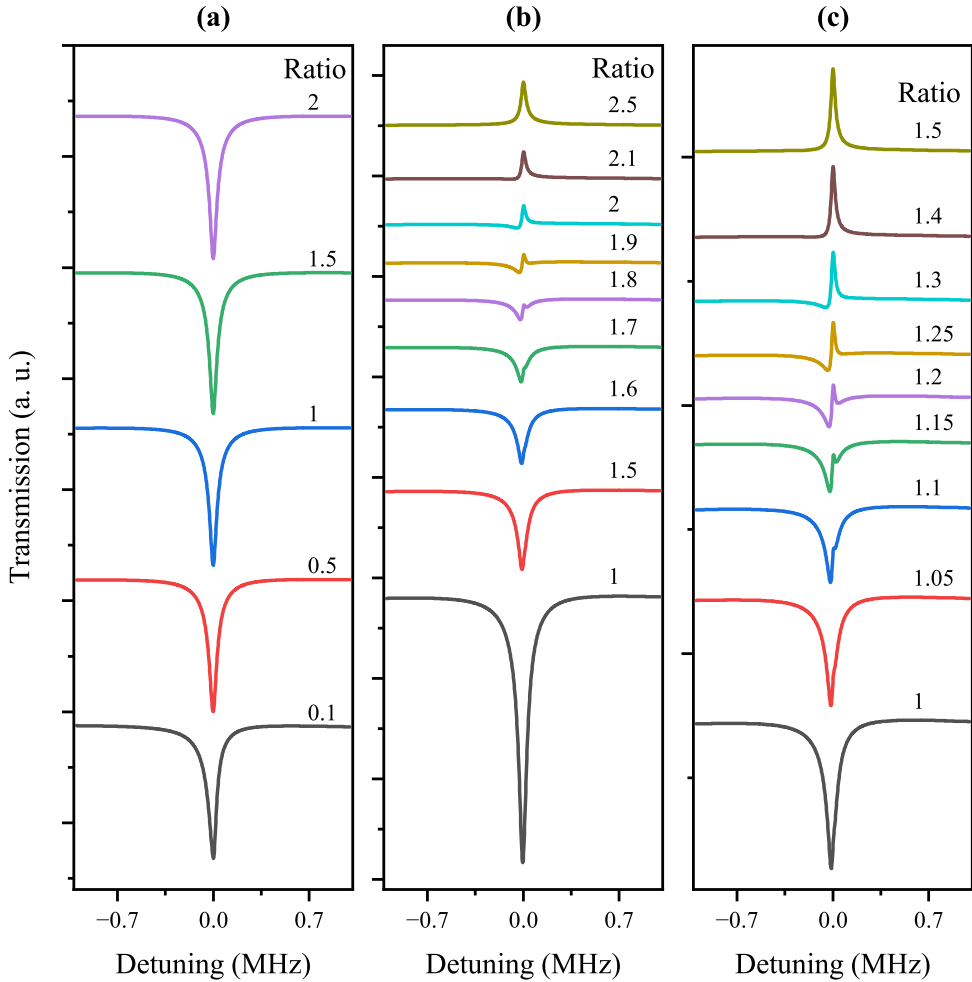


**Figure 5.2:** The spectral characteristics of the  $\pi \perp \pi$  configuration with artificial variation in the hyperfine splittings of  $^{87}\text{Rb}$  for the (a)  $F_g = 2 \rightarrow F_e = 3$ , (b)  $F_g = 2 \rightarrow F_e = 2$ , and (c)  $F_g = 2 \rightarrow F_e = 1$  transitions.

Fig. 5.3 (a), (b), and (c) depict the results by artificially varying the hyperfine splitting for the  $\pi \parallel \pi$  configuration of the  $F_g = 2 \rightarrow F_e = 3$ ,  $F_g = 2 \rightarrow F_e = 2$ , and  $F_g = 2 \rightarrow F_e = 1$  transitions, respectively. Fig. 5.3 (a) illustrates the transition of the EIT signal to the EIA signal as the ratio grows, specifically for the  $F_g = 2 \rightarrow F_e = 3$  transition. The transition takes place when the ratio reaches an estimated value of 1.15. The EIT signal observed at this transition can be attributed to the

influence of the  $F_g = 2 \rightarrow F_e = 2$  and  $F_g = 2 \rightarrow F_e = 1$  open transitions. As the ratio of artificial hyperfine splittings grow, there is a corresponding reduction in the impact of the open transition. The EIT signals observed in Figs. 5.3 (b) and (c) remain unchanged even when the ratio is less than one. This suggests that the influence of the  $F_g = 2 \rightarrow F_e = 3$  closed transition is significantly weaker in the  $\pi||\pi$  configuration compared to the  $\pi\perp\pi$  configuration.

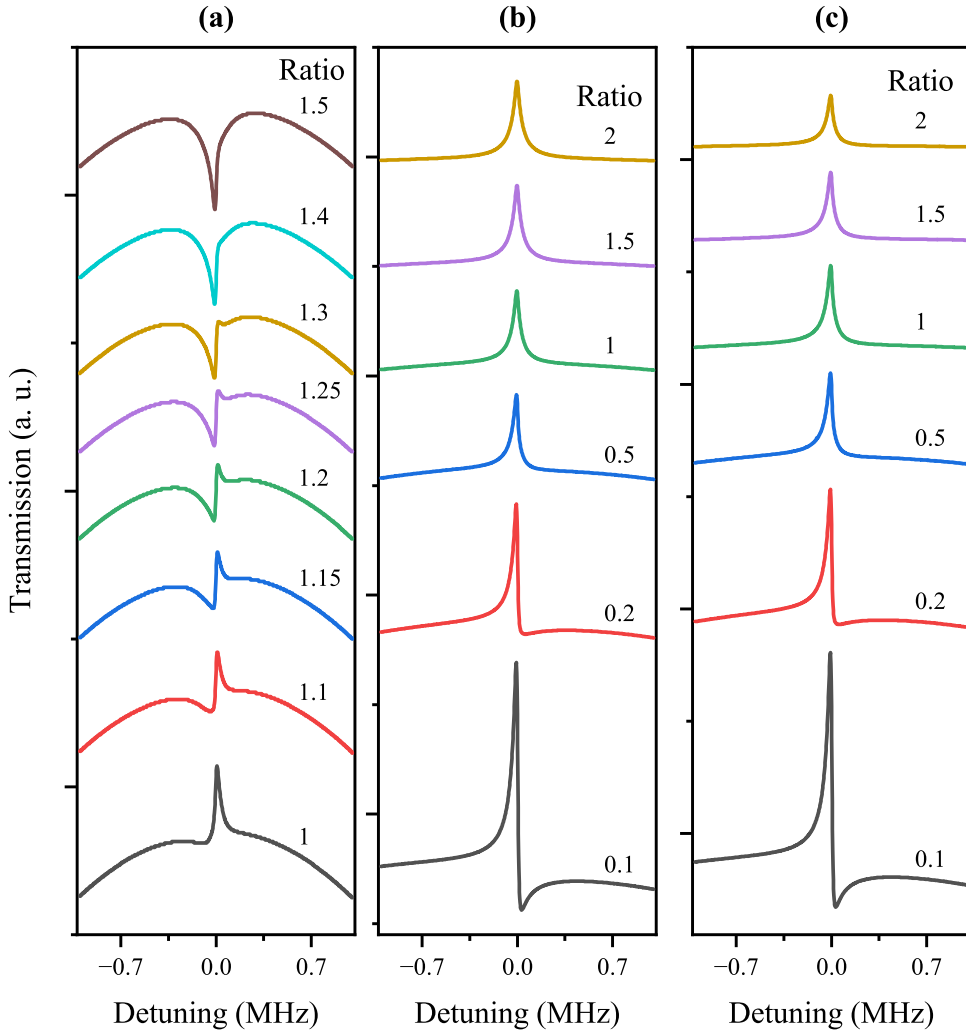


**Figure 5.3:** The spectral characteristics of the  $\pi||\pi$  configuration with artificial variation in the hyperfine splittings of  $^{87}\text{Rb}$  for the (a)  $F_g = 2 \rightarrow F_e = 3$ , (b)  $F_g = 2 \rightarrow F_e = 2$ , and (c)  $F_g = 2 \rightarrow F_e = 1$  transitions.

## 5.3 Artificial Variation in Hyperfine Splitting of $^{85}\text{Rb}$

In order to comprehend the contrasting behavior exhibited by the coherent resonances in the  $\pi\parallel\pi$  and  $\pi\perp\pi$  configuration of coupling and probe beams, the spectral changes in the  $F_g = 3 \rightarrow F_e = 2$  transition of  $^{85}\text{Rb}$  by artificially manipulating the hyperfine splittings of  $^{85}\text{Rb}$  is also presented with respect to the  $\sigma\parallel\sigma$  and  $\sigma\perp\sigma$  configurations of coupling and probe beams. The method for calculating DTLS absorption profiles without neighboring transitions and DMLS absorption profiles considering the neighboring transitions is same as described in Sec. 4.2.

### 5.3.1 Experimental Setup

A polarizing beam splitter (PBS) is used to separate a beam emitted by a single tunable external cavity diode laser (DLPro, Toptica Inc.) with a wavelength of 780 nm. The probe beam and the pump beam were generated using a single laser equipped with two acousto-optic modulators (AOMs, 3080-122, Gooch & Housego). The utilization of a half-wave plate (HWP) positioned right before the polarizing beam splitter (PBS) facilitated the regulation of the beam powers for both the coupling and probing beams. The desired configuration of circular polarization for the coupling and probe beams is manipulated by employing a combination of a HWP and quarter-wave plates (QWP) prior to a beam splitter (BS), as depicted in Fig. 5.4. The beam splitter (BS) is employed to spatially overlap the co-propagating coupling and probe beams within the Rb vapor cell. The power of the probe and coupling beams are measured to be  $15 \mu\text{W}$  and  $50 \mu\text{W}$ , respectively.

The coupling beam was scanned by passing it through AOMs in a single-pass configuration. The modulation frequency of one of AOMs is set at a constant value of 80 MHz, while the second AOM is varied within a range of  $\pm 1$  MHz centered around -80 MHz. The RF spectrum analyzer (Tektronix 2712) was employed to calibrate the time axis, specifically in terms of frequency, of the oscil-

loscope. The purpose of scanning the coupling beam was to mitigate the effects of Doppler broadening. To ensure a uniform beam with a diameter of 4 mm, both the coupling and probe beams underwent a five-fold expansion using the beam expander (GBE05-B, Thorlabs). The vapor cell, which measures 5 cm in length and 2.5 cm in diameter, is effectively protected by five layers of  $\mu$ -metal sheets. This shielding effectively prevents any interference from external magnetic fields, including both stray fields and the Earth's magnetic field.

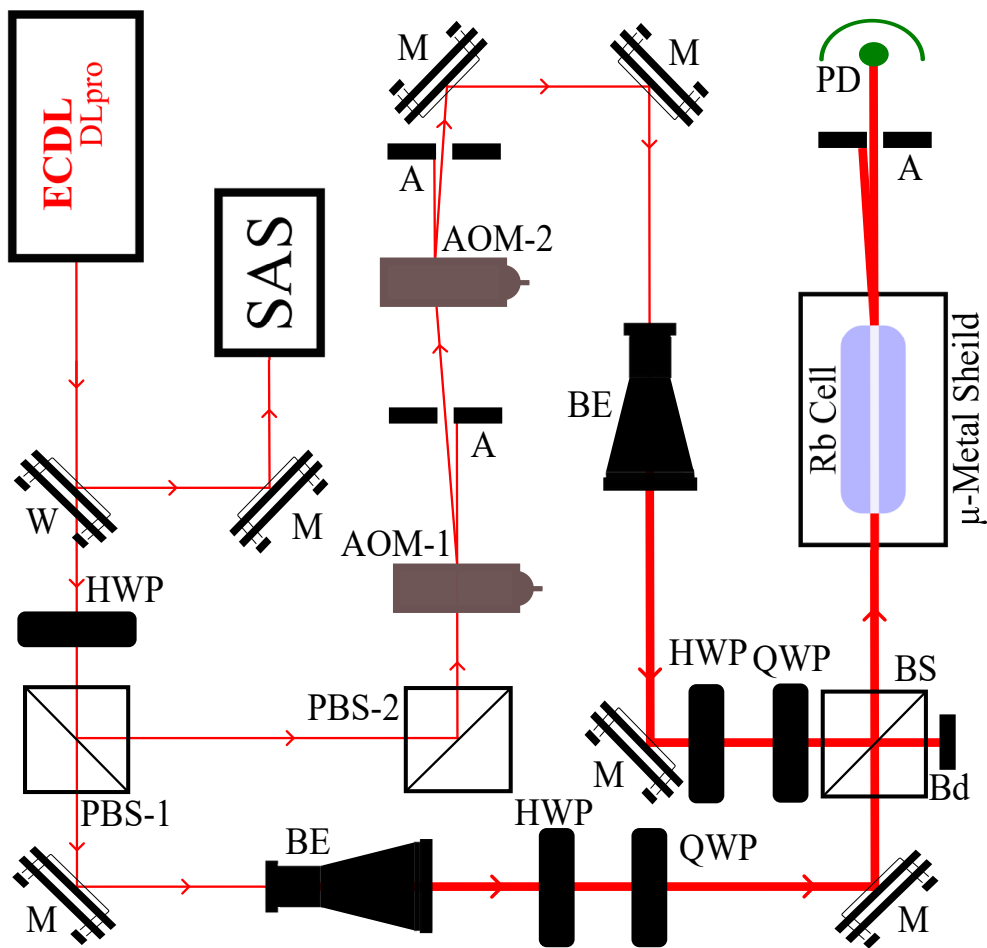


**Figure 5.4:** Schematic diagram of experimental setup. Component symbols: SAS: saturation absorption spectroscopy; W: window; HWP: halfwave plate; QWP: quarter-wave plate; PBS: polarizing beam splitter; BE: beam expander; A: aperture; AOM: acousto-optic modulator; M: mirror; BS: beam splitter; Bd: beam dump; PD: photodetector.

### 5.3.2 Results and Discussion

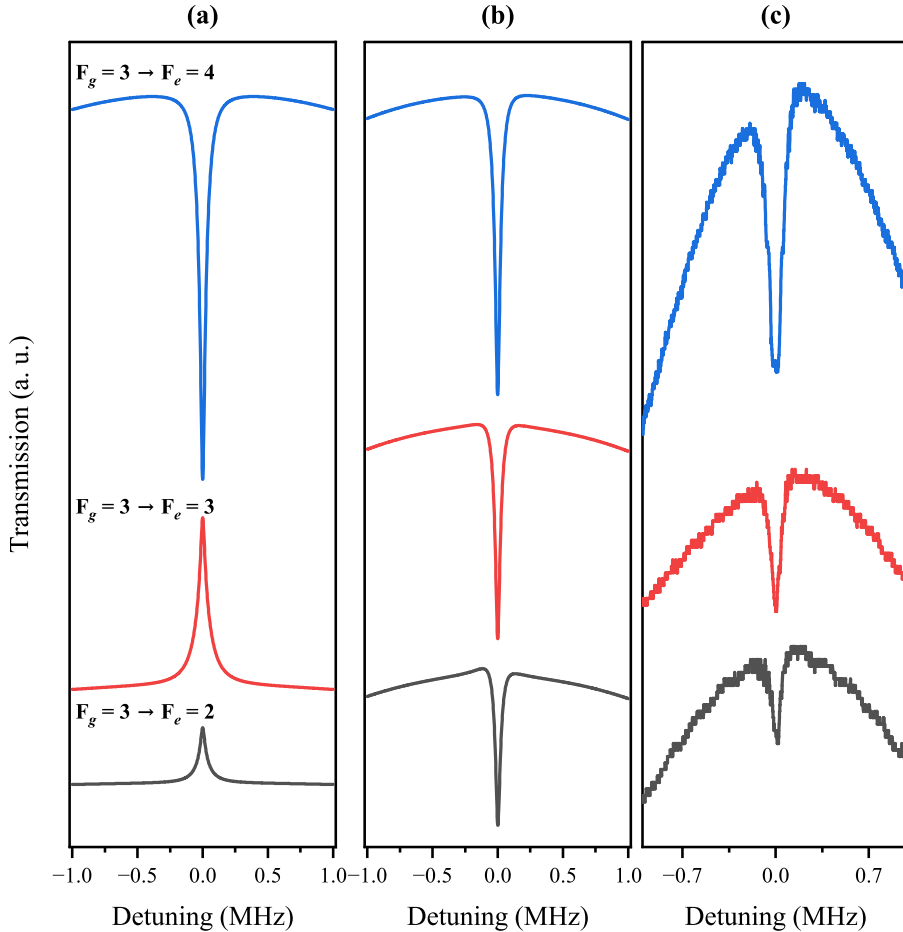


**Figure 5.5:** Spectral profiles with  $\sigma \parallel \sigma$  configuration of coupling and probe beams at  $F_g = 3 \rightarrow F_e = 2, 3,$  and  $4$  of  $^{85}\text{Rb}$  D2 line considering (a) DTLS calculations without neighboring effects of  $F_g = 3 \rightarrow F_e = 2, F_g = 3 \rightarrow F_e = 3,$  and  $F_g = 3 \rightarrow F_e = 4$  transitions; (b) DMLS calculations (with neighboring effects) of  $F_g = 3 \rightarrow F_e = 2$  (3 and 4),  $F_g = 3 \rightarrow F_e = 3$  (2 and 4), and  $F_g = 3 \rightarrow F_e = 4$  (2 and 3); and (c) experimentally measured spectra for  $F_g = 3 \rightarrow F_e = 2, F_g = 3 \rightarrow F_e = 3,$  and  $F_g = 3 \rightarrow F_e = 4$  transitions.

The DTLS absorption profile of  $F_g = 3 \rightarrow F_e = 4$  closed transition exhibit strong EIA while open transitions  $F_g = 3 \rightarrow F_e = 3$  and  $F_g = 3 \rightarrow F_e = 2$  exhibit EITs, as shown in Fig. 5.5 (a). The DMLS spectra of  $F_g = 3 \rightarrow F_e = 4$  with neighboring

transitions  $F_g = 3 \rightarrow F_e = 3$  and  $2$ ,  $F_g = 3 \rightarrow F_e = 3$  with neighboring transitions  $F_g = 3 \rightarrow F_e = 4$  and  $2$ , and  $F_g = 3 \rightarrow F_e = 2$  with neighboring transitions  $F_g = 3 \rightarrow F_e = 4$  and  $3$  present EIAs, as shown in Fig. 5.5 (b). The experimental profiles match well with the calculated DMLS profiles and confirm the influence of neighboring hyperfine  $F_g = 3 \rightarrow F_e = 4$  closed transition on  $F_g = 3 \rightarrow F_e = 3$  and  $F_g = 3 \rightarrow F_e = 2$ , as shown in Fig. 5.5 (c).

Same should be true for transitions from upper ground state  $F_g = 3$  of  $^{87}\text{Rb}$  atoms, but  $^{87}\text{Rb } F_g = 2 \rightarrow F_e = 1$  transition exhibit EIT [77]. The reason for weak neighboring effect of  $^{87}\text{Rb } F_g = 2 \rightarrow F_e = 3$  closed transition on neighboring  $^{87}\text{Rb } F_g = 2 \rightarrow F_e = 2$  and  $^{87}\text{Rb } F_g = 2 \rightarrow F_e = 1$  is due to the large hyperfine splitting of  $^{87}\text{Rb}$  atoms. Fig. 5.6 presents the artificial variation of hyperfine energy splittings of  $F_g = 3 \rightarrow F_e = 2$  transition of  $^{85}\text{Rb}$  atoms with same circular polarization of coupling and probe beams. The profile at unity ratio corresponds to the DMLS absorption profile for the  $F_g = 3 \rightarrow F_e = 2$ , whereas ratio of 2.3 corresponds to the hyperfine energy splitting of  $F_g = 2 \rightarrow F_e = 1$  transition of  $^{87}\text{Rb}$  atoms.

The ratio depicted in Fig. 5.6 suggests the artificial amplification factor of the hyperfine splittings observed in  $^{85}\text{Rb}$ . It is worth noting that the factor of 2.3 is a close approximation to the hyperfine splittings seen in  $^{87}\text{Rb}$ . The trace observed at the unity ratio in Fig. 5.6, which demonstrates the phenomenon of EIA, is identical to the trace depicted in the lowest panel of Fig. 5.5. As the ratio grows, there is an observable alteration in the spectral profile, leading to a transformation of the EIA to EIT. This transformation occurs within a ratio range of around 1.5 to 1.8. It is observed that there are no substantial disparities in the spectra of  $^{87}\text{Rb}$  and  $^{85}\text{Rb}$  atoms when the hyperfine splittings are artificially adjusted to comparable spacings. Fig. 5.6 illustrates the contrasting resonant characteristics seen in the  $^{87}\text{Rb}$  system for the  $F_g = 2 \rightarrow F_e = 1$  transition and the  $F_g = 3 \rightarrow F_e = 2$  transition. In terms of qualitative analysis, it can be observed that an increase in hyperfine splitting leads to decrease in neighboring effects.

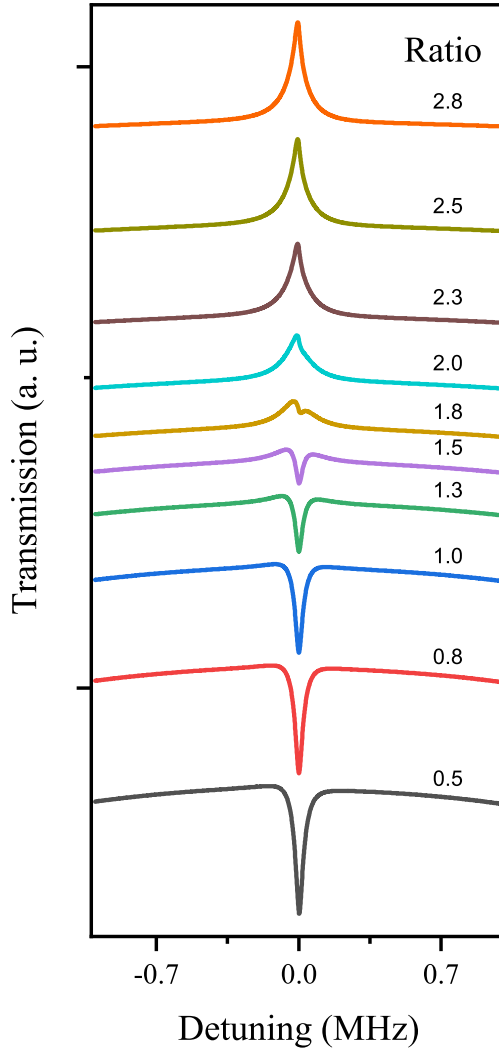


**Figure 5.6:** Spectral profile with artificial variation in hyperfine splitting of  $F_g = 3 \rightarrow F_e = 2$  transition of  $^{85}\text{Rb}$  with respect to circular parallel ( $\sigma\parallel\sigma$ ) configuration of coupling and probe beams.

The circular orthogonal ( $\sigma\perp\sigma$ ) polarization of coupling and probe beam is illustrated in Fig. 5.7. A strong split EIA is observed for  $F_g = 3 \rightarrow F_e = 4$  closed transition of  $^{85}\text{Rb}$  atoms for DTLS calculations, as shown in the top panel of Fig. 5.7 (a). The open  $F_g = 3 \rightarrow F_e = 3$  and  $F_g = 3 \rightarrow F_e = 2$  transitions, on the



other hand, exhibit EITs for DTLS. The DMLS spectra of  $F_g = 3 \rightarrow F_e = 4$  with neighboring transitions  $F_g = 3 \rightarrow F_e = 3$  and 2,  $F_g = 3 \rightarrow F_e = 3$  with neighboring transitions  $F_g = 3 \rightarrow F_e = 4$  and 2, and  $F_g = 3 \rightarrow F_e = 2$  with neighboring transitions  $F_g = 3 \rightarrow F_e = 4$  and 3 present split EIAs just like the split EIA of  $F_g = 3 \rightarrow F_e = 4$  transition in DTLS, as shown in Fig. 5.7 (b). The experimental spectra, shown in Fig. 5.7 (c), has split EIAs for all  $F_g = 3 \rightarrow F_e = 4, 3,$  and 2 transitions.

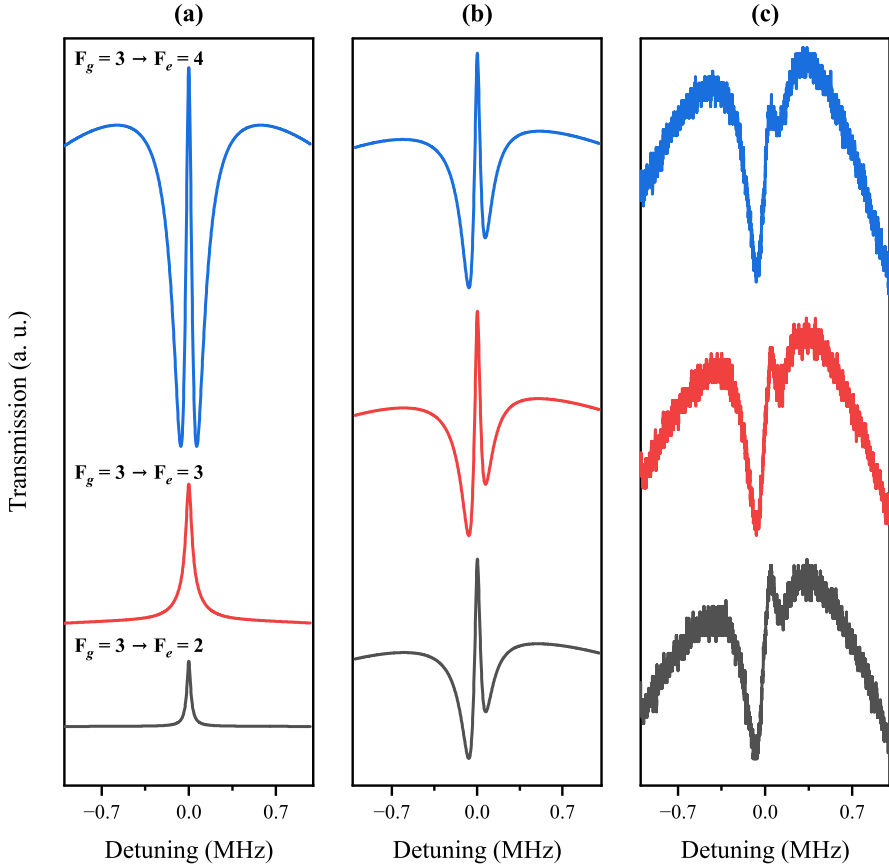


**Figure 5.7:** Spectral profiles with  $\sigma \perp \sigma$  configuration of coupling and probe beams at  $F_g = 3 \rightarrow F_e = 2, 3,$  and 4 of  $^{85}\text{Rb}$  D2 line considering (a) DTLS calculations without neighboring effects of  $F_g = 3 \rightarrow F_e = 2, F_g = 3 \rightarrow F_e = 3,$  and  $F_g = 3 \rightarrow F_e = 4$  transitions; (b) DMLS calculations (with neighboring effects) of  $F_g = 3 \rightarrow F_e = 2$  (3 and 4),  $F_g = 3 \rightarrow F_e = 3$  (2 and 4), and  $F_g = 3 \rightarrow F_e = 4$  (2 and 3); and (c) experimentally measured spectra for  $F_g = 3 \rightarrow F_e = 2, F_g = 3 \rightarrow F_e = 3,$  and  $F_g = 3 \rightarrow F_e = 4$  transitions.

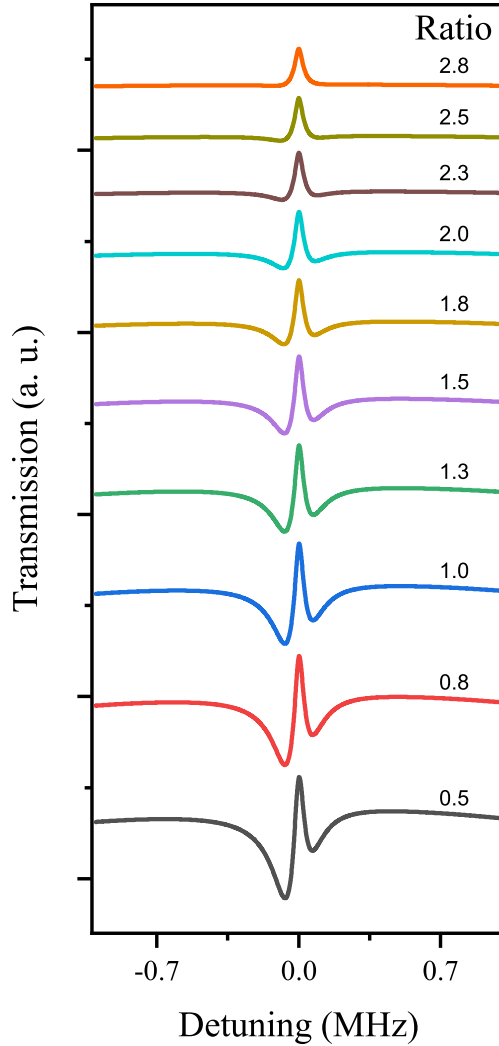


**Figure 5.8:** Spectral profile with artificial variation in hyperfine splitting of  $F_g = 3 \rightarrow F_e = 2$  transition of  $^{85}\text{Rb}$  with respect to circular orthogonal ( $\sigma \perp \sigma$ ) configuration of coupling and probe beams.

In Fig. 5.8, the hyperfine energy splittings of  $^{85}\text{Rb}$  is artificially varied by a factor equivalent to the ratio for  $\sigma \perp \sigma$  configuration of coupling and probe beams. The profile at unity ratio corresponds to the DMLS absorption profile for the  $F_g = 3 \rightarrow F_e = 2$  transition of  $^{85}\text{Rb}$  atoms with circular orthogonal configuration

of coupling and probe beams. The spectra at a ratio of 2.3 corresponds to the hyperfine energy splitting of  $^{87}\text{Rb}$   $F_g = 2 \rightarrow F_e = 1$  transition. Similar to the  $\sigma\|\sigma$  configuration of couplin and probe beams,  $\sigma\perp\sigma$  has weaker influence of neighboring transitions [78].

As the ratio grows, it can be observed that EIA sees a consistent reduction in amplitude. In comparison to the outcomes observed in the  $\sigma\|\sigma$  configuration, the degree of variation is not notably substantial. Upon evaluating the transition strengths associated with the pertinent transitions of the two polarization configurations ( $\sigma\|\sigma$  and  $\sigma\perp\sigma$ ), it is evident that the overall transition strengths in the scenario of the  $\sigma\|\sigma$  configuration exhibit significantly greater magnitude compared to those observed in the  $\sigma\perp\sigma$  configuration.

## 5.4 Summary

The chapter focused on examining the impact of neighboring transitions, caused by Doppler broadening, on EIA and EIT in a degenerate two-level system. Specifically, the  $F_g = 2 \rightarrow F_e = 1, 2$  and 3 transitions the  $^{87}\text{Rb}$  D2 with both linear parallel ( $\pi\|\pi$ ) and linear perpendicular ( $\pi\perp\pi$ ) polarization of coupling and probe beams. A notable fluctuations in EIT and EIA resulting from the influence of neighboring transitions by artificially manipulating the hyperfine spacings of the  $5P_{3/2}$  state is presented using both the experimentally measured spectra and theoretical absorption profiles. The investigation also involves the evaluation of the relationship between spectral characteristics and hyperfine spacing for same circular ( $\sigma\|\sigma$ ) and circular orthogonal ( $\sigma\perp\sigma$ ) polarization of coupling and probe. This is achieved by intentionally manipulating the hyperfine spacing of  $^{85}\text{Rb}$  atoms. The prediction of transitions between EIA and EIT can be facilitated by utilizing the result obtained from this study.

## Chapter 6

# Conclusion

This thesis addresses mainly on two distinct subjects, namely modulation transfer spectroscopy (MTS) and the impact of neighboring transitions on electromagnetically induced absorption (EIA) and electromagnetically induced transmission (EIT). The MTS produces a signal that exhibits dispersive characteristics and without any background noise. This property makes it suitable for laser frequency stabilization without the need for direct modulation of the probe laser. Moreover, MTS exhibits a high sensitivity in detecting cycling transitions, making it particularly advantageous in scenarios involving closely spaced hyperfine transitions. The MTS signals are generated for the  $F_g = 3 \rightarrow F_e = 4$  transition of  $^{85}\text{Rb}$  and the  $F_g = 2 \rightarrow F_e = 3$  transition of  $^{87}\text{Rb}$  atoms with negligible background and zero crossing accurately centered at the resonance. In order to provide additional evidence of the applicability of this technique in achieving laser frequency stabilization in the presence of numerous closely spaced hyperfine transitions, we additionally acquired the MTS signal corresponding to the  $F_g = 2 \rightarrow F_e = 1$  transition of  $^{85}\text{Rb}$ . The MTS signals generated using a single laser have been compared with those obtained through the two-color MTS (TCMTS).

The experimental and theoretical demonstration of V-type TCMTS has been conducted for the D2 line of Rb atoms, taking into account Zeeman sublevels in order to address the optical Bloch equation. The probe beam is in resonance with the  $F_g = 3 \rightarrow F_e = 2, 3,$  and  $4$  transitions of  $^{85}\text{Rb}$  and  $F_g = 2 \rightarrow F_e = 1, 2,$  and  $3$  transitions of  $^{87}\text{Rb}$  atoms. The pump beam is both scanning and modulated. The pump beam is modulated using the electro-optic modulator (EOM). In the first case of  $^{85}\text{Rb}$  atoms, probe beam is fixed at  $F_g = 3 \rightarrow F_e = 4$  transition and pump beam is scanning across the transitions from the  $F_g = 3$  ground hyperfine state. This generates an MTS signal with larger peak to peak amplitude in comparison to the one-color MTS (OCMTS) with both pump and probe beams scanning across transitions from  $F_g = 3$  hyperfine ground state. In other two cases of TMTS for  $^{85}\text{Rb}$  atoms, the probe beam is fixed at  $F_g = 3 \rightarrow F_e = 3$  and  $F_g = 3 \rightarrow F_e = 2$  transitions. The scanning and modulated pump beam transfers modulation to

open transitions in a nonlinear four-wave mixing process in the Rb vapor cell. The MTS signals for  $F_g = 3 \rightarrow F_e = 3$  and  $F_g = 3 \rightarrow F_e = 2$  are weaker than for the probe beam fixed at  $F_g = 3 \rightarrow F_e = 4$ . The further away the transition is from the  $F_g = 3 \rightarrow F_e = 4$  closed transition, smaller is the peak to peak amplitude of the MTS Signal. Similarly, for the  $^{87}\text{Rb}$  atoms, the MTS signals for  $F_g = 2 \rightarrow F_e = 2$  and  $F_g = 2 \rightarrow F_e = 1$  are weaker than for the probe beam fixed at  $F_g = 2 \rightarrow F_e = 3$ . The ratio at which the peak to peak amplitude decreases when locking the probe to the transition further away from the  $F_g = 2 \rightarrow F_e = 3$  closed transition is larger for  $^{87}\text{Rb}$  atoms which is due to the larger hyperfine splitting of  $^{87}\text{Rb}$  in comparison to  $^{85}\text{Rb}$ . One advantageous aspect of this technique is its ability to prepare several configurations of pump and probe beams for frequency stabilization. The theoretical calculations utilizing the optical Bloch equation exhibit a strong agreement with the experimentally measured results. Therefore, spectroscopic technique is available for performing MTS with different configurations of pump and probe beams.

Furthermore, a study has been conducted on the tunable nature of the MTS. This property allows the generation of a tunable reference signal that exhibits dispersive-like behavior without compromising on peak to peak amplitude and signal gradient. The Tunable Modulation Transfer Spectroscopy (TMTS) is employed to generate dispersive-like signal for  $F_g = 3 \rightarrow F_e = 4$  and  $F_g = 2 \rightarrow F_e = 1$  D2 transitions  $^{85}\text{Rb}$  atoms. These TMTS signals are utilized for Type I and Type II magneto-optical trapping (MOT) of atoms in the  $F_g = 3$  and  $F_g = 2$  hyperfine ground states, respectively. In the context of the  $F_g = 2 \rightarrow F_e = 1$  cycling transition where  $F_g < F_e$ , it is observed that the ground and excited Zeeman sublevels remain decoupled. Consequently, the excited hyperfine level can be considered as the dark state, devoid of any contribution to the trapping process. As a result, a weak trapping force is observed.

Subsequently, a study is conducted on the impact of neighboring transitions on electromagnetically induced absorption (EIA) and electromagnetically induced transmission (EIT) in relation to the varying angle between the polarization axes of the coupling and probe beams. This investigation specifically focuses on the

D2 transition line of Rb. The relative orientation of the polarization axis of the coupling and probing beams is a significant factor in the transition between EIA and EIT, as well as the influence of neighboring hyperfine transitions. Closed transitions,  $F_g = 3 \rightarrow F_e = 4$  of  $^{85}\text{Rb}$  and  $F_g = 2 \rightarrow F_e = 3$  of  $^{87}\text{Rb}$ , have EITs at 0 degrees and switch to EIAs at a higher polarization rotational angle. Furthermore, open transitions,  $F_g = 3 \rightarrow F_e = 2$  and  $3$  of  $^{85}\text{Rb}$  and  $F_g = 2 \rightarrow F_e = 1$  and  $2$  of  $^{87}\text{Rb}$  have EITs at a smaller polarization rotational angle, but as the angle increases, the EITs switch to EIAs, which is largely due to the influence of neighboring hyperfine transitions. Closed transition  $F_g = 3 \rightarrow F_e = 4$  of  $^{85}\text{Rb}$  ( $F_g = 2 \rightarrow F_e = 3$  of  $^{87}\text{Rb}$ ) has EIT at 0 degrees due to neighboring  $F_g = 3 \rightarrow F_e = 2$  and  $3$  ( $F_g = 2 \rightarrow F_e = 1$  and  $2$ ) open transitions of  $^{85}\text{Rb}$  ( $^{87}\text{Rb}$ ). Likewise, open transitions  $F_g = 3 \rightarrow F_e = 2$  and  $3$  of  $^{85}\text{Rb}$  ( $F_g = 2 \rightarrow F_e = 1$  and  $2$  of  $^{87}\text{Rb}$ ) have EIAs at a larger polarization rotational angle due to the strong EIA of the neighboring closed transition  $F_g = 3 \rightarrow F_e = 4$  ( $F_g = 2 \rightarrow F_e = 3$ ). Transitions from lower ground hyperfine energy levels of  $^{85}\text{Rb}$  and  $^{87}\text{Rb}$  are open systems. Consequentially, the spectral profiles of  $F_g = 2 \rightarrow F_e = 1, 2,$  and  $3$  transitions of  $^{85}\text{Rb}$  and  $F_g = 1 \rightarrow F_e = 0, 1,$  and  $2$  transitions of  $^{87}\text{Rb}$  exhibit EITs. By comparing the experimental spectra with DTLS and DMLS absorption profiles, it is evident that the influence of neighboring transitions on each transition causes the amplitude of EITs to increase for transitions from lower ground hyperfine energy levels. The determination of the critical angles for coherent control of EIA and EIT is achieved using a combination of experimental measurements and theoretical calculations utilizing optical Bloch equations. Theoretical calculations exhibit a strong correlation with their corresponding experimental spectra.

Lastly, the influence of neighboring transitions on EIA and EIT in a degenerate two-level system with respect to the artificial variation in the hyperfine splitting of Rb atoms is investigated. Specifically, we focus on the  $F_g = 2 \rightarrow F_e = 1, 2,$  and  $3$  transitions of the D2 line in  $^{87}\text{Rb}$ , taking into account the effects of Doppler broadening with both linear parallel ( $\pi \parallel \pi$ ) and linear perpendicular ( $\pi \perp \pi$ ) polarization of coupling and probe beams. The focus of our study is the notable fluctuation observed in EIT and EIA caused by hyperfine splitting between the states.

To investigate this, we artificially manipulate the hyperfine spacings of the  $5P_{3/2}$  state and compare them with experimentally measured spectra. The investigation also involves the evaluation of the relationship between spectral characteristics and hyperfine spacing for same circular ( $\sigma\parallel\sigma$ ) and circular orthogonal ( $\sigma\perp\sigma$ ) polarization of coupling and probe for  $^{85}\text{Rb}$  atoms. This is achieved by artificially varying the hyperfine splitting of  $^{85}\text{Rb}$  atoms. The prediction of transformations between EIA and EIT can be facilitated by utilizing the results obtained from this study.

## List of Publications

---

1. Z. A. S. Jadoon, **Aisar-ul Hassan**, H.-R. Noh, and J. T. Kim, Effects of neighboring transitions of electromagnetically induced absorption and transparency in in  $^{85}\text{Rb}$  atoms based on the linear parallel polarization of coupling and probe beams, *Optics Communications*, **520**: 128512 2022.
2. Z. A. S. Jadoon, **Aisar-ul Hassan**, H.-R. Noh, and J. T. Kim, Electromagnetically induced absorption in Rb atoms with circular polarization of laser beams: Effects of neighboring transitions, *Heliyon*, **8**: e11752 2022.
3. **Aisar-ul Hassan**, Z. A. S. Jadoon, J. T. Kim, and H.-R. Noh, Effects of neighboring transitions on electromagnetically induced absorption and transparency in Rb atoms in circular orthogonal polarization configuration, *Journal of the Korean Physical Society*, **82**: 907–911 2023.
4. Z. A. S. Jadoon, **Aisar-ul Hassan**, H.-R. Noh, and J. T. Kim, Effects of neighboring transitions on electromagnetically induced absorption and transparency in  $^{87}\text{Rb}$  atoms with respect to varying hyperfine spacings, *JOSA B*, **40**: 2612-2617 2023.
5. **Aisar-ul Hassan**, H.-R. Noh, and J. T. Kim, Effects of neighboring transitions on electromagnetically induced absorption and transparency in Rb atoms with respect to varying linear polarization of coupling and probe beams, To be submitted.
6. **Aisar-ul Hassan**, H.-R. Noh, and J. T. Kim, Two-color Modulation Transfer Spectroscopy of D2 line of  $^{85}\text{Rb}$  atoms: Theory and Experiment, To be submitted.
7. **Aisar-ul Hassan**, H.-R. Noh, and J. T. Kim, Tunable Modulation Transfer Spectroscopy of D2 line of  $^{85}\text{Rb}$  atoms: Theory and Experiment, To be submitted.



## Bibliography

- [1] T. H. MAIMAN. Stimulated optical radiation in ruby. *Nature*, **187**:493–494, 1960.
- [2] M. H. Anderson, J. R. Ensher, M. R. Matthews, C. E. Wieman, and E. A. Cornell. Observation of bose-einstein condensation in a dilute atomic vapor. *Science*, **269**:198–201, 1995.
- [3] K. B. Davis, M. O. Mewes, M. R. Andrews, N. J. van Druten, D. S. Durfee, D. M. Kurn, and W. Ketterle. Bose-einstein condensation in a gas of sodium atoms. *Phys. Rev. Lett.*, **75**:3969–3973, 1995.
- [4] C. C. Bradley, C. A. Sackett, J. J. Tollett, and R. G. Hulet. Evidence of bose-einstein condensation in an atomic gas with attractive interactions. *Phys. Rev. Lett.*, **75**:1687–1690, 1995.
- [5] Gregory M Harry. Advanced ligo: the next generation of gravitational wave detectors. *Classical and Quantum Gravity*, **27**:084006, 2010.
- [6] J. E. M. Goldsmith, E. W. Weber, and T. W. Hänsch. New measurement of the rydberg constant using polarization spectroscopy of H $\alpha$ . **41**:1525–1528, 1978.
- [7] Steven Chu. Nobel lecture: The manipulation of neutral particles. *Rev. Mod. Phys.*, **70**:685–706, 1998.
- [8] Masao Takamoto, Feng-Lei Hong, Ryoichi Higashi, and Hidetoshi Katori. An optical lattice clock. **435**:321–324, 2005.
- [9] Masao Takamoto, Tetsushi Takano, and Hidetoshi Katori. Frequency comparison of optical lattice clocks beyond the dick limit. **5**:288–292, 2011.
- [10] Kazuhiro Yamanaka, Noriaki Ohmae, Ichiro Ushijima, Masao Takamoto, and Hidetoshi Katori. Frequency ratio of  $^{199}\text{Hg}$  and  $^{87}\text{Sr}$  optical lattice clocks beyond the si limit. *Phys. Rev. Lett.*, **114**:230801, 2015.
- [11] W. Demtroder. *Laser Spectroscopy*. Springer, 3rd edition edition.

- [12] K. B. MacAdam, A. Steinbach, and C. Wieman. A narrow-band tunable diode laser system with grating feedback, and a saturated absorption spectrometer for Cs and Rb. *American Journal of Physics*, **60**:1098–1111, 1992.
- [13] Gary C. Bjorklund. Frequency-modulation spectroscopy: a new method for measuring weak absorptions and dispersions. *Opt. Lett.*, **5**:15–17.
- [14] L Mudarikwa, K Pahwa, and J Goldwin. Sub-doppler modulation spectroscopy of potassium for laser stabilization. *Journal of Physics B: Atomic, Molecular and Optical Physics*, **45**:065002, 2012.
- [15] C. Wieman and T. W. Hänsch. Doppler-free laser polarization spectroscopy. *Phys. Rev. Lett.*, **36**:1170–1173, 1976.
- [16] C.P. Pearman, C.S. Adams, S.G. Cox, P.F. Griffin, D.A. Smith, and I.G. Hughes. Polarization spectroscopy of a closed atomic transition: applications to laser frequency locking. *Journal of Physics B: Atomic, Molecular and Optical Physics*, **35**:5141–5151, 2002.
- [17] V.B. Tiwari, S. Singh, S.R. Mishra, H.S. Rawat, and S.C. Mehendale. Laser frequency stabilization using a balanced bi-polarimeter. **83**:93–96, 2006.
- [18] Jon H. Shirley. Modulation transfer processes in optical heterodyne saturation spectroscopy. *Opt. Lett.*, **7**:537–539, 1982.
- [19] Jing Zhang, Dong Wei, Changde Xie, and Kunchi Peng. Characteristics of absorption and dispersion for rubidium D2 lines with the modulation transfer spectrum. *Opt. Express*, **11**:1338–1344, 2003.
- [20] D J McCarron, S A King, and S L Cornish. Modulation transfer spectroscopy in atomic rubidium. *Measurement Science and Technology*, **19**:105601, 2008.
- [21] Heung-Ryoul Noh, Sang Eon Park, Long Zhe Li, Jong-Dae Park, and Chang-Ho Cho. Modulation transfer spectroscopy for  $^{87}\text{Rb}$  atoms: theory and experiment. *Opt. Express*, **19**:23444–23452, 2011.

- [22] G. V. Osipenko, M. S. Aleynikov, and A. G. Sukhovskaya. Offset laser frequency stabilization using modulation transfer spectroscopy. **66**:1–5, 2023.
- [23] Daniel A. Steck. Rubidium 85 D line data. (revision 2.3.2, 10 September 2023).
- [24] Daniel A. Steck. Rubidium 87 D line data. (revision 2.3.2, 10 September 2023).
- [25] Theodor W. Hansch, Arthur L. Schawlow, and George W. Series. The spectrum of atomic hydrogen. **240**:94–111, 1979.
- [26] O. Schmidt, K. M. Knaak, R. Wynands, and D. Meschede. Cesium saturation spectroscopy revisited: How to reverse peaks and observe narrow resonances. **59**:167–178, 1994.
- [27] Daryl W. Preston. Doppler-free saturated absorption: Laser spectroscopy. **64**:1432–1436, 1996.
- [28] E. L. Raab, M. Prentiss, Alex Cable, Steven Chu, and D. E. Pritchard. Trapping of neutral sodium atoms with radiation pressure. *Phys. Rev. Lett.*, **59**:2631–2634, 1987.
- [29] S. L. Cornish, N. R. Claussen, J. L. Roberts, E. A. Cornell, and C. E. Wieman. Stable  $^{85}\text{Rb}$  bose-einstein condensates with widely tunable interactions. *Phys. Rev. Lett.*, **85**:1795–1798, 2000.
- [30] P. A. Altin, N. P. Robins, D. Döring, J. E. Debs, R. Poldy, C. Figl, and J. D. Close.  $^{85}\text{Rb}$  tunable-interaction Bose–Einstein condensate machine. *Review of Scientific Instruments*, **81**(6):063103, 2010.
- [31] A. L. Marchant, S. Händel, S. A. Hopkins, T. P. Wiles, and S. L. Cornish. Bose-einstein condensation of  $^{85}\text{Rb}$  by direct evaporation in an optical dipole trap. *Phys. Rev. A*, **85**:053647, 2012.

- [32] V. B. Tiwari, S. Singh, H. S. Rawat, and S. C. Mehendale. Cooling and trapping of  $^{85}\text{Rb}$  atoms in the ground hyperfine  $F = 2$  state. *78*, 2008.
- [33] M. H. Anderson, J. R. Ensher, M. R. Matthews, C. E. Wieman, and E. A. Cornell. Observation of bose-einstein condensation in a dilute atomic vapor. *Science*, **269**:198–201, 1995.
- [34] B. DeMarco and D. S. Jin. Onset of fermi degeneracy in a trapped atomic gas. *Science*, **285**:1703–1706, 1999.
- [35] G. Modugno, G. Ferrari, G. Roati, R. J. Brecha, A. Simoni, and M. Inguscio. Bose-einstein condensation of potassium atoms by sympathetic cooling. *Science*, **294**:1320–1322, 2001.
- [36] Andrew G. Truscott, Kevin E. Strecker, William I. McAlexander, Guthrie B. Partridge, and Randall G. Hulet. Observation of fermi pressure in a gas of trapped atoms. *Science*, **291**:2570–2572, 2001.
- [37] C. C. Bradley, C. A. Sackett, J. J. Tollett, and R. G. Hulet. Evidence of bose-einstein condensation in an atomic gas with attractive interactions. *Phys. Rev. Lett.*, **75**:1687–1690, 1995.
- [38] K. B. Davis, M. O. Mewes, M. R. Andrews, N. J. van Druten, D. S. Durfee, D. M. Kurn, and W. Ketterle. Bose-einstein condensation in a gas of sodium atoms. *Phys. Rev. Lett.*, **75**:3969–3973, 1995.
- [39] Tino Weber, Jens Herbig, Michael Mark, Hanns-Christoph Nägerl, and Rudolf Grimm. Bose-einstein condensation of cesium. *Science*, **299**:232–235, 2003.
- [40] Chen-Lung Hung, Xibo Zhang, Nathan Gemelke, and Cheng Chin. Accelerating evaporative cooling of atoms into bose-einstein condensation in optical traps. *Phys. Rev. A*, **78**:011604, 2008.

- [41] D. J. McCarron, H. W. Cho, D. L. Jenkin, M. P. Köppinger, and S. L. Cornish. Dual-species bose-einstein condensate of  $^{87}\text{Rb}$  and  $^{133}\text{Cs}$ . *Phys. Rev. A*, **84**:011603, 2011.
- [42] H. J. Metcalf and P. van der Straten. Laser cooling and trapping of atoms. *J. Opt. Soc. Am. B*, **20**:887–908, 2003.
- [43] K. N. Jarvis, B. E. Sauer, and M. R. Tarbutt. Characteristics of unconventional Rb magneto-optical traps. *Phys. Rev. A*, **98**:043432, 2018.
- [44] M. R. Tarbutt. Magneto-optical trapping forces for atoms and molecules with complex level structures. **17**:015007, 2015.
- [45] J. Flemming, A.M. Tuboy, D.M.B.P. Milori, L.G. Marcassa, S.C. Zilio, and V.S. Bagnato. Magneto-optical trap for sodium atoms operating on the D1 line. *Optics Communications*, **135**:269–272, 1997.
- [46] S.N. Atutov, V. Biancalana, A. Burchianti, R. Calabrese, S. Gozzini, V. Guidi, P. Lenisa, C. Marinelli, E. Mariotti, L. Moi, K. Nasyrov, and S. Pod'yachev. Sodium MOT collection efficiency as a function of the trapping and repumping laser frequencies and intensities. **13**:71–82, 2001.
- [47] J. D. Pritchard, D. Maxwell, A. Gauguet, K. J. Weatherill, M. P. A. Jones, and C. S. Adams. Cooperative atom-light interaction in a blockaded rydberg ensemble. *Phys. Rev. Lett.*, **105**:193603, 2010.
- [48] Y. O. Dudin and A. Kuzmich. Strongly interacting rydberg excitations of a cold atomic gas. *Science*, **336**:887–889, 2012.
- [49] O. Firstenberg, C. S. Adams, and S. Hofferberth. Nonlinear quantum optics mediated by rydberg interactions. **49**:152003, 2016.
- [50] Thibault Peyronel, Ofer Firstenberg, Qi-Yu Liang, Sebastian Hofferberth, Alexey V. Gorshkov, Thomas Pohl, Mikhail D. Lukin, and Vladan Vuletić. Quantum nonlinear optics with single photons enabled by strongly interacting atoms. **488**:57–60, 2012.

- [51] D. Maxwell, D. J. Szwer, D. Paredes-Barato, H. Busche, J. D. Pritchard, A. Gauguet, K. J. Weatherill, M. P. A. Jones, and C. S. Adams. Storage and control of optical photons using rydberg polaritons. *Phys. Rev. Lett.*, **110**:103001, 2013.
- [52] L. Isenhower, E. Urban, X. L. Zhang, A. T. Gill, T. Henage, T. A. Johnson, T. G. Walker, and M. Saffman. Demonstration of a neutral atom controlled-not quantum gate. *Phys. Rev. Lett.*, **104**:010503, 2010.
- [53] M. Saffman, T. G. Walker, and K. Mølmer. Quantum information with rydberg atoms. *Rev. Mod. Phys.*, **82**:2313–2363, 2010.
- [54] T. Wilk, A. Gaëtan, C. Evellin, J. Wolters, Y. Miroshnychenko, P. Grangier, and A. Browaeys. Entanglement of two individual neutral atoms using rydberg blockade. *Phys. Rev. Lett.*, **104**:010502, 2010.
- [55] M. D. Lukin, M. Fleischhauer, R. Cote, L. M. Duan, D. Jaksch, J. I. Cirac, and P. Zoller. Dipole blockade and quantum information processing in mesoscopic atomic ensembles. *Phys. Rev. Lett.*, **87**:037901, 2001.
- [56] Henning Labuhn, Daniel Barredo, Sylvain Ravets, Sylvain de Léséleuc, Tommaso Macrì, Thierry Lahaye, and Antoine Browaeys. Tunable two-dimensional arrays of single rydberg atoms for realizing quantum ising models. **534**:667–670, 2016.
- [57] Hannes Bernien, Sylvain Schwartz, Alexander Keesling, Harry Levine, Ahmed Omran, Hannes Pichler, Soonwon Choi, Alexander S. Zibrov, Manuel Endres, Markus Greiner, Vladan Vuletić, and Mikhail D. Lukin. Probing many-body dynamics on a 51-atom quantum simulator. **551**:579–584, 2017.
- [58] Harold J. Metcalf and Peter Van Der Straten. *Laser Cooling and Trapping*. Graduate Texts in Contemporary Physics. Springer, 1999.

- [59] A. M. Akulshin, S. Barreiro, and A. Lezama. Electromagnetically induced absorption and transparency due to resonant two-field excitation of quasidegenerate levels in Rb vapor. *Phys. Rev. A*, **57**:2996–3002, 1998.
- [60] Michael Fleischhauer, Atac Imamoglu, and Jonathan P. Marangos. Electromagnetically induced transparency: Optics in coherent media. *Rev. Mod. Phys.*, **77**:633–673, 2005.
- [61] Silvia Gozzini, Andrea Fioretti, Alessandro Lucchesini, Luca Marmugi, Carmela Marinelli, Stoyan Tsvetkov, Sanka Gateva, and Stefka Cartaleva. Tunable and polarization-controlled high-contrast bright and dark coherent resonances in potassium. **42**:2930–2933, 2017.
- [62] Mangesh Bhattarai, Vineet Bharti, and Vasant Natarajan. Tuning of the Hanle effect from EIT to EIA using spatially separated probe and control beams. **8**:7525, 2018.
- [63] Sapam Ranjita Chanu, Kanhaiya Pandey, and Vasant Natarajan. Conversion between electromagnetically induced transparency and absorption in a three-level lambda system. **98**:44009, 2012.
- [64] Luca Spani Molella, Katrin Dahl, Rolf-Hermann Rinkleff, and Karsten Danzmann. Coupling-probe laser spectroscopy of degenerate two-level systems: An experimental survey of various polarisation combinations. **282**:3481–3486, 2009.
- [65] Katrin Dahl, Luca Spani Molella, Rolf-Hermann Rinkleff, and Karsten Danzmann. Switching from “absorption within transparency” to “transparency within transparency” in an electromagnetically induced absorption dominated transition. **33**:983–985, 2008.
- [66] T. Zigdon, A. D. Wilson-Gordon, and H. Friedmann. Absorption spectra for strong pump and probe in atomic beam of cesium atoms. *Phys. Rev. A*, **80**:033825, 2009.

- [67] A. A. Zhukov, S. A. Zibrov, G. V. Romanov, Y. O. Dudin, V. V. Vassiliev, V. L. Velichansky, and V. P. Yakovlev. Electromagnetically induced absorption in a bichromatic laser field. *Phys. Rev. A*, **80**:033830, 2009.
- [68] D. McGloin, M. H. Dunn, and D. J. Fulton. Polarization effects in electromagnetically induced transparency. *Phys. Rev. A*, **62**:053802, 2000.
- [69] Nibedita Ram and M. Pattabiraman. Sign reversal of hanle electromagnetically induced absorption with orthogonal circularly polarized optical fields. **43**:245503, 2010.
- [70] H. G. Song, R. Choi, and C. H. Oh. Temperature dependence of electromagnetically induced transparency in a Cs atomic vapor cell. **51**:40, 2007.
- [71] ChengJing Gao and HaiFeng Zhang. Switchable metasurface with electromagnetically induced transparency and absorption simultaneously realizing circular polarization-insensitive circular-to-linear polarization conversion. **534**:2200108, 2022.
- [72] Raghwinder Singh Grewal and M. Pattabiraman. Hanle electromagnetically induced absorption in open transitions of the  $^{87}\text{Rb}$  D2 line. **48**:085501, 2015.
- [73] Hafeez-ur Rehman, Muhammad Adnan, Heung-Ryoul Noh, and Jin-Tae Kim. Spectral features of electromagnetically induced absorption in  $^{85}\text{Rb}$  atoms. **48**:115502, 2015.
- [74] Hafeez Ur Rehman, Muhammad Qureshi Mohsin, Heung-Ryoul Noh, and Jin-Tae Kim. Electromagnetically induced absorption due to transfer of coherence and coherence population oscillation for the  $F_g=3 \rightarrow F_e=4$  transition in  $^{85}\text{Rb}$  atoms. **381**:127–134, 2016.
- [75] Zeeshan Ali Safdar Jadoon, Heung-Ryoul Noh, and Jin-Tae Kim. Effects of neighboring transitions on the mechanisms of electromagnetically in-



- duced absorption and transparency in an open degenerate multilevel system. **12**:145, 2022.
- [76] Zeeshan Ali Safdar Jadoon, Aisar-ul Hassan, Heung-Ryoul Noh, and Jin-Tae Kim. Effects of neighboring transitions on electromagnetically induced absorption and transparency in  $^{85}\text{Rb}$  atoms based on the linear parallel polarization of coupling and probe beams. **520**:128512, 2022.
- [77] Zeeshan Ali Safdar Jadoon, Aisar Ul Hassan, Heung-Ryoul Noh, and Jin-Tae Kim. Electromagnetically induced absorption in Rb atoms with circular polarization of laser beams: Effects of neighboring transitions. **8**:e11752, 2022.
- [78] Aisar Ul Hassan, Zeeshan Ali Safdar Jadoon, Jin-Tae Kim, and Heung-Ryoul Noh. Effects of neighboring transitions on electromagnetically induced absorption and transparency in Rb atoms in circular orthogonal polarization configuration. **82**:907–911, 2023.
- [79] Lene Vestergaard Hau, S. E. Harris, Zachary Dutton, and Cyrus H. Behroozi. Light speed reduction to 17 metres per second in an ultracold atomic gas. **397**:594–598, 1999.
- [80] Paul Mandel. Lasing without inversion: A useful concept? **34**:235–246, 1993.
- [81] Marlan O. Scully and Michael Fleischhauer. High-sensitivity magnetometer based on index-enhanced media. *Phys. Rev. Lett.*, **69**:1360–1363, 1992.
- [82] Michael Fleischhauer and Marlan O. Scully. Quantum sensitivity limits of an optical magnetometer based on atomic phase coherence. *Phys. Rev. A*, **49**:1973–1986, 1994.
- [83] Dmitry Budker and Michael Romalis. Optical magnetometry. **3**:227–234, 2007.

- [84] M. D. Lukin, S. F. Yelin, M. Fleischhauer, and M. O. Scully. Quantum interference effects induced by interacting dark resonances. *Phys. Rev. A*, **60**:3225–3228, 1999.
- [85] M. Fleischhauer and M. D. Lukin. Dark-state polaritons in electromagnetically induced transparency. *Phys. Rev. Lett.*, **84**:5094–5097, 2000.
- [86] Chien Liu, Zachary Dutton, Cyrus H. Behroozi, and Lene Vestergaard Hau. Observation of coherent optical information storage in an atomic medium using halted light pulses. **409**:490–493, 2001.
- [87] D. F. Phillips, A. Fleischhauer, A. Mair, R. L. Walsworth, and M. D. Lukin. Storage of light in atomic vapor. *Phys. Rev. Lett.*, **86**:783–786, 2001.
- [88] A. S. Zibrov, A. B. Matsko, O. Kocharovskaya, Y. V. Rostovtsev, G. R. Welch, and M. O. Scully. Transporting and time reversing light via atomic coherence. *Phys. Rev. Lett.*, **88**:103601, 2002.
- [89] C. H. van der Wal, M. D. Eisaman, A. André, R. L. Walsworth, D. F. Phillips, A. S. Zibrov, and M. D. Lukin. Atomic memory for correlated photon states. **301**:196–200, 2003.
- [90] R. G. Beausoleil, W. J. Munro, D. A. Rodrigues, and T. P. Spiller. Applications of electromagnetically induced transparency to quantum information processing. **51**:2441–2448, 2004.
- [91] M. Fleischhauer, C. H. Keitel, M. O. Scully, Chang Su, B. T. Ulrich, and Shi-Yao Zhu. Resonantly enhanced refractive index without absorption via atomic coherence. *Phys. Rev. A*, **46**:1468–1487, 1992.
- [92] Byoung S. Ham and Philip R. Hemmer. Coherence switching in a four-level system: Quantum switching. *Phys. Rev. Lett.*, **84**:4080–4083, 2000.
- [93] D. Felinto, L. G. Marcassa, V. S. Bagnato, and S. S. Vianna. Influence of the number of atoms in a ring-shaped magneto-optical trap: Observation of bifurcation. **60**:2591–2594, 1999.

- [94] D. Felinto, H. Regehr, J. W. R. Tabosa, and S. S. Vianna. Fluctuations in ball- and ring-shaped magneto-optical traps at low densities. **18**:1410, 2001.
- [95] G. Wasik, W. Gawlik, J. Zachorowski, and W. Zawadzki. Laser frequency stabilization by doppler-free magnetic dichroism. **75**:613–619, 2002.
- [96] Gyeong-Won Choi and Heung-Ryoul Noh. Sub-doppler DAVLL spectra of the D1 line of rubidium: a theoretical and experimental study. **48**:115008, 2015.
- [97] Gyeong-Won Choi and Heung-Ryoul Noh. Line shapes in sub-doppler DAVLL in the  $^{87}\text{Rb}$ -D2 line. **367**:312–315, 2016.
- [98] A. Lezama, S. Barreiro, and A. M. Akulshin. Electromagnetically induced absorption. *Phys. Rev. A*, **59**:4732–4735, 1999.